Università degli Studi di Torino

Facoltà di Scienze Matematiche, Fisiche e Naturali
Dottorato di Ricerca in Fisica -XXIII ciclo
FIS/01 - Fisica Sperimentale

Study of the Diffractive Component of the Inclusive Z→ee,$\mu\mu$ Cross Section at $\sqrt{s}$= 7 TeV with the CMS Detector

Candidato
Dr. Matteo Marone

Tutori
Dr.ssa Arcidiacono Roberta
Dr. Cartiglia Nicolo

Coordinatore
Prof. Guido Boffetta

La scienza conosce solo un comandamento:
contribuire allo sviluppo scientifico.
Bertold Brecht

Contents

List of Figures

List of Tables

Introduction

The Standard Model formulated in 1973 led to a series of successes, providing a large numbers of predictions experimentally verified. Some questions are still unsolved: their answers will be hopefully accessible at high energy scale. Therefore, the pp collisions occurring at LHC are designed to reach the world highest energy on the center of mass (14 TeV) with peak instantaneous luminosity $(10^{34} cm^{-2} s^{-1})$.

In the last 50 years, the diffractive physics has been extensively studied at DESY and Fermilab, improving the understanding of hard-diffractive processes. The description of diffraction in terms of QCD has opened the way to a rich physics program, and to a more complete understanding of the theory of strong interactions. The study of hard diffraction at LHC is feasible and it will offer the possibility to explore and test the ideas and models developed at much lower energies.

In this thesis a new method to select diffractive events to deal with the high number of pile-up events produced at high luminosity is proposed. Using the 2010 proton-proton run, a study on the diffractive component of the inclusive $Z \to \mu\mu$,ee cross section is performed in Chapter 5.

The physics program, together with an introduction on diffractive physics is presented in Chapter 1. After an overview of the Compact Muon Solenoid (CMS) detector in Chapter 2, a special attention has been reserved to the Electromagnetic Calorimeter (ECAL) in Chapter 3. I have actively participated to the commissioning phase culminated with the 2008 CMS cosmic run. I have also contributed to the development of the ECAL data acquisition system and in particular the development of the online software which controls the Detector Control Units (DCU) system. The DCU system is part of the front-end electronics able to read relevant parameters such as temperatures and supply voltages of the on-detector electronics [36].

In order to reach the potential to discover new physics, stringent requirements on the ECAL temperature stability have been placed. In chapter 4 a study carried on the DCU systems has been used to demonstrate that the temperature stability lies within the specifications [64],[59].

Chapter 1

Physics at the Large Hadron Collider (LHC)

The absence of the Flavour Changing Neutral Currents (FCNC), the universality of weak charged current interaction, the smallness of the K^0 - $\overline{K^0}$ mixing, the CP violation were mysteries unsolved until the proposal of the Standard Model (SM). A breathtaking series of successes follow the neutral currents discovery in 1973. After that, charm was discovered in 1974, tau lepton in 1975, beauty in 1977, the W and Z boson in the 1983. The SM was soon universally accepted. After 30 years the model provides a great number of predictions experimentally verified.

Unfortunately it leaves some questions unresolved: among this, the most evident is the fact that it requires so many different particle masses. Moreover, the barion-antibarion asymmetry in the universe and the nature of the Higgs particle are far from being understood. The LHC machine [1], together with theoretical breakthroughs will hopefully investigate these scenarios.

1.1 LHC

The LHC is a particle accelerator built at CERN. It is contained in a circular tunnel having a circumference of 27 kilometers, up to 175 metres underground. The accelerator can provide two colliding proton beams, with a maximum energy of 7 TeV per proton (presently of 3.5 TeV), as well as heavy ions beams with an energy of $Z/A \cdot 7$ TeV per nucleon. The beams are injected in bunches separated in time by 25 ns. Its design luminosity is 10^{34} cm^{-2}s^{-1}.

The main machine parameters are summarized in Table 1.1. A proton-proton

Parameter		p-p	$^{208}Pb^{82+}$
Energy per nucleon (TeV)	E	7	2.76
Dipole field at 7 TeV (T)	B	8.33	8.33
Design Luminosity ($cm^{-2}s^{-1}$)	$\mathcal{L}$	10^{34}	10^{27}
Bunch time separation (ns)		25	100
Max. No. of bunches	k_B	2808	592
No. particles per bunch	N_p	1.15×10^{11}	7.0×10^7
β-value at IP (m)	$\beta^\star$	0.55	0.5
RMS beam radiius at IP (μm)	$\sigma^\star$	16.7	15.9
Luminosity lifetime (h)	τ_L	15	6

Table 1.1: *LHC parameters for p-p and Pb-Pb collisions*

collider was chosen because:

- being a hadron collider, the colliding entities are the partons, which carry a variable fraction x of the whole hadron momentum. Therefore the center-of-mass energy of the hard scattering process can span different orders of magnitude.

- The storage and production of proton bunches is relatively easier than anti-protons. This leads to an higher luminosity.

- In a circular collider[1] of radius R, due to their higher mass, the usage of protons imply a smaller energy loss for synchrotron radiation with respect to electrons.

Another main parameter strongly influenced by the physics goal is the luminosity. In order to compensate for the low cross section of the interesting processes, LHC must provide a very high number of collisions to accumulate statistics for the analysis. The luminosity in fact represents the number of collisions per unit time and cross-sectional area of the beams. The relation between event rate R of a given process with cross section σ and the luminosity $\mathcal{L}$ is given by:

$$R = \mathcal{L}\sigma \tag{1.1}$$

where the luminosity is defined as:

$$\mathcal{L} = \frac{\gamma f k_B N_p^2}{4\pi \epsilon_n \beta^\star} F, \tag{1.2}$$

---

[1]the energy loss per turn due to synchrotron radiation is proportional to $\frac{(E/m)^4}{R}$, where E and m are respectively the energy and mass of the particles accelerated.

where γ is the Lorentz factor, f is the crossing frequency, k_B is the number of bunches, N_p is the number of protons per bunch, ϵ_n is the normalized transverse emittance (with a design value of 3.75 μm), $\beta^\star$ is the betatron function at the interaction point, and F is the reduction factor due to the crossing angle.

The main drawback of this powerful design is that the total event rate will be so high that several interactions overlap in the same bunch crossing, creating the so called pile up. It has been estimated that, at highest luminosity, with a 55 mb cross section for p-p non-diffractive inelastic process predicted by PYTHIA montecarlo [2], there will be on average 17.3 events occurring at every bunch crossing, with about 50 charged tracks per interaction. The high bunch crossing frequency, the strong pile-up and the high event rate dictate strict requirements on the design of the detectors. The electronics (discussed in details in chapter 2 and 3) have to be very fast, while the granularity have to be necessary high to avoid the overlap of particles in the same sensitive elements. Moreover, LHC detectors will also have to stand extremely high radiations doses, therefore all the electronics will need to be radiation hard. Finally, it needs additional requirements to the online trigger selection, that has to deal with a background rate several orders of magnitude higher than the signal rate.

1.1.1 Phenomenology at LHC

In Figure 1.1 are shown the cross sections and the production rate at LHC of interesting processes as a function of the center-of-mass energy and of the mass of the produced particle. In table 1.2 is presented the number of events produced for a given process, at each collision point, at a luminosity of L=2 10^{33} cm^{-2}s^{-1}.

The previous table and figure underline a very remarkable aspect of LHC physics: the overwhelming background rate compared to the interesting physics processes. The Higgs production, for example, has a cross section at least ten orders of magnitude smaller than the total inelastic cross section. This is due to the "minimum bias events": the bulk of events produced in the proton-proton collisions is either due to the low-p_T scattering, where the protons collide at large distances, or to QCD high-p_T processes. They constitute the background for other processes in which massive particles are created in the hard scattering, so they are in general considered uninteresting in LHC physics studies.

The energy of the initial state partons in the events is given by the Partons Density Functions (PDFs). Two examples of PDFs for two different Q^2 are
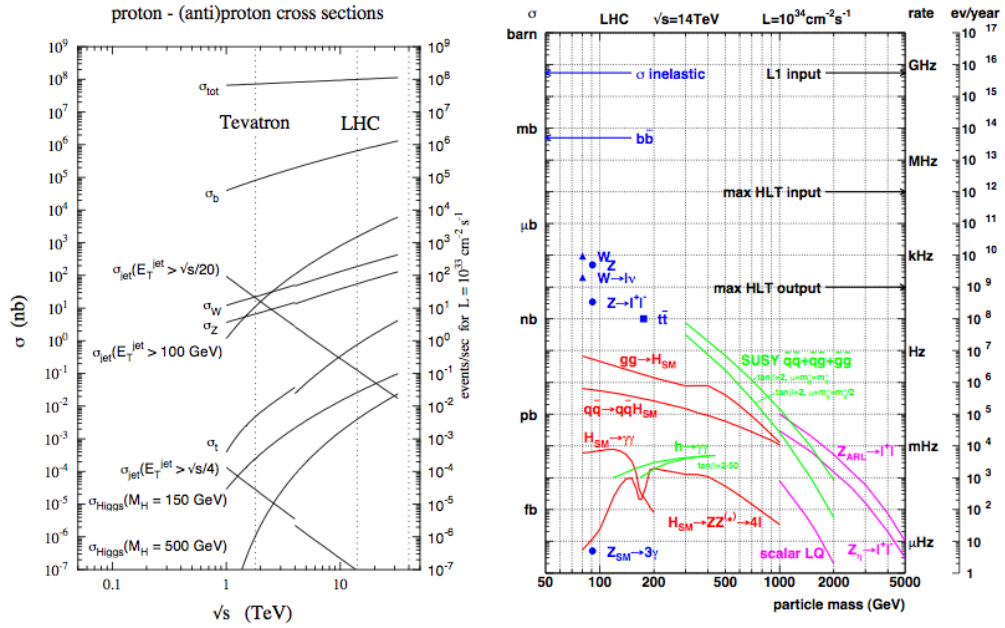
Figure 1.1: *Cross section as a function of the center-of-mass energy (left) and rate of events at LHC as a function of the mass of the produced particle (right) for interesting processes.*

shown in Fig 1.2. The collisions between the two partons happens then at
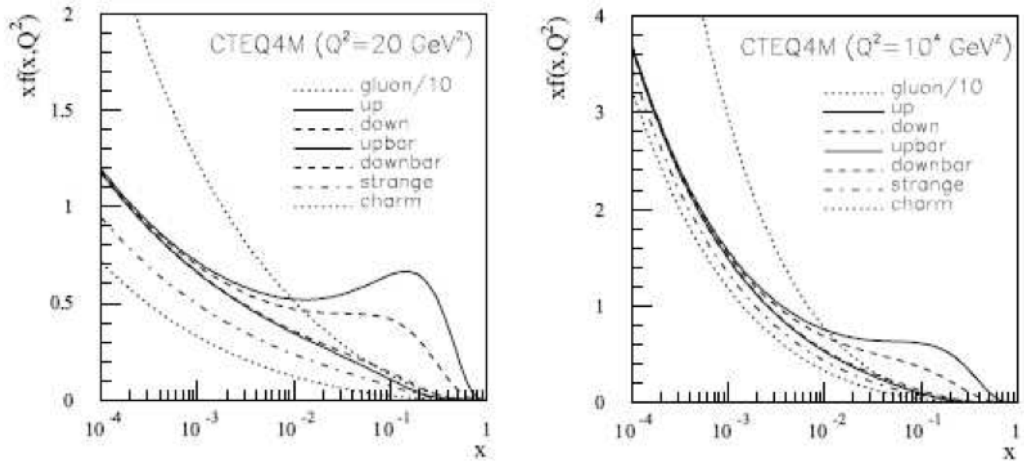
Figure 1.2: *Parton density functions for $Q^2 = 20$ GeV/c^2 (left) and $Q^2 = 10^4$ GeV/c^2 (right) .*

an unknown energy: the proton remnants, that carry a sizable fraction of

Process	σ	Events/sec	Events/year
W→eν	20 nb	15	10^8
Z→ee	2 nb	1.5	10^7
t$\bar{t}$	1 nb	0.8	10^7
b$\bar{b}$	0.8 mb	10^5	10^{12}
H (m_H= 0.8 TeV)	1pb	0.001	10^4
H (m_H= 0.2 TeV)	20pb	0.01	10^5

Table 1.2: *Cross section and the number of events produced for a given process per experiment at a luminosity of L=2 10^{33} cm^{-2}s^{-1}*

the proton energy, are scattered at small angles and are predominantly lost in the beam pipe (escaping undetected). Experimentally, it is therefore not possible to define the total and missing energy of the event, but only the total and missing transverse energies (in the plane transverse to the beams). Moreover, the center of mass may be boosted along the beam direction. It is therefore very useful to use experimental quantities that are invariant under boosts as the transverse momentum p_T or the *rapidity (y)*. The rapidity (choosing the beam direction as z axis) is defined as:

$$y = \frac{1}{2} ln \frac{E + p_z}{E - p_z} \tag{1.3}$$

and it is often used to describe angular distributions because it is additive under boosts along the z direction. For ultra-relativistic particles ($p \gg m$) the rapidity is approximated by the *pseudorapidity*:

$$\eta = -\ln \tan \frac{\theta}{2}, \tag{1.4}$$

where θ is the angle between the particle momentum and the z axis. The pseudorapidity can be reconstructed just from the measurement of the θ angle and can be also used for particles for which the mass and momentum are not measured.

1.1.2 Experiments at LHC

As already said in the previous section, the LHC experiments have to operate in very difficult conditions. In this challenging environment, four experiments have been installed. Two of them are devoted to specific topics: ALICE [3] to heavy ions and LHC-b [4] to b-physics. The other two are

the general-purpose experiments ATLAS [5] and CMS [6]. CMS and ATLAS are designed to cover the widest possible range of physics at the LHC. The difference between them is in the technical solution adopted. Their design reflects the different choice for the magnetic field configuration: CMS uses a solenoidal field generated by a big superconducting solenoid, while ATLAS uses a toroidal field produced by three sets of air-core toroids complemented by a small inner solenoid. ATLAS has the advantage that the track p_T resolution is constant as a function of the pseudorapidity. A very large air-core toroid allows a good momentum resolution even without the aid of the inner tracker. However, it requires an excellent alignment. CMS, on the other hand, can generate a very intense field. The resulting system is very compact and allows calorimeters to be installed inside the magnet, improving the detection and energy measurement of electrons and photons. Precise tracking exploits both the constant field within the magnet and the field inside the return yoke. Multiple scattering within the yoke, however, degrades the resolution of the muon system. Schematic pictures of CMS and ATLAS are shown in Fig.1.3 and Fig.1.4, respectively. The CMS experiment is described in details in Chapter 2.
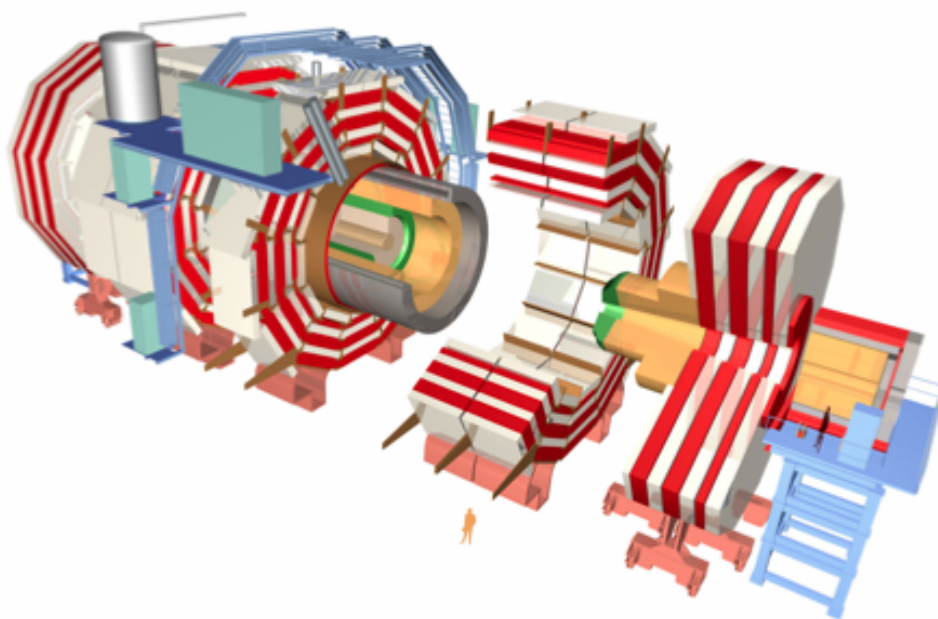
Figure 1.3: *The CMS detector*
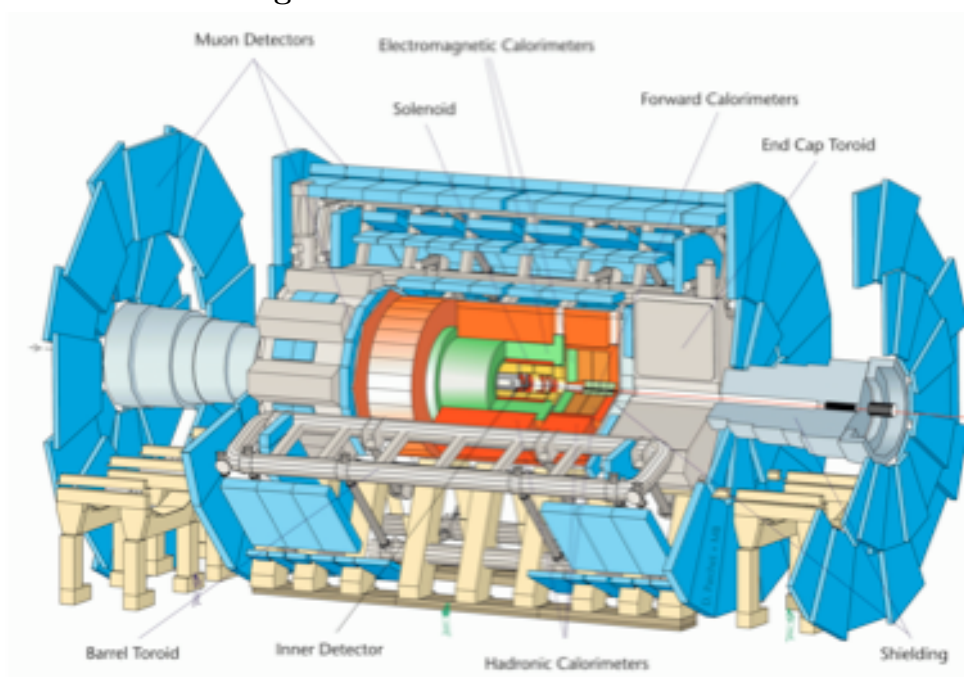
Figure 1.4: *The ATLAS detector*

1.2 The LHC Physics program

The physics investigation of the CMS experiment can be summarized on three main items:

- perform precision measurements in the electroweak sector (m_W, m_{top}, triple gauge couplings, $sin^2\theta_W$), in QCD, and in the CP violation and B physics sector. The top mass and the W mass have to be measured with a relative precision given by:

$$\Delta m_W = 0.7 \times 10^{-2} \Delta m_{top} \tag{1.5}$$

  in order to have a comparable impact in the determination of the Higgs mass from the fit of the electroweak observable. The target precision on these quantities is expected to be $\Delta m_W \leq 15$ MeV and $\Delta m_{top} \leq 2$ GeV.

- study the mechanism that breaks the symmetry of the Standard Model lagrangian giving rise to the particle masses. Assuming a SM Higgs boson, this means to search for a resonance from $m_H = 100$ GeV up to $m_H = 1$ TeV. If the Higgs is found, understand if it has the same properties predicted by the SM; otherwise look for alternative models.

- search for new physics, especially if the Higgs is not found. Concerning supersymmetry, all the *s*-particles with mass $m_{\tilde{s}} \leq 3$ TeV will be accessible. For exotic models (like lepto-quark, technicolor, new strong interaction, new lepton families, additional bosons, extra-dimensions) the mass range increases up to 5 TeV.

1.2.1 Measurement in the electroweak sector

As seen in figure 1.1, the cross sections of W and Z bosons production at LHC is huge: $\sigma(pp{\to}W{\to}l\nu) \sim$20nb and $\sigma(pp \to Z \to ll) \sim$ 2nb. The W and Z bosons are known since long time and their decay processes have been measured with high accuracy in previous experiments: nevertheless these processes are playing a key role, allowing to test the detector performances (calibration of the scale of charged particles momentum, calibration of the calorimeters energy scale, alignment of the detector, expecially the inner tracker, and understanding of the track reconstruction) and to tune the Monte Carlo.

A deep study of Z and W events will also improve the knowledge of the Parton Distribution Functions at LHC scale and it will provide a raw luminosity monitoring. The actual knowledge of the PDF derives mainly from deep inelasting scattering experiments (like H1 and ZEUS). The extrapolation of those functions to the LHC energy scale is one of the main systematic uncertainties in the measurement of the cross section of a physics process [7]. Using the angular distribution of the leptons produced from pp → WX and pp → ZX decays is possible anyway to reduce this uncertainty. A comparison between the accessible kinematic region in the old experiments and LHC is shown in Figure 1.5.
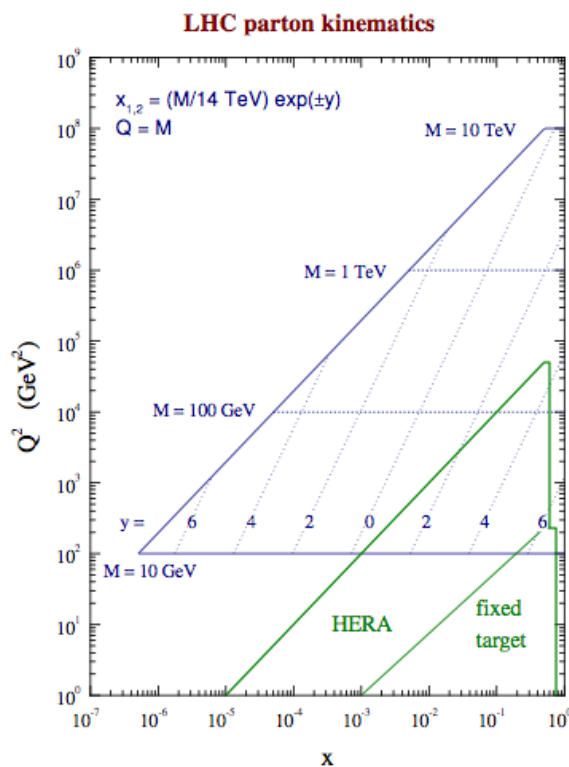
Figure 1.5: *Kinematic region in the (x, Q^2) plane, accessible at LHC.*

1.2.2 The SM Higgs search

In the Standard Model the elementary particles acquire their mass through the Higgs mechanism. This mechanism foresees the existence of the Higgs boson, a scalar particle which couples to massive particles. Its mass is the only yet unknown parameter of the SM.

The main processes which contribute to the Higgs production in a pp collision at the energy scale reached by LHC are shown in the diagrams in Figure 1.6. The fundamental interaction takes place between the partons, i.e. quark and
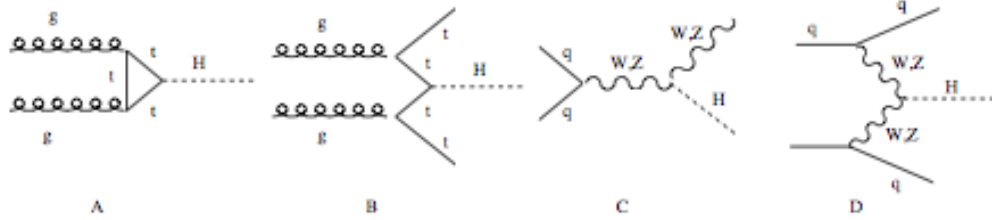
Figure 1.6: *Higgs boson production mechanisms at tree level in proton-proton collisions: gluon-gluon fusion (a), ttH associated production (b),W and Z associated production or Higgsstrahlung (c), VV fusion (d).*

gluons: the gluon fusion is the dominant process on the whole m_H spectrum and only at very high masses the vector boson fusion becomes comparable. Once produced, the Higgs can decay in different ways, according to its mass. The branching ratios for different decay channels as a function of the Higgs mass are shown in Figure 1.7.

Three different scenarios are possible:
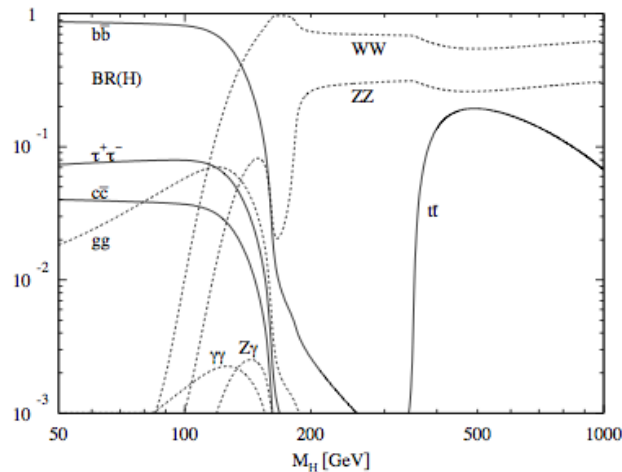
Figure 1.7: *Branching ratios for different Higgs boson decay channels as a function of the Higgs boson mass.*

- Low Higgs mass ($m_H \leq 130$ GeV): the heaviest available fermion is the b quark and H $\rightarrow b\bar{b}$ dominates. However this decay channel will

be unobservable because of the huge QCD background. In this mass region the most promising channel is H $\to \gamma\gamma$, which despite the very low branching ratio ($\sim 10^{-3}$) has a very clean signature. Excellent photon energy and angular resolution are required as well as good π_0 rejection.

- Intermediate Higgs mass ($m_H \geq 130$ GeV and $m_H \leq 500$ GeV): The production of WW and ZZ pairs becomes possible; the Higgs decay in four leptons is the golden channel. Even with a low branching ratio, it has a clean final state and does not suffer from irreducible background.

- High Higgs mass ($m_H \geq 500$): The cross section becomes low and semi-leptonic lνjj and lljj final states have to be used. The Higgs width becomes also very broad so that the reconstruction of a mass peak becomes difficult.

1.2.3 Search for new physics

1.2.3.1 Supersimmetry

Supersymmetry (SUSY) is a theory that introduces a new symmetry between bosons and fermions [8]. SUSY predicts that each particle has a supersymmetric partner whose spin differs by one half. The simplest supersymmetric model, called the Minimal Supersymmetric Standard Model (MSSM), predicts the existence of two Higgs doublets. it corresponds to five Higgs particles: two charged bosons (H$\pm$), two scalar bosons (h and H) and one pseudoscalar (A). At tree level, all masses and couplings depend on two parameters, chosen to be the mass of the A boson, m_A, and the ratio of the vacuum expectation values of the two Higgs doublets, tanβ. Charged Higgs bosons decay predominantly to τ ν. For the neutral Higgs bosons, the decays to vector bosons are suppressed, so that the golden channels described for the case of a SM Higgs will not be observable. The dominant decays modes are those to b$\bar{b}$ and $\tau^-\tau^+$ but the former is hidden by the large background of b-jets. The observation of MSSM Higgs bosons will therefore rely on the identification the leptons coming from τ decays and of τ-jets.

1.2.3.2 New massive bosons

The discovery of an object like a Z' boson will be very likely limited by the statistical significance of the signal. Ways of distinguishing between different models involve the measurement of the natural width and the forward-backward asymmetry, both of which require sufficiently good momentum

resolution at high p_T to determine correctly the sign of the leptons and a pseudorapidity coverage up to $\eta = 2.4$.

The detector requirements for high momenta can be determined by considering decays of high-mass objects such as Z' $\rightarrow e^+e^-$ and $\mu^+\mu^-$.

1.3   Z boson Production at LHC

Z bosons production at LHC proceeds mainly via the Drell-Yan process. The dominating processes at the LHC are:

$$q\bar{q} \longrightarrow Z/\gamma* \longrightarrow l^+l^- \text{ Leading order } 65\% \tag{1.6}$$

$$qg \longrightarrow q\gamma * /Z \longrightarrow ql^+l^- \text{ NLO order } 35\% \tag{1.7}$$

The dominant higher order correction of the first process is the scattering of a quark with a gluon, which contributes roughly 1/3 of the overall cross-section of this process. The Feynman diagrams (1.6,1.7) are presented in Fig. 5.1, for the $\mu\mu$ decay only.

The backgrounds arise from isolated leptons originating from other elec-
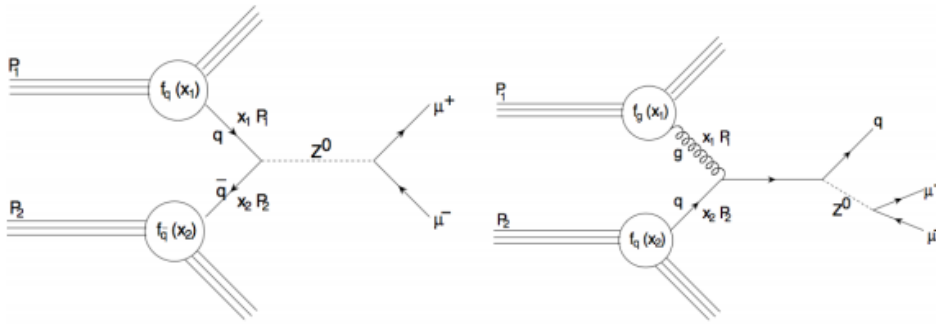
Figure 1.8: *Feynman diagrams of the Drell-Yan process decaying into two muons. On the left the Leading order diagram, while on the right one of the NLO diagram.*

troweak boson production processes and leptons (real or misidentified) originating from QCD jet or jet $+\gamma$ production. The most important backgrounds are then:

- di-jets

- $t\bar{t}$

- W+jets

- Z$\longrightarrow \tau\tau$

- jet $+\gamma$

1.4 Diffractive Physics

An hypothesis of the composition of the total LHC cross section σ_{TOT} is presented in Fig. 1.9. The diffractive reactions such as AB → XY are a
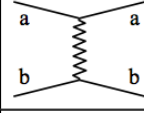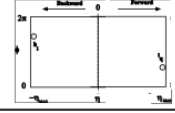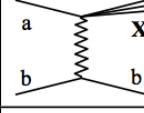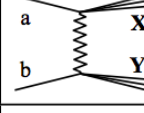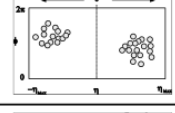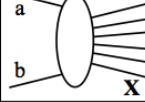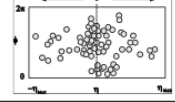
Figure 1.9: *Composition of the total cross section σ_{TOT} at LHC.*

considerable (∼25%) fraction of the total cross section. The X,Y terms can be either the initial, scattered hadrons or a low mass states which may be a resonance or a continuum state. In all cases, the energy of the outgoing hadrons or the state X,Y is approximately the energy of the incoming particle, to within few percent. The two final states particles are well separated in phase-space and have a *large rapidity gap* (LRG) between them.
Historically, the diffractive hadron-hadron scattering has been described using the Regge theory [9],[10]. The exchange of particles in the t-channel is summed coherently to give the exchange of the so called "Regge Trajectories". Diffraction is characterized by the exchange of a specific trajectory, called the "Pomeron (IP)". The Pomeron has the quantum numbers of the vacuum and no color. The exchange of the Pomeron implies no additional hadronic production.

1.4.1 Introduction

Let's consider the following example (fig 1.10):

$$\pi^- p \to \pi^0 n \tag{1.8}$$

The conservation of the quantum numbers implies that this process might
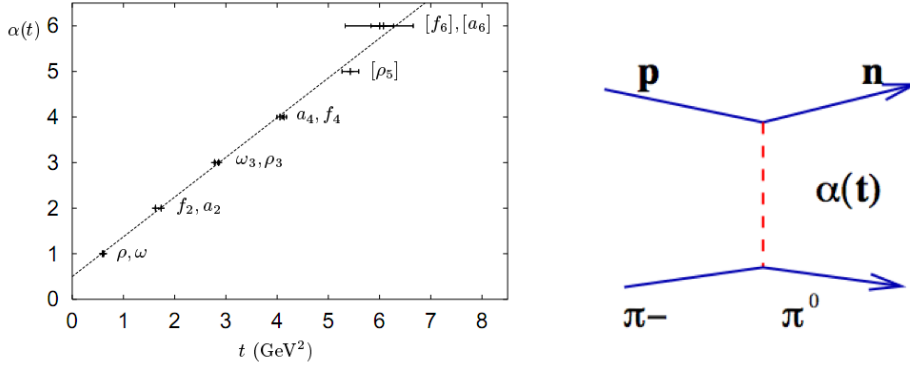
Figure 1.10: *Schematic diagram for $\pi^- p \to \pi^0 n$ scattering and the exchanged trajectory.*

happen via the exchange of a virtual hadron like ρ, a_2, g,..., hadron. The values of masses and spins of these particles lie almost on a straight line in the mass-spin plane, determining the "trajectory" of the particles.
The general parametrization of this line is:

$$\alpha(t) = \alpha(0) + \alpha' t \tag{1.9}$$

The most important trajectories are at first approximation all linear with a common slope. The first particle of the line is the one that gives the name to the trajectory (ρ trajectory in this case).
Regge's theory predicts the properties of a t-channel reaction (that happens on the left hand side of the spin-t plane, where t is negative, via the exchange of the off-mass shell particles). In the example, the reaction is determined by the parameters of the trajectory formed by the exchanged particles on the right-side of the spin-t plane.
The formula (1.9) can be derived in Regge theory from the analytic continuation of the partial-wave amplitudes to complex values of the angular momentum. The relativistic scattering amplitude A(s,t) in the t channel can be written in the high energy limit as:

$$A(s,t) \sim -\sum_i \beta_i(t) \frac{\eta_i}{sin\pi\alpha_i(t)} s^{\alpha_i(t)} \tag{1.10}$$

where the sum is over the poles of the amplitude in the complex l plane (so called "Regge Poles"), while β are the residues at each pole and $\alpha(t)$ their location. The function $\alpha(t)$ are the Regge trajectories. Expanding $\alpha(t)$ in

power of t we obtain the 1.9.

Each Regge trajectory is called a "Reggeon"(IR), which corresponds to a family of resonances with a certain set of quantum numbers.

1.4.1.1   The Pomeron And Total Cross Section

Among the Regge trajectories which characterize diffraction events, the Pomeron is the most interesting: it is needed to explain the behavior of the total cross section with energy. According to Regge theory, the dependence of the total cross section (a t-channel process) is parametrized as:

$$\sigma_{TOT} \approx \frac{ImA(s, t=0)}{s} \sim \sum_i A_i s^{\alpha_i(0)-1} \tag{1.11}$$

where $\alpha_i(0)$=1,..,n are the intercepts of the trajectories exchanged. Using only two main categories, σ_{TOT} for pp, p$\bar{p}$, $K^{\pm}$p, $\pi^{\pm}$p, have been fitted by Donnachie and Landshoff [12] with an expression of the form:

$$\sigma_{TOT}(s) = X_s^{\alpha_{IP}(0)-1} + Y_s^{\alpha_{IR}(0)-1} \tag{1.12}$$

where X and Y are parameters that depend on the exchanged field. The pomeron trajectory has an intercept of $\alpha_{IP}(0)$=1.0808 while the second term, which represents an effective meson trajectory, has an intercept of $\alpha_{IR}(0)$=0.545. At high energy, only the pomeron term is important. The pomeron, identified as the first particle of the pomeron trajectory, is then responsible for the rise of the total cross section as a function of the center of mass energy.

In Fig. 1.11 the total cross section for pp, p$\bar{p}$, $\pi^{\pm}$p, as a function of $\sqrt{s}$ is presented. It is remarkable that such a simple fit works well from low to very high energies. When Donnachie and Landshoff first made these fits to total cross sections, the higher energy data from the CERN collider and the Tevatron were not available, but their predictions based on Regge theory are successful.

For reggeon and pomeron exchange, the probability to have a large rapidity gap $\Delta\eta$ between the initial particles has the form [13]:

$$p(\Delta\eta) = e^{-2(\alpha(0)-1)\Delta\eta} \tag{1.13}$$

There are three different possibilities:

- IP exchange: $\alpha(0) \sim 1 \Rightarrow$ p=e^0
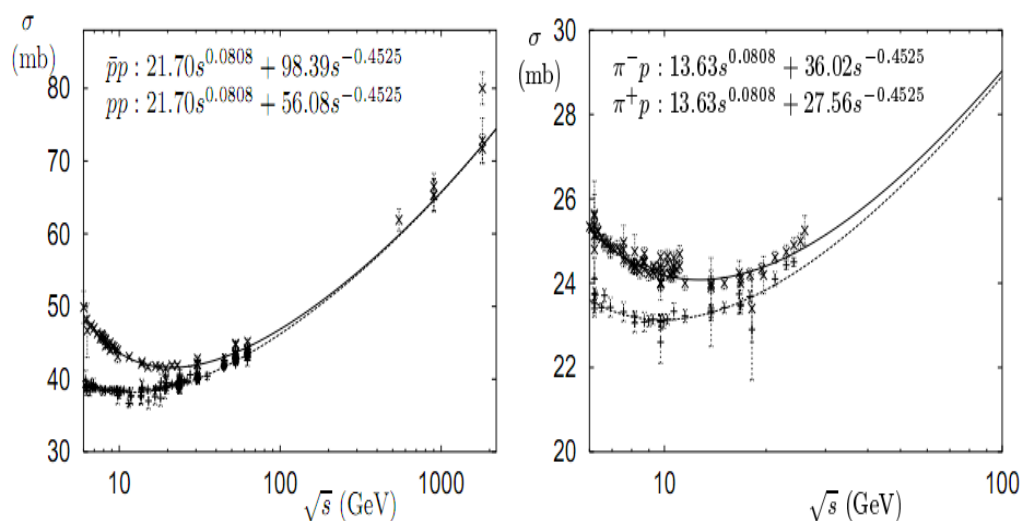
Figure 1.11: *Fits to the total cross section for pp, $p\bar{p}$, $\pi^{\pm}p$, as a function of $\sqrt{s}$.*

- ρ,a2,f2,ω exchange: $\alpha(0) \sim 0.5 \Rightarrow$ p=$e^{-\Delta\eta}$

- π exchange $\alpha(0) \sim 0 \Rightarrow$ p=$e^{-2\Delta\eta}$

Therefore, only pomeron exchange produces rapidity gaps that are not suppressed at the gap width increases. It is possible to define operationally the diffraction by the presence of rapidity gaps in the final space phase.

1.4.2 Hard Diffraction

At higher energies, some additional reactions such as high p_T jet production were observed in diffractive scattering. Ingelman and Schlein [14] proposed that the observation of jets in diffractive events would probe the partonic nature of the exchanged object, whether it is the pomeron or something else. They assumed that the pomeron can be treated as an object that exists within a proton, and that it is thus sensible to define a flux of pomerons in the proton as well as a pomeron structure function. With these assumptions they were able to make predictions for diffractive jet production cross sections and their properties.

The first evidence of diffraction with a hard scale was found by the UA8 collaboration [11] at the CERN SPS collider (proton-antiproton collisions at s = 630 GeV). There, the production of high-energy transverse deposits

along with a fast proton carrying a large fraction of the incoming beam energy was observed in the single-diffractive reaction pp→pX. The outgoing protons were measured by special detectors, located along the beam line, called Roman Pots. Their momentum was determined from the measurement of their deflection.

Recently, diffraction has been extensively studied at HERA and Tevatron colliders, improving the understanding of hard-diffractive processes. The description of diffraction in terms of QCD has opened the way to a rich physics program, and to a more complete understanding of the theory of strong interactions.

1.4.3   Large Rapidity Gap

In diffractive scattering, the hadronization of the final states X and Y with masses M_X^2 and M_Y^2 happens independently. If the center of mass energy $\sqrt{s}$ is large enough ($\ln(s) >> \ln(M_x^2) + \ln(M_Y^2)$), then there is a gap in rapidity in between X and Y, as sketched in Fig. 1.12.
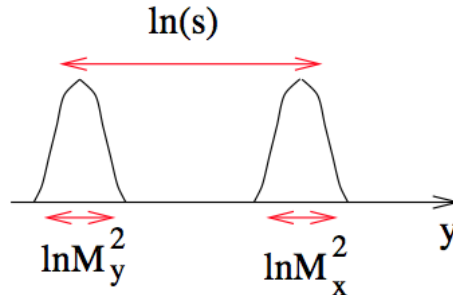
Figure 1.12: *Energy flow as a function of the rapidity.*

Ln(s) quantify the number of rapidity units covered by the events. For the LHC machine, given the high energy available in the center of mass, this number corresponds to ~ 18 rapidity units. In terms of pseudorapidity, the diffuse protons are deflected at $\sim \pm 10$ units, as it is clearly visible from the simulation in Fig. 1.13.

The $\ln(M_X^2)$ and $\ln(M_Y^2)$ define instead how wide is, in units of pseudorapidity, the dispersion of the particles after the hadronization. If the M_Y, M_X masses are high (like for a diffractive Z boson production), the particles can easily cover a large zone of the CMS detector total acceptance ($|\eta| \leq 5$). For example, if the $M_{X,Y}$ is supposed to be twice the Z boson mass, then dispersion would cover ~ 10 rapidity units.
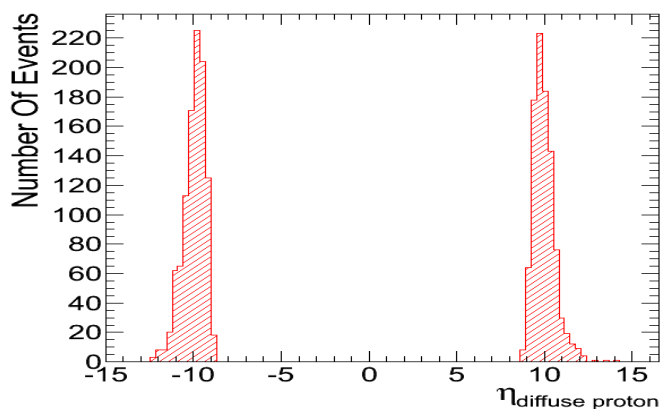
Figure 1.13: *Pseudorapidity of the diffuse proton, simulated using PomPyt Monte Carlo.*

A typical energy flow as a function of the pseudorapidity for a single diffractive scattering at LHC is presented in figure 1.14.
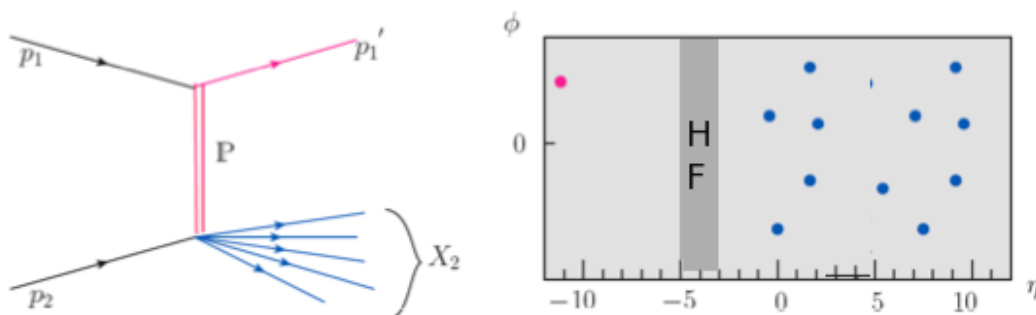
Figure 1.14: *Energy flow Vs pseudorapidity at LHC for single diffractive events.*

Aside for the diffractive proton (pink point on the left), a group of particles formed during the hadronization of the other proton is visible within the CMS detector ($|\eta| \leq 5$). In this example the LRG is detected because none of the particles hit the HF- calorimeter ($-5 \leq \eta \leq -3$, dark grey area). Considering the available M_X^2 at LHC, a not negligible fraction of events is produced in such a way to cover the total detector acceptance, and thus to neutralize the selection provided by the LRG.

The diffractively scattered protons carry an average energy of 99 percent of their initial momentum (x_L). Figure 1.15 schematically shows the spectra of protons generated from different mechanisms: at x_L close to 1 single diffrac-
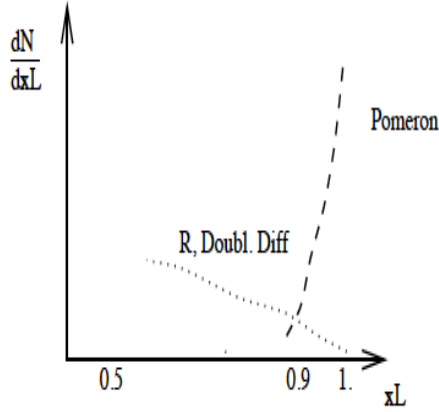
Figure 1.15: *Spectra of protons generated from different mechanisms: pomeron exchange (dashed line) and Reggeon exchange and double diffraction (dotted line).*
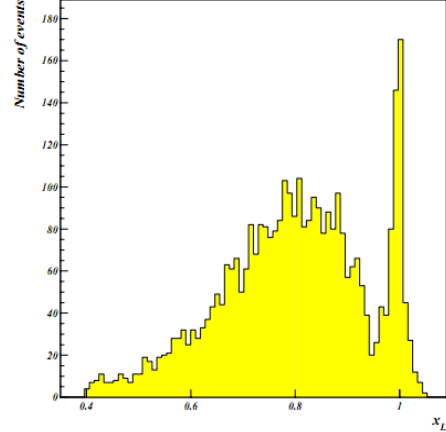
Figure 1.16: *Fraction xL of the incoming proton momentum carried by the diffractively scattered proton.*

tion is almost the sole component. Moving away from this point, double diffraction and Reggeon exchange become important.

Traditionally it has been decided to arbitrary assign x_L=0.9 as the point in which the diffractive and not diffractive part of the spectrum are equal.

1.4.4 Single Diffractive Production of Z bosons

In the reaction pp $\rightarrow$ Xp, X can contain a Z boson. The Z$\rightarrow l^+ l^-$ decay mode is sensitive to the diffractive structure function of the proton, notably its quark component since bosons originate from quark fusion (figure 1.17). Hard diffractive hadron-hadron cross sections are unfortunately suppressed due to the effect of rescattering between the spectator partons of the beam particles, quantified by the so called rapidity gap survival probability.

1.4.4.1 Single Diffractive production at Tevatron

Measurements of soft and hard diffractive processes have been performed at the Tevatron p$\bar{p}$ collider in the last two decades. In Run I (1992-1996) at an energy of $\sqrt{s} = 1.8$ TeV and in Run II (2003-present) with the new upgrade ($\sqrt{s}$=1.96 TeV), the exclusive production rate have been studied by tagging
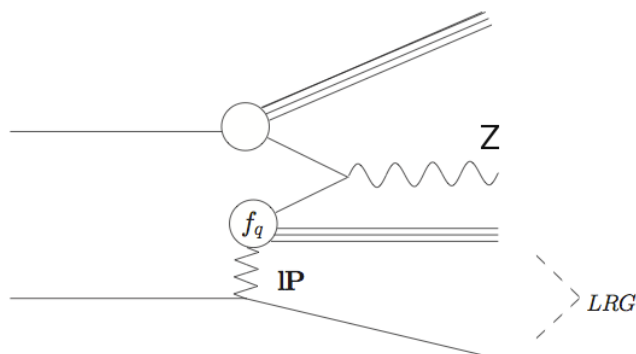
Figure 1.17: *Sketch of the single-diffractive reaction pp → Xp in which X includes a Z boson.*

events either with a rapidity gaps or with a leading hadron.

The experimental apparatus includes a set of forward detectors [15]: the miniplug calorimeters which cover the pseudorapidity of $3.5 < |\eta| < 5.1$; the Beam Shower Counters which surround the beam pipe at region of $5.1 < |\eta| < 7.4$; the Roman Pot Spectrometer tagging the leading hadron scattered from the interaction point.

In Run I, CDF measured the fraction of events with di-jets, W bosons, b quarks, or J/Ψ [16] which are produced diffractively, and found in all cases a fraction of approximately 1% of the total rate. In Run II, using the Roman Pots to remove the ambiguity of the gap survival probability, the new ratio has been settled to $R_W = 0.97 \pm 0.05$ (stat) ± 0.10 (sist) % and for the Z boson to $R_Z = 0.85 \pm 0.20$ (stat) ± 0.08 (sist) %. [17]

D0 experiment also studied both diffractive bosons production in Run I and it founded a diffractive fraction, uncorrected for gap survival,of $(1.44^{0.61}_{0.52})$% for Z boson. However, the gap survival estimated by D0 using MonteCarlo simulations was (21 ± 4)%, which would yield W and Z fractions approximately four times larger than those of CDF.

Chapter 2

The Compact Muon Solenoid

The CMS detector has been built to identify precisely the properties of muons, electrons and photons. Jets also need to be measured. Neutrinos and other very weakly interacting particles escape without leaving signals: they can only be measured indirectly through the determination of missing transverse energy, which requires a hermetic detector. Therefore CMS must cover as much of the solid angle as possible. For this purpose, new forward detectors have been added to the original CMS design.
In this chapter we will present a general description of every subdetectors allowing CMS to fullfill its design goal.

2.1 CMS Detector

A transverse section of the CMS detector is shown in Fig. 2.1, while the general layout has been already presented in Fig. 1.3. The detector is divided in two parts: a cylindrical Barrel closed by two Endcap disks. The overall length is 21.6 m, the diameter 14.6 m and the total weight about 12500 tons. The coordinate system used to describe the detector is a right-handed frame where the x axis points to the centre of the LHC ring, the y axis points upward and the z axis is parallel to the beam, with the origin at the nominal interaction point.
Starting from the interaction point, a series of subdetectors forms the "onion-like" CMS layout. The innermost is the silicon pixel vertex detector with three layers in the Barrel (43 mm from the interaction point) and two disks in each Endcap. The main aim of this subdetector is to reconstruct precisely the position of the interaction point and decay vertices.
Outside the pixel detector the silicon strip detector extends up to a radius of 1.2 m. Together with the pixel detector it is used to reconstruct the charged
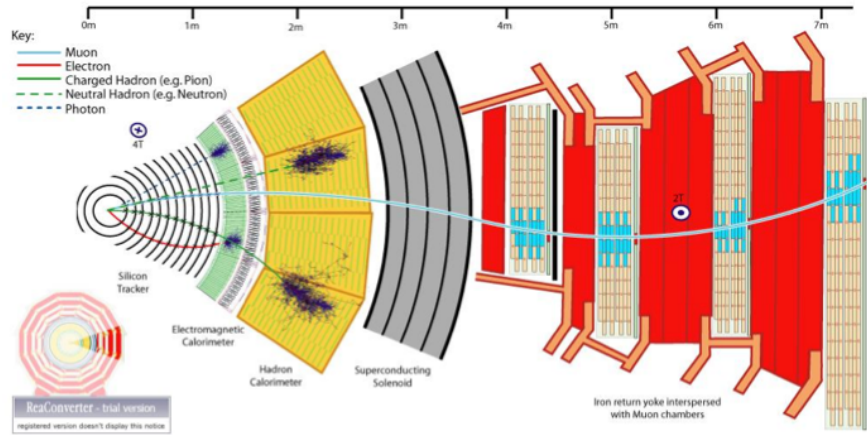
Figure 2.1: *The CMS detector transverse section.*

tracks.

The electromagnetic calorimeter (ECAL) is located outside the tracker. It is a homogeneous device consisting of a large number of scintillating crystals that are read out using avalanche photo diodes or vacuum phototriodes. Its purpose is the precise measurement of the energy and position of electrons and photons. In the Endcap region a preshower detector is placed in front of the ECAL in order to provide neutral pions/photons separation.

The hadronic calorimeter (HCAL) is placed after ECAL. It is a sampling calorimeter consisting of copper absorber plates interleaved with scintillator sheets. Its purpose is the reconstruction of energy and position of hadrons and jets.

All these subdetectors are contained inside a superconducting solenoid magnet. This magnet is the main feature of CMS detector: 13 m long, 5.9 m in diameter and producing an uniform magnet field of 3.8 T. It is cooled with liquid helium.

The very forward hadronic calorimeter (HF) extends the coverage of the detector.

The muon system is embedded in the iron return yoke of the magnet, outside the coil. Three different technologies are used: drift tubes in the Barrel, cathode strip chambers in the Endcaps and resistive plate chambers to measure the bunch-crossing timing. All three subdetectors are used in the trigger and in the reconstruction of muon tracks.

In Fig. 2.1 it is represented the interaction of the various particles traversing the CMS detector. Muons easily traverse the entire detector, leaving tracks

in the inner tracker and in the muon chambers, and depositing almost no energy in the calorimeters.

Electrons and photons deposit all their energy producing electromagnetic showers in the crystals of ECAL. Electrons are charged particles therefore they leave tracks in the tracker while photons, since they are neutral particles, they leave no traces in the tracker. Hadrons such as pions or neutrons produce large showers in the calorimeters. Unless they are very energetic, they dissipate all their energy before reaching the muon chambers.

In the following sections a description of every subdetector listed previously is presented.

2.2   The Inner Tracking System

The tracking system should measure the particle transverse momentum p_T with an high resolution. The trajectory of a particle with transverse momentum p_T and charge z inside a magnetic field B is an helix with radius R. The relation among these quantities is:

$$p_T = 0.3 \cdot z \cdot B \cdot R \qquad (2.1)$$

where p_T is expressed in GeV, B in T e R in m.

Generally, the particle transverse momentum resolution can be written as:

$$\frac{\sigma_{p_T}}{p_T} = C_1 \cdot p_T \oplus C_2 \qquad (2.2)$$

the term C_2 contains the multiple Coulomb scattering effects; C_1 depends on the detector geometry, in particular from the number of points used for the track reconstruction (n), its length (L), and the resolution on the single point measurement (σ_x).[1]

The resolution σ_x on the measured point is given by:

$$\sigma_x = \sqrt{\sigma_{int}{}^2 + \sigma_{syst}{}^2} \qquad (2.3)$$

where σ_{int} is the intrinsic resolution of the detectors and the other term the systematic error given by the unknown spatial position of hit module and can be minimized by alignment procedures.

The CMS tracker is composed of a pixel detector with three Barrel layers at radii between 4.4 cm and 10.2 cm and a silicon strip tracker with ten Barrel detection layers extending outwards to a radius of 1.1 m. Each system is

---

[1]$C_1 \sim \frac{\sigma_x}{BL^2\sqrt{n}}$

completed by Endcaps which consist of 2 disks in the pixel detector and 3 plus 9 disks in the strip tracker on each side of the Barrel, extending the acceptance of the tracker up to a pseudorapidity of 2.5.

The performance of the tracker is illustrated in Fig.2.2 which shows the transverse momentum resolution in the r-ϕ and r-z planes for single muons with different p_T, as a function of the pseudorapidity.
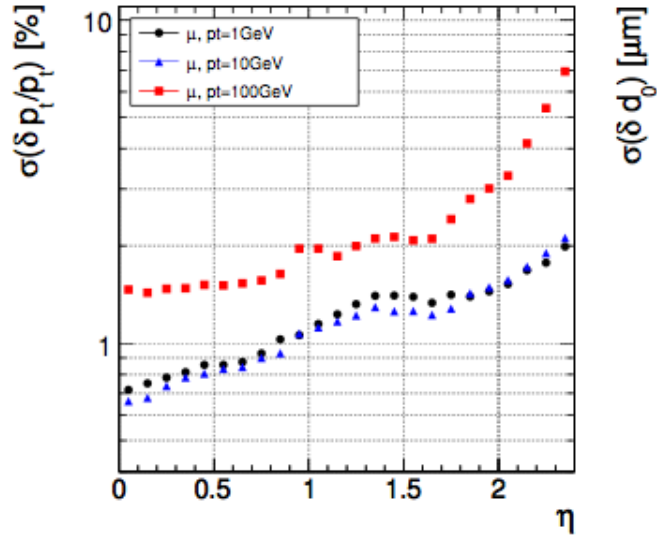
Figure 2.2: *Tracker resolution for single muons with transverse momentum of 1, 10 and 100 GeV/c, as a function of pseudorapidity.*

2.2.1   The Pixel Tracker

The pixel Tracker consists of three 53.3 cm long Barrel layers and two Endcap disks on each side of the Barrel section (Fig.2.3). The innermost Barrel layer has a radius of 4.4 cm, while for the second and third layer the radii are 7.3 cm and 10.2 cm. The detector is made of of 4.4 millions of n-type silicon pixels with a size of 100 μm x 150 μm.

The sensor are read-out analogically and a spatial resolution of $\sim$ 10 μm for the $r - \phi$ coordinate and of $\sim$ 20 μm for the $r - z$ measurement can be obtained. This precision is achieved interpolating the charge induced in nearby pixels, helped by the large Lorentz drift angle in the magnetic field. The short distance from the interaction point imposes special requirements on radiation hardness and will probably require the substitution of the pixel detector during the lifetime of the experiment.
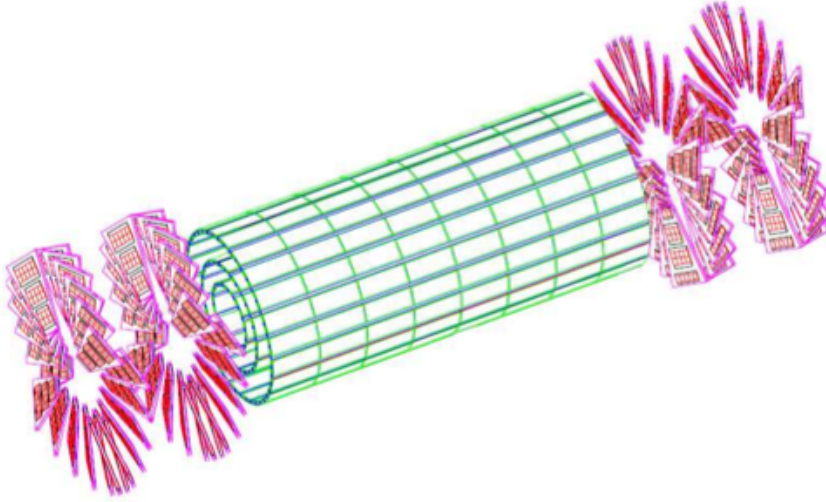
Figure 2.3: *Schematic view of the Pixel Tracker.*

2.2.2 The Strip Tracker

The strip tracker is composed of 10 layers of silicon microstrip detectors. The layout is shown in Fig.2.4.

The silicon strip tracker covers a tracking volume up to r = 1.1 m with a length of 5.4 m and is divided in four parts: the Tracker Inner Barrel (TIB), the Tracker Outer Barrel (TOB), the Tracker End-Cap (TEC) and the Tracker Inner Disks (TID).

The TIB is composed by four layers of n-type silicon sensors with a thickness of 320 μm and strip pitches varying from 80 to 120 μm. The first two layers are made with double sided (stereo) modules, composed by two detectors mounted back to back with the strips tilted by 100 mrad. The single point resolution of this sensors in both rϕ and rz coordinates is between 23 and 34 μm and 230 μm respectively.

The TOB is made of six layers. The lower radiation levels allows the use of thicker silicon sensors (500 μm). The strip pitch varies from 120 to 180 μm. Also the first two layers of the TOB provide a "stereo" measurement with a single point resolution which varies from 35 to 52 μm in the $r - \phi$ direction and 530 μm in z.

The TID is made of three disks, filling the gap between the TIB and the TEC. the TEC comprises nine disks that extend into the region 120 cm $\leq$ $|z| \leq$ 280 cm. Both parts are composed of wedge shaped modules arranged in rings, centred on the beam line, and have strips that point towards the
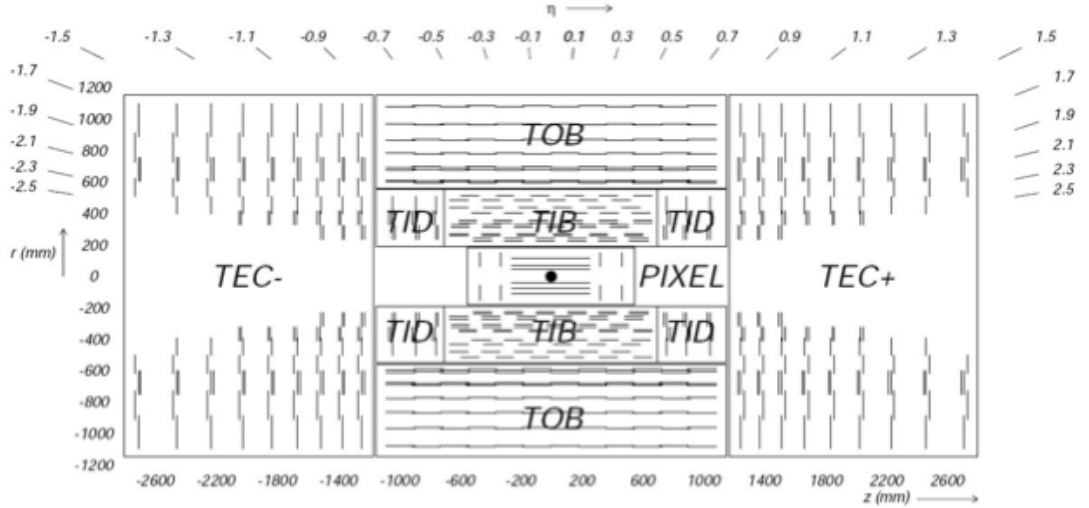
Figure 2.4: *Schematic cross-section of the Inner Tracking System showing also the η ranges of the different cross sections.*

beam line.

The entire silicon strip detector consists of about 15400 modules, which are mounted on carbon-fibre structures and housed inside a temperature controlled (-20 °C) support tube.

2.3   The Calorimeters

The calorimeters measure energies of both neutral and electrically charged particles. Electrons, positrons and photons, via electromagnetic interaction, deposit all their energy by showering in the innermost section of the calorimeter, the electromagnetic calorimeter (ECAL).

After ECAL, the hadronic calorimeter (HCAL) measures the hadronic showers and energies of jets and provides further containment and hermeticity for the determination of missing energy. In order to reach a large rapidity coverage the Barrel part (HB) and the Endcap parts (HE) are complemented by two forward hadron calorimeters (HF) on each side of the detector. An outer hadron calorimeter (HO), made of an additional layer of scintillator, has been included in the Barrel region, just outside the coil, to maximize the number of interaction lengths and thus to prevent punch-through of hadronic showers into the muon system as much as possible.

2.3.1   The Electromagnetic Calorimeter

An introductory description of the ECAL calorimeter is presented in this section, while a more detailed examination will be given in Chapter 3.

ECAL is a high-resolution, high-granularity detector made of lead tungstate (PbW0$_4$) crystals. Lead tungstate is a fast scintillator providing a small Molière radius and short radiation length.

ECAL can achieve a good mass resolution: the detector design was tuned on the investigation of the two-photons decay of a Standard Model Higgs boson with a mass just above 114.4 GeV/c^2 (the limit reached at the LEP collider). The good rejection of π_0's decaying into two photons is provided by a preshower detector in the Endcap regions.

The geometrical crystal coverage extends up to $|\eta| = 3.0$, as shown in Fig.2.5. ECAL was equipped in the Endcap region with the preshower detectors, that
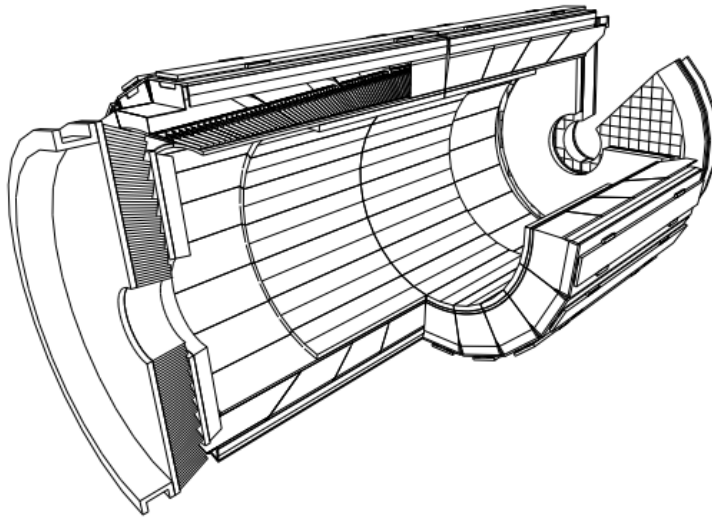
Figure 2.5: *Schematic view of the ECAL detector.*

consist of lead/silicon detector layers and cover a range of $1.65 < |\eta| < 2.6$. A parametrization of the energy resolution can be given by

$$\left(\frac{\sigma_E}{E}\right)^2 = \left(\frac{a}{\sqrt{E}}\right)^2 + \left(\frac{b}{E}\right)^2 + c^2 \tag{2.4}$$

where a is a stochastic term including fluctuations in the shower containment and in the number of photo-electrons, b describes noise caused by electronics or pileup energy, and c is a constant characterizing energy leakage and

intercalibration errors. The values of the three constants measured on test beams are reported in Table 2.1. The different contributions as a function of the energy are shown in Fig.2.6.

The crystals response is strongly temperature dependent. The temperature

Contribution	Barrel ($\eta = 0$)	Endcap ($\eta = 2$)
Stochastic term	2.7%	5, 7%
Constant term	0.55%	0.55%
Noise (low luminosity)	0.155 GeV	0.155 GeV
Noise (high luminosity)	0.210 GeV	0.245 GeV

Table 2.1: *Contributions to the energy resolution of ECAL.*
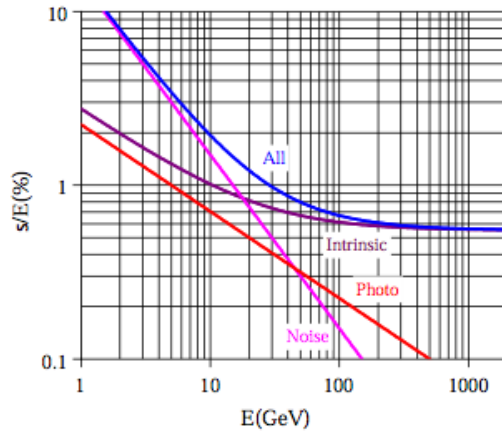
Figure 2.6: *Different contributions to the energy resolution of the ECAL as a function of the energy.*

of the ECAL system has therefore to be maintained constant to high precision, requiring a cooling system capable of extracting the heat dissipated by the read-out electronics and of keeping the temperature stable to preserve energy resolution. The nominal operating temperature of the detector is 18°.

2.3.2   The Hadron Calorimeter

The hadron calorimeters are particularly important for the measurement of hadron jets, neutrinos or exotic particles resulting in apparent missing transverse energy and in the forward physics studies.

The hadron calorimeter (HCAL) Barrel is radially comprised between the electromagnetic calorimeter (with an external radius R = 1.77 m) and the inner extent of the magnet coil (R = 2.95 m), as seen in (Fig.1.3). This limits the total amount of material which can be put in to absorb the hadronic shower. Therefore, an outer hadron calorimeter or tail catcher is placed outside the solenoid complementing the Barrel calorimeter.

HCAL ((Fig.2.7)) is divided in a central calorimeter ($|\eta| < 3$), containing the Hadronic Barrel (HB), the Hadronic Endcaps (HE), and the Outer Hadronic calorimeter (HO), complemented by the forward and backward calorimeters (HF) in the range $3 < |\eta| < 5$.

HCAL is a hadronic sampling calorimeter made of brass and stainless steel
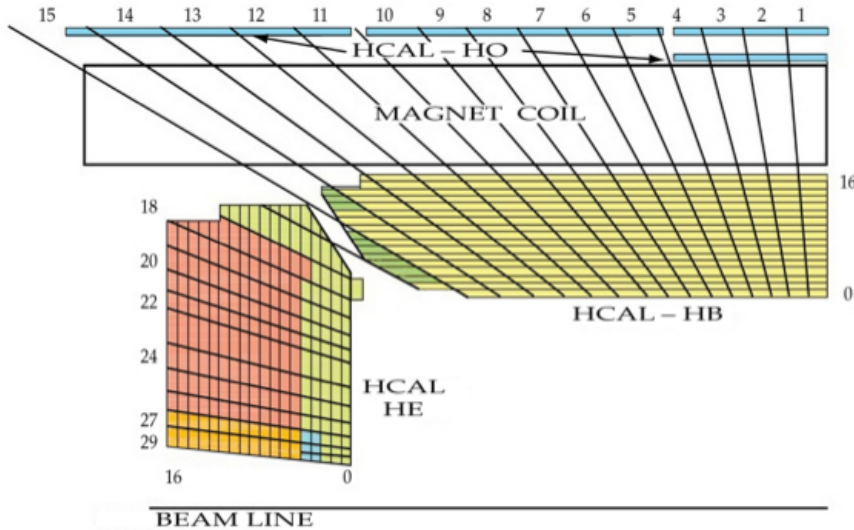
Figure 2.7: *The HCAL tower segmentation in the r,z plane for one-fourth of the HB, HO, and HE detectors. The shading represents the optical grouping of scintillator layers into different longitudinal readout.*

absorbers and plastic scintillators, with a dynamic energy range of 5 MeV to 3 TeV.

The HB is divided into two half Barrels, each containing 18 identical wedges. The wedges are made of absorber plates, complemented by 17 layers of plastic scintillators. The innermost and outermost absorber plates consist of stainless steel for stability reasons, the others are made of brass to maximize the hadronic interaction length. The granularity of the scintillators in the Barrel part is $\Delta\eta \times \Delta\phi = 0.087 \times 0.087$.

Each of the Hadronic Endcaps consists of absorber plates and scintillators

arranged in 10 sectors. There are 18 absorber layers of 80 mm thickness. As in the Barrel part, the innermost and outermost layer are made of stainless steel, while the others consist of brass. The scintillator granularity is the same as in the Barrel part, except for the highest η-regions. Here, the granularity matches that of the electromagnetic calorimeter.

The HO is placed outside the solenoid. It contains one sampling layer in the Endcap region, two layers in the Barrel region and an additional layer in the range of $\eta < 0.4$.

The total absorber thickness of the hadronic calorimeter is summarized in the table 2.2.

At the end, the HF calorimeters (positioned at a distance of about 11 m from

HCAL total absorber thickness	
Eta	Interaction length λ
$\eta = 0$	5.15
$\eta = 1.3$	9.1
Endcap	10.5

Table 2.2: *HCAL total absorber thickness.*

the interaction point) has been inserted for the identification and reconstruction of very forward jets. The region is characterized by an high radiation field: this leads to the choice of quarz fibres as active material. These fibres emit Cherenkov light, detected by photodiodes. They are placed between 5 mm thick steel absorber plates with a total thickness of 10 hadronic interaction lengths λ.

During test beam studies, the energy resolution of the CMS calorimeter system (including the electromagnetic calorimeter) for hadrons in the energy range 30 GeV$< E <$1 TeV was found to be:

$$\left(\frac{\sigma_E}{E}\right)^2 = \left(\frac{100\%}{\sqrt{E}}\right)^2 + (4.5\%)^2 \qquad (2.5)$$

2.4   The Superconducting Magnet

The CMS superconducting magnet [21], of 6 m diameter and 12.5 m length, has been designed to reach a 4 T field with a stored energy of 2.6 GJ at full current. The flux is returned through a 10,000 t yoke comprising 5 wheels and 2 Endcaps, composed of three disks each.

The distinctive feature of the 220 tons cold mass is the 4-layer winding made

from a stabilized reinforced N_bT_i conductor. The ratio between stored energy and cold mass is high (11.6 KJ/kg), causing a large mechanical deformation (0.15 percent) at energizing. The parameters of the CMS magnet are summarized in Table 2.3.

General Parameters	
Magnetic Length	12.5 m
Cold bore diameter	6.3 m
Central magnetic induction	4 T
Total Ampere-turns	41.7 MA - turns
Nominal current	19.14 kA
Inductance	14.2 H
Stored energy	2.6 GJ
Cold Mass	
Radial thickness of cold mass	312 mm
Radiation thickness of cold mass	3.9 X_0
Weight of cold mass	220 t
Maximum induction on conductor	4.6 T
Temperature margin wrt operating temperature	1.8 K
Stored energy/unit cold mass	11.6 kJ/kg
Iron Joke	
Outer diameter of the iron flats	14 m
Length of Barrel	13 m
Thickness of the iron layers in Barrel	300, 630 and 630 mm
Mass of iron in Barrel	6000 t
Thickness of iron disks in Endcaps	250, 600 and 600 mm
Mass of iron in each Endcap	2000 t
Total mass of iron in return yoke	10 000 t

Table 2.3: *Main CMS magnet characteristics.*

2.5   The Muon System

The muon spectrometer must provide an accurate measurement of the muon momentum and its charge, even without the contribution of the tracker system. It is all embedded in the iron return yoke of the magnet (Fig.2.8), which shields the detectors from charged particles other than muons. The minimum value of the muon transverse momentum required to reach the system is $\sim$ 5 GeV.
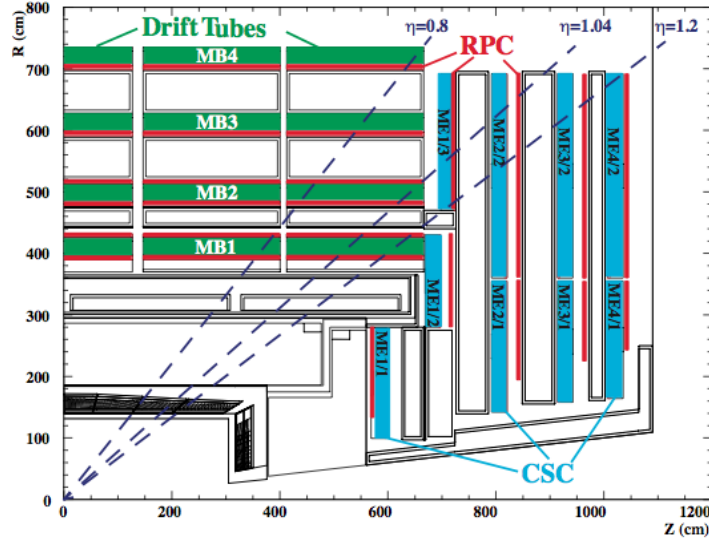
Figure 2.8: *The longitudinal view of the muon spectrometer.*

The muon spectrometer consists of three independent subsystems, described in the following sections: the drift tube chambers, the cathode strip chambers and the resistive plate chambers.

2.5.1   The Drift Tube Chambers

Muon detectors in the Barrel do not operate in particularly severe conditions, since the occupancy in this region is low and the magnetic field is well contained in the iron plates of the return yoke.

The chamber segmentation consists in five wheels along the z axis, each one divided into 12 azimuthal sectors. Within all wheels, chambers are arranged in four stations at different radii, named MB1, MB2, MB3 and MB4. Each station is made of 12 chambers, one per sector, except for MB4 where 14 chambers are built.

The basic detector element is a drift tube cell, shown in Fig.2.9. Cells have a size of 42×13 mm^2. A layer of cells is obtained by two parallel aluminium planes and by "I" shaped aluminium beams which define the boundary of the cells and serve as cathodes. I-beams are insulated from the planes by a 0.5 mm thick plastic profile. The anode is a 50 μm stainless steel wire placed in the centre of the cell. The distance of the track from the wire is measured by the drift time of the electrons produced by ionisation. To improve the time-distance linearity, additional field shaping is obtained with two positively biased insulated strips, glued on the planes in correspondence
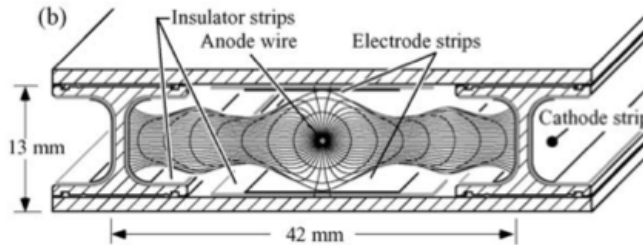
Figure 2.9: *Section of a drift tube cell.*

to the wire.

The gas is a 85%/15% mixture of Ar/CO_2, which provides good quenching properties and a saturated drift velocity, of about 5.4 cm/μs. The maximum drift time is therefore $\sim$ 390 ns, *i.e.* 15 bunch crossings. A single cell has an efficiency of about 99.8% and a resolution of $\sim$ 180 μm.

2.5.2 The Cathode Strip Chambers

Cathode Strip Chambers are used in the Endcap regions where the magnetic field is very intense and inhomogeneous and where the charged particle rate is high. CSCs are multiwire proportional chambers defined by two cathode planes, one segmented into strips, and an array of anode wires running across, in between (Fig.2.10). An avalanche developed on a wire induces a charge on several strips of the cathode plane, and interpolation between adjacent strips gives a very fine spatial resolution of 50 μm, which is used to measure the ϕ-coordinate. Simultaneously, the wire signals are read out, directly, and used to measure the radial coordinate with a coarse precision[2] of approximately 0.5 cm. The basic module of the CSC system is a chamber consisting of six layers.

Combining multiple layers also improves the timing resolution so that the correct bunch crossing can be assigned with over 99% efficiency. The cathode planes are formed by honeycomb panels with copper clad skins, while the 9.5 mm thick gas gaps are filled with a mixture of 30% Ar, 50% CO_2 and 20% CF_4. Chambers cover sectors of 10° or 20° and have a maximum dimension of 3.5 m to 1.5 m. The chambers are placed in four disks (stations ME1 to ME4) perpendicular to the beam axis. The inner rings of stations ME2 to ME4 consist of 18 chambers while all the other rings consist of 36 chambers.

---

[2]The closely spaced wires make the CSC a fast detector suitable for triggering
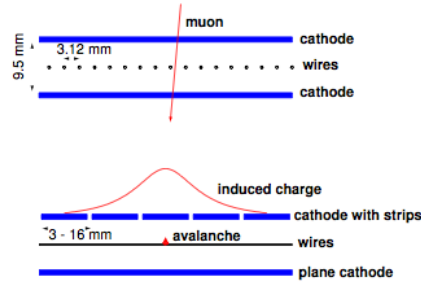
Figure 2.10: *Orthogonal section of one CSC chamber.*

2.5.3 The Resistive Plate Chambers

In order to have a fast dedicated muon trigger, CMS has been equipped with the resistive plate chambers (RPC). They give the time of an ionizing event in a much shorter time than the 25 ns between two consecutive LHC bunch crossings. Therefore, a fast device based on RPCs can identify unambiguously the relevant bunch crossing.

RPCs are parallel-plate detectors filled with gas having an excellent time resolution of approximately 1 ns, comparable to that of scintillators. A RPC consists of two parallel plates made of very high resistivity plastic material (bakelite), separated by a gas gap of a few millimeters (Fig.2.11). The plates are coated with graphite on the outside which forms the high voltage electrodes. The read-out is performed by means of aluminum strips separated from the graphite coating by an insulating PET (polyethylene terephthalate) film. The RPCs are operated with a gas mixture of 95% $C_2H_2F_4$ and 5% i-C_4H_{10}.

Their geometry within the detector depends on the position: six layers of RPCs are used in the Barrel. They are attached to either side of the DT chambers in the inner two stations and only to one side in the outer two stations. In the Endcaps, four layers of RPCs are attached to the four CSC disks, covering a range up to $|\eta| < 2.1$.

2.6 Forward Detectors

2.6.1 CASTOR

The CASTOR [20] (Centauro And Strange Object Research) detector is a calorimeter made of quartz-tungsten located 14.37 m from the CMS interaction point to extend the forward rapidity coverage to the region -6.6 $\leq \eta$
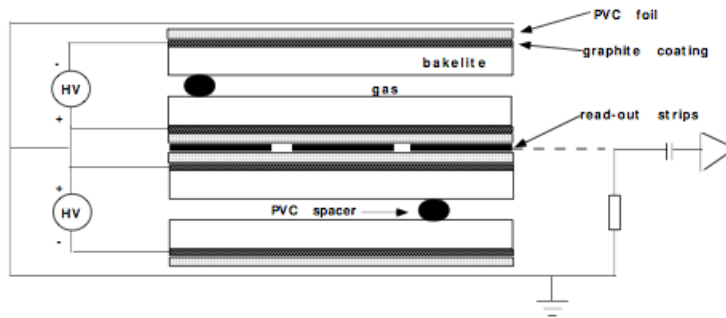
Figure 2.11: *Scheme of a double-gap Resistive Plate Chamber.*

$\leq$ -5.2. CASTOR presents a sandwich structure of tungsten (W) absorber
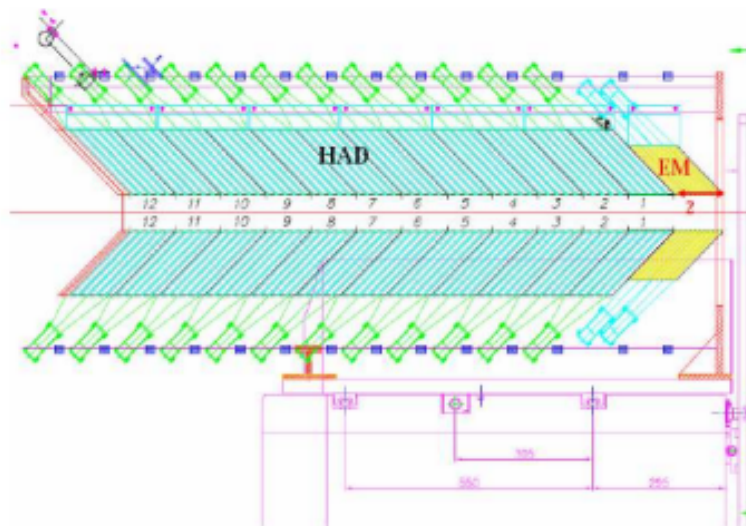
Figure 2.12: *The CASTOR detector.*

plates and quartz plates as active material. It has an octagonal cylindrical shape with an inner radius of 3.7 cm, an outer radius of 14 cm. The collection of the signal is based on the production of Cerenkov photons which are transmitted to photomultiplier tubes through aircore lightguides. The CASTOR calorimeter is divided in an electromagnetic section of 20.12 radiation lenght and an hadronic section of 9.5 radiation lenght. It has a 16-fold azimuthal segmentation in towers and a 14-fold longitudinal segmentation in sections, from which the two first are electromagnetic and the 12 remaining

hadronic. It has no segmentation in eta and consists therefore in a total of 224 channels.

The calorimeter and its readout are designed in such a way as to permit the observation of the cascade development of the impinging particles as they traverse the calorimeter. The typical total and electromagnetic energies in the CASTOR acceptance range (about 180 TeV and 50 TeV, respectively, from Pb-Pb simulations at 5.5 TeV) can be measured with a resolution better than ≈ 1 percent.

2.6.2   Zero Degree Calorimeter (ZDC)

For diffractive studies two zero degree calorimeters with pseudorapidity coverage of eta ≥ 8.3 are placed in the CMS forward region (Fig.2.13).

Each ZDC has two independent parts: the electromagnetic (EM) and
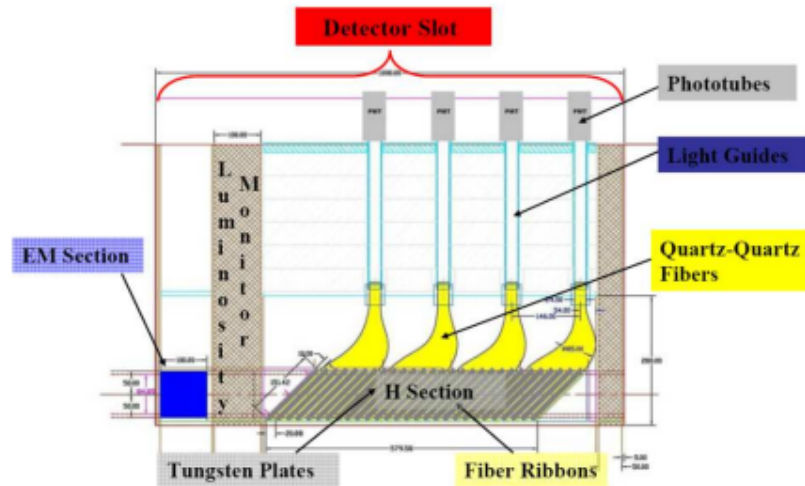
Figure 2.13: *The ZDC detector.*

hadronic (HAD) sections. Two identical ZDCs are located between the two LHC beam pipes at 140 m on each side of the CMS interaction point. During heavy ion running the combined (EM + HAD) calorimeter allows the reconstruction of the energy of 2.75 TeV spectator neutrons with a resolution of 10-15%. Sampling calorimeters using tungsten and quartz fibers have been chosen for the detection of the energy in the ZDCs with a design similar to HF and CASTOR.

2.7 Trigger And Data Acquisition

The high rate produced at LHC cannot be sustained by any storage system presently available. Given the typical size of a raw event (1 MB), only a rate of ~ 100 Hz can be stored for offline analysis, when the collisions rate is in fact 40 MHz. A huge reduction factor is then necessary: it is accomplished by the trigger and the data acquisition systems.

2.7.1 The Trigger System

The event rate is mainly composed of protons interactions with particles of low transverse momentum. A good triggering system should have a large rejection of the less interesting particles and maintain at the same time a high efficiency on the (potential) interesting events. This characteristic is achieved at CMS in two steps: a Level 1 Trigger (L1)[39] and a High Level Trigger (HTL)[40]. The rate reduction capability is designed to be a factor of 10^7 for the combined L1 and HLT.

2.7.1.1 The Level 1 Trigger (L1)

L1 consists of custom-designed, largely programmable electronics: it reduces the rate of selected events down to 100 kHz for the high luminosity running. The full data are stored in pipelines of processing elements, while waiting for the trigger decision. The maximum latency allowable is 3.2 μs: if the L1 accepts the event, the data are moved to be processed by the High Level Trigger. The high bunch crossing rate does not permit the full readout of the detector, mainly because of the slowness of the tracker algorithms: only the calorimetric and muons information are employed.

The Calorimeter Trigger (see Fig. 2.14) identifies the best four candidates of each of the following classes: electrons and photons, central jets, forward jets and *-jets identified from the shape of the deposited energy. The information of these objects is passed to the Global Trigger, together with the measured missing E_T.

The Muon trigger is performed separately for each muon detector. The information is then merged and the best four muon candidates are transferred to the Global Trigger. The Global Trigger takes the decision to reject an event or to accept the event for further evaluation by the HLT. The decision is based on algorithm calculations and on the readiness of the sub-detectors and the DAQ.

The L1 Trigger electronics is housed partly on the detectors, partly in the underground control room located at a distance of approximately 20 m from
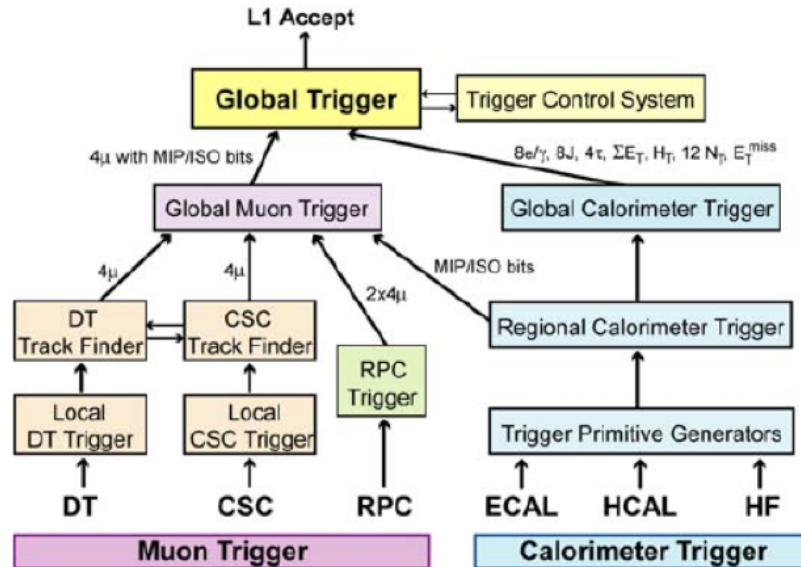
Figure 2.14: *Schematic representation of the CMS L1 trigger system.*

the experimental cavern.

2.7.1.2   High Level Trigger (HLT)

HLT is a software system (implemented in a filter farm of about one thousand commercial processors) which reduces the output rate down to around 100 Hz. The idea of the HLT trigger software is the regional reconstruction on demand: only objects in the useful regions are reconstructed and uninteresting events are rejected as soon as possible. The HLT has access to the high-resolution data in pipelined memories in the front-end electronics as well as the information from the silicon tracker: it can therefore perform complex calculations.

The L1 and HLT schema lead to the development of three "virtual trigger" levels: at the first level only the full information of the muon system and of the calorimeters is used, in the second level the information of the tracker pixels is added and in the third and final level the full event information is available.

2.7.2   The Data Acquisition (DAQ)

The CMS Data Acquisition (DAQ) [32] has the task to transport the data from about 650 data sources at the detector side, to the filter units for processing of complete events. Each data source provides event fragments of about 2kB. The central DAQ runs online software on about 3000 PC used for buffering and processing of event data.

The DAQ system of CMS is shown in Figure 2.15. The detector is read
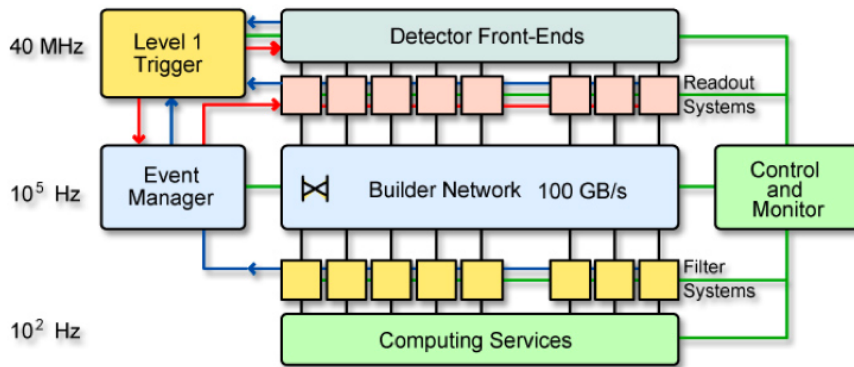
Figure 2.15: *The main components of the DAQ system of CMS.*

out through a builder network with a bisectional bandwidth of 100 GB/s by the so called Front-End Drivers (FED). The FEDs are located in the underground counting room $\sim$ 70 m from the detector. Complete events are fed to the event filter systems at a rate of maximal 100 kHz. The large rate to the filter systems stems from the design choice of CMS to build the full event already after the first level trigger instead of building partial events as in traditional multi level trigger systems. This requires the read-out, assembly and forwarding of the full event data at the nominal level one trigger rate.

The total rate of data produced by the online trigger system is $\sim$ 230 MB/s. These data need to be stored for further processing and analysis. Given the large data volumes involved and to the large size of the CMS collaboration, a fully distributed computing model is used for data reconstruction and analysis. The system is based upon Grid middleware, with the common Grid services at centres defined and managed through the Worldwide LHC Computing Grid (WLCG) project [22], a collaboration between LHC experiments, computing centres, and middleware providers.

Chapter 3

ECAL Detector

Electrons, positrons and photons dissipate their energy by showering in the electromagnetic calorimeter. Their signals are read-out by the ECAL electronics, which is physically divided in two blocks: the on-detector and the off-detector electronics. The first is responsible for the signal digitization and the trigger primitives production, and it will presented in section 3.1. The second is responsible for the finalization of the trigger information and for the readout and reduction of the full granularity data, and it is described in section 3.2.
Other relevant parameters related to the operational conditions of the detector, are read-out by the Detector Control Units (DCU) chips. This non-event parallel read-out chain is described in section 3.3.

3.1 ECAL On-Detector Electronics

The signal released by an interacting particle is firstly processed through the ECAL on-line readout chain, which is shown schematically in Fig. 3.1. The first element is the $PbWO_4$ crystal which converts energy into light. The light is converted into current by the photodetector. The relatively low light yield of the crystal necessitates a preamplifier stage before the photocurrent to voltage convertion stage. The readout requirements of ECAL imply the use of a multiple gain amplification stage to span the overall requested energy range, transmitting the signals only for the highest unsaturated stage. The electronics has been designed to read a complete trigger tower (5x5 crystals in ϕ x η). The trigger tower electronics consists of 5 Very Front End (VFE) boards, 1 Front End (FE) board, 1 Low Voltage Regulator card and a mother board.
The digitized data for each channel are then transmitted to the off-detector
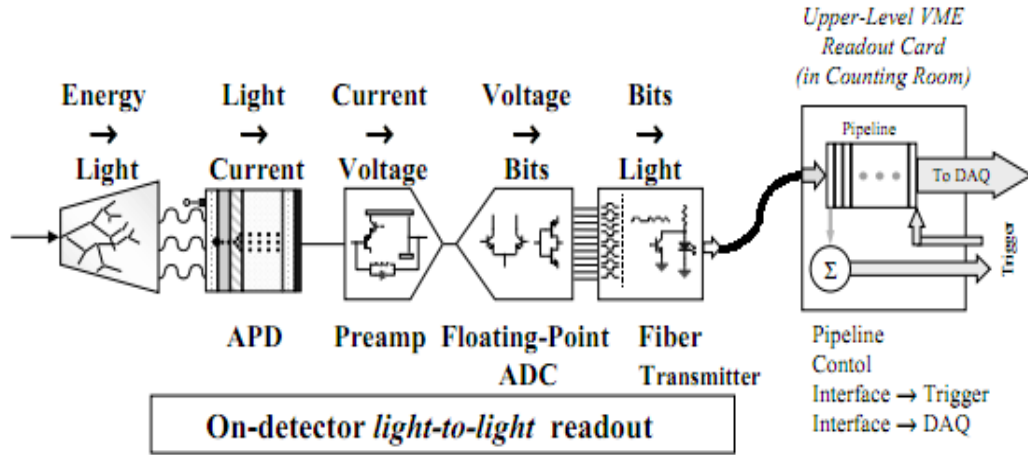
Figure 3.1: *The ECAL readout chain.*

electronics, via optical fibers.

3.1.1 Lead Tungstate Crystals

Both the Barrel and the Endcaps are made of $PbWO_4$ crystals. The main characteristics of this scintillating material are:

- the high density (8.28 g/cm^3)

- the short radiation length (0.89 cm) and small Moliere radius (2.2 cm), which gives a fine granularity and compact calorimeter

- the short scintillation decay time: about 80 % of the light is emitted in 25 ns.

The crystals have to resist to the very high radiation levels and particle fluxes throughout the duration of the experiment. Ionizing radiation produces absorption bands through the formation of colour centres due to oxygen vacancies and impurities in the lattice. The practical consequence is a wavelength-dependent loss of light transmission without changes to the scintillation mechanism, a damage which can be tracked and corrected for by monitoring the optical transparency with injected laser light.
The most important drawbacks of this type of crystals are:

- the relatively low light output (about 4.5 photoelectrons per MeV). A successive amplification stage is essential.

- the strong temperature dependence (2.1% at 18 °C) of the crystal pho-
  toemission. This implies stringent requirements on the stability of the
  temperature: 0.05 °C in the Barrel and 0.1 °C for the Endcaps. A
  water flow cooling system is used to stabilize the temperature of the
  crystals at the nominal operating value of 18°C.

The crystals emit blue-green scintillation light with a broad maximum at 420
nm [23]. Longitudinal optical transmission and radioluminescence spectra
are shown in Fig. 3.2. Pictures of Barrel and Endcap crystals with the
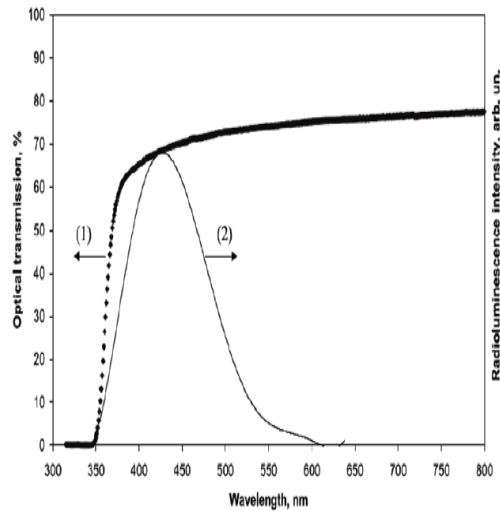
Figure 3.2: *Longitudinal optical transmission (1, left scale) and radiolumi-
nescence intensity (2,right scale) for production PbWO4 crystals.*

photodetectors attached are shown in Fig. 3.3.

3.1.2   Photodetectors

The photodetectors need to be fast, radiation tolerant and able to operate
in a high magnetic field. Moreover, because of the small light yield of the
crystals, they should provide electronic pre-amplification of the signals.
The configuration of the magnetic field and the expected level of radiation
led to different choices: avalanche photodiodes in the Barrel and vacuum
phototriodes in the Endcaps.
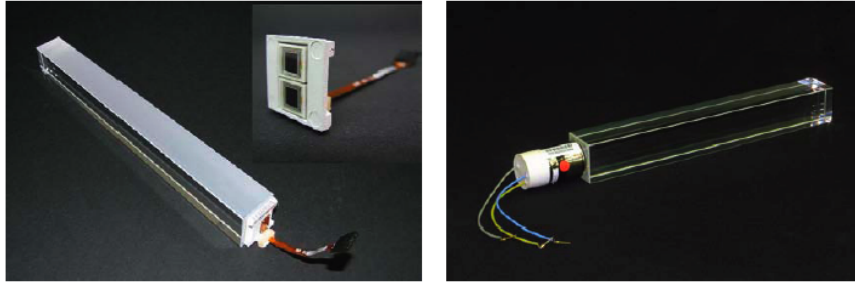
Figure 3.3: *PbWO4 crystals with photodetectors attached. Left panel: A Barrel crystal with the upper face depolished and the APD capsule. In the insert, a capsule with the two APDs. Right panel: An Endcap crystal and VPT.*

3.1.2.1   Avalanche Photodiodes

In the Barrel, the photodetectors are avalanche photodiodes specially designed for the calorimeter by Hamamatsu. They have been produced in reverse structure (type S8148), with the bulk n-type silicon behind the p-n junction. Each APD has an active area of 5x5 mm^2 and a pair is mounted on each crystal.

The APD (see Fig. 3.4) consists of a thin photocathode (p++), a p-n junction, a drift region and a highly doped cathode to collect the charge. Photons
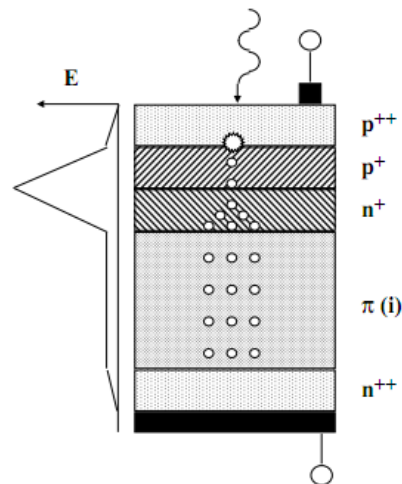
Figure 3.4: *Schematic view of the Avalanche Photodiodes (APD).*

convert in the p++ layer. Photoelectrons drift towards the abrupt p-n junction, where ionization starts and avalanche breakdown occurs. The avalanche breakdown results in electron multiplication.

The operational gain is 50: this value can be adjusted and varied by moving the nominal supply current.

The main properties of the APDs at gain 50 and 18 °C are listed in table 3.1. The sensitivity to the nuclear counter effect is given by the (effective) thick-

Sensitive area	Barrel 5 x 5 mm^2
Operating voltage	340 - 430 V
Breakdown voltage - operating voltage	45 ± 5 V
Quantum efficiency (430 nm)	$75 \pm 2\%$
Capacitance	80 ± 2 pF
Excess noise factor	2.1 ± 0.2
Effective thickness	6 ± 0.5 um
Series resistance	≤ 10 Ω
Voltage sensitivity of the gain (1/M x dM/dV)	3.1 ± 0.1 %/V
Temperature sensitivity of the gain (1/m x dM/dT)	$-2.4 \pm 0.2\%$/C
Rise time	≤ 2ns
Dark current	≤ 50 nA
Typical dark current	3 nA
Dark current after 2x10^{13} n/cm^2	5 uA

Table 3.1: *Properties of the APDs at gain 50 and 18 ∘C.*

ness of 6 mm, which turns into a signal from a minimum ionizing particle traversing an APD equivalent to about 100 MeV deposited in the $PbWO^4$. Each APD was required to be fully depleted and to pass through a screening procedure involving 5 kGy of ^{60}Co irradiation and 1 month of operation. The screening and testing aimed to ensure reliable operation for 10 years under high luminosity LHC conditions for over 99% of the APDs installed in the ECAL [24]. Based on tests with hadron irradiations [25] it is expected that the dark current will increase to about 5 uA, with no other significant property change.

The operating gain of 50 requires a voltage between 340 and 430 V. The gain stability directly affects the ECAL energy resolution, since the APD gain (M) has a high dependence on the bias voltage (dM/dV=3% at gain 50). Moreover, APD gain strongly depends on temperature variations (-2.3%/°C). In order not to affect the constant term of the resolution, a very stable power supply system is required: the stability of the voltage has to be of the order of

few tens of mV. A custom high voltage (HV) power supply system has been designed for the CMS ECAL in collaboration with the CAEN Company [26]. The APDs are kept termally stable by the same cooling system used for the crystals.

The APDs are sorted according to their operating voltage and paired. The pair is mounted in parallel in a capsule, which is then glued on the back of each crystal. The capsules are connected to the read-out electronics by Kapton flexible printed circuits of variable length.

3.1.2.2 Vacuum Phototriodes

In the Endcaps the vacuum phototriodes (VPTs) photodetectors (type PMT188 from National Research Institute Electron in St. Petersburg) are used (Fig. 3.5). They are photomultipliers with a single gain stage: these devices were developed specially for CMS [27] and have an anode of very fine copper mesh (10 mm pitch) allowing them to operate in the 3.8 T magnetic field.

Each VPT is 25 mm in diameter, with an active area of approximately 280 mm^2; one VPT is glued to the back of each crystal. The VPTs have a mean quantum efficiency of 22% at 430 nm, and a mean gain of 10.2 at zero field. When placed in a strong axial magnetic field, the response is slightly reduced
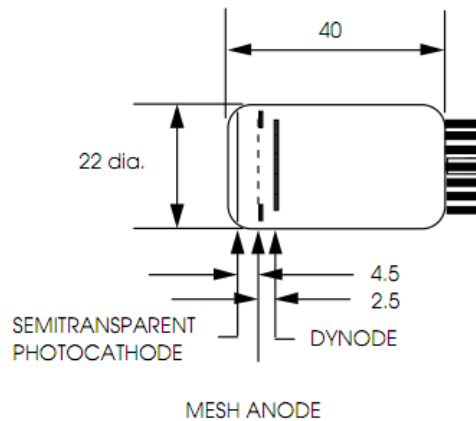
Figure 3.5: *Schematic view of the Vacuum Photo Triode (VPT).*

and there is a modest variation of response with the angle of the VPT axis with respect to the field.

All VPTs were tested to determine their response as a function of magnetic field up to 1.8 T. Each device was measured at a set of angles, spanning the range of angles covered by the Endcaps. The VPTs have been designed

to resist to the estimated doses and particle fluences for 10 years of LHC operation.

The VPTs are operated with the photocathode at ground potential and the dynode and anode biased at +600 V and +800 V respectively. The high voltage system is based on CAEN SY1527 standard control crates.

The anode sensitivity of a VPT may show a dependence on count rate (anode current) under certain conditions. For example, in the absence of a magnetic field, if the count rate falls to a few Hz, following a period of high rate operation, the anode sensitivity may rise suddenly and take several hours to return to the nominal value. The magnitude of the effect may vary from a few percent to a few tens of percent. In the presence of a strong magnetic field, the effect is strongly suppressed or absent. Nevertheless, it has been judged prudent to incorporate a light pulser system on the ECAL Endcaps. This delivers a constant background rate of at least 100 Hz of pulses of approximately 50 GeV equivalent energy to all VPTs.

The system is synchronized to pulse during a fraction of the 3 ms abort gaps that occur during every 89 ms cycle of the LHC circulating beams.

3.1.3   Motherboards And Low Voltage Regulator Card

The motherboard is a passive device located between the APDs and the VFE cards. It has been designed to:

- connect 25 photo-detectors to the VFE card using Kapton flexible printed circuit boards.

- house the 5 VFE and the LVR board.

- provide the high voltage (HV) to the photodetectors. In the Barrel the motherboard provides and filters the APD bias voltage. Two motherboards are connected to one CAEN HV supply channel located at a distance of about 120 m from the photodetectors. In the Endcaps the voltages for the VPTs are distributed and filtered by a separate HV filter card.

Each LVR card [29] distributes the output voltages of 2.5V to the FE card via the motherboards. The LVR card uses 11 radiation-hard low voltage regulators (LHC4913) developed by ST-microelectronics. The regulators have built in over-temperature protection, output current limitation and an inhibit input. Four LVR cards are connected by a passive low voltage distribution (LVD) block to one radiation and magnetic field tolerant Wiener low voltage power supply.

3.1.4 Very Front End Boards

The VFE boards perform the most important action in the ECAL readout. The signals are pre-amplified, shaped and then amplified again in parallel by a set of three amplifiers with nominal gains of 1, 6 and 12. To avoid the production of a very high precision radiation hard ADC, the approach has been to use multiple gain stages to reach the needed effective dynamic range (the full scale signal to cover is 1.5 TeV in the APDs, while for the VPTs is 3.1 TeV. The highest gain is required to have a least significant bit of approximately 35 MeV in the Barrel and 70 MeV in the Endcaps). A 12-bit ADC is thus sufficient, but a decision must be made as to which channel is in correct range. This functionality is reached using an ASIC chip called Multi Gain Pre-Amplifier (MGPA) [30], developed in 250 nm technology.

The shaping is done by a CR-RC network with a shaping time of ~ 40 ns. Each MGPA has a power consumption of 580 mW at 2.5 V. The output pulse non-linearity is less than 1%. The MGPA contains three programmable 8-bit DACs to adjust the baseline to the ADC inputs. An integrated test-pulse generator with an amplitude adjustable by means of an 8-bit DAC allows a test of the read-out electronics over the full dynamic range.

A schematic view of the signal read-out is given in Fig. 3.6. The three analog
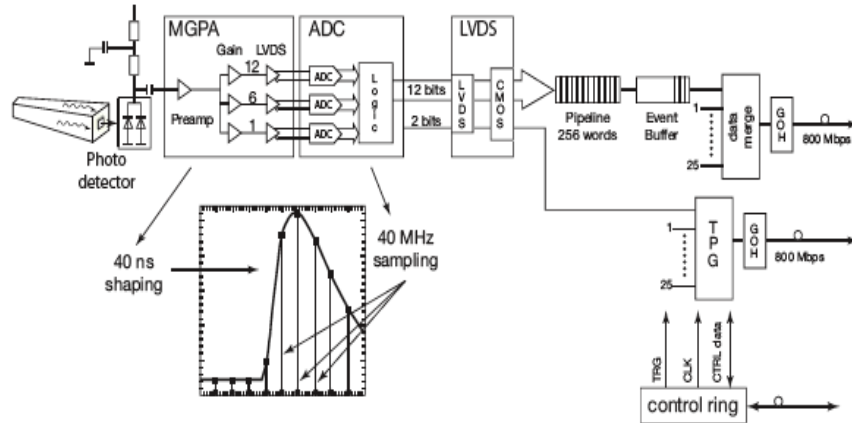
Figure 3.6: *Schematic view of the on-detector electronics.*

output signals of the MGPA are digitized in parallel by a multi-channel 12-bit ADC, the AD41240 [31], developed in the same technology. Its working frequency is 40 MHz. An integrated logic selects the highest non-saturated signal as output and reports the 12 bits of the corresponding ADC together with two bits coding the gain (1=1X, 2=6X and 3=12X).

The noise obtained with the VFE cards installed into supermodules is typically 1.1, 0.75 and 0.6 ADC counts for gains 12, 6 and 1 respectively. This corresponds to ~ 40 MeV for gain 12.

3.1.5 Front End Boards and Optical Links

The signals from the 5 VFEs are collected on the Front End (FE) cards. Each FE card contains 7 FENIX ASICSs, used to:

1. buffer digitized data until a level-1 trigger is received

2. transmit the data to the ECAL off detector electronics, for read-out

3. sum the samples from a group of 5 channels (strip) at 40 MHz and then sum the data from the 5 strips for transmission to the calorimeter trigger. In the Barrel region the FE performs also the calculation of the trigger primitives (TP). The TP consists of roughly 3000 words, representing the transverse energy deposited in each ECAL trigger tower and a compactness bit, which characterizes the lateral extension of the electromagnetic shower.

Digitized data are sent to the DAQ system and the TP to the Level-1 trigger using two opto-hybrids with radiation-tolerant laser diodes for electrical to optical conversion, and GOL ASIC for parallel to serial conversion.
Clock signals are distributed to a group of 8 FE cards using two independent electrical token rings. These rings communicate optically to the off-detector electronics.

3.2   ECAL Off-Detector Electronics

The ECAL data are used both in the CMS Level 1 Trigger, which receives coarse information on energy deposit (trigger primitives), and by the High Level Trigger (HLT, see Chapter 2) system, which uses full granularity data. The trigger primitives are sent every 25 ns to the Regional Calorimeter Trigger (RCT). The signal is then propagated up to the Global Trigger (GT), the top entity of the Level-1 hierarchy. The level-1 accept (L1A) signal is issued whenever an interesting event is found by the GT system within 3 μs.

The ECAL off-detector electronics read-out and trigger architecture [41],[42] is schematically illustrated in Fig. 3.7. The off-detector electronics receives signals from the Timing,Trigger and Control (TTC) system, namely the clock, the L1A signals plus the so-called B-Go commands, used for synchronisation and acquisition of special triggers. The electronics is organized in 54 identical units each comprising three types of VME boards:
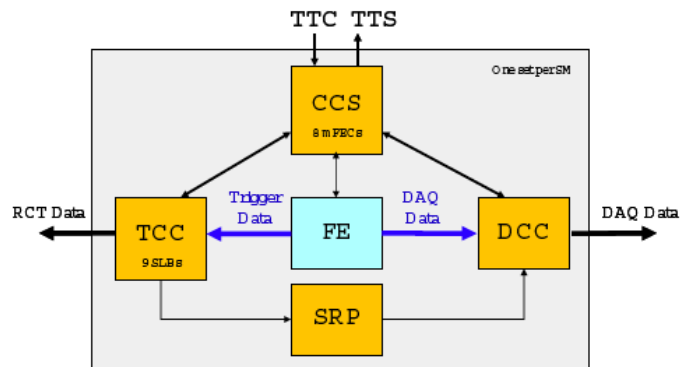
Figure 3.7: *Schematic view of ECAL off-detector electronics.*

- **the Clock and Control System (CCS)**.
  The CCS board distributes the system clock, the L1A signal and broadcast commands, configures the FE electronics and provides an interface to the trigger throttling system.

- **the Data Concentrator Card (DCC)[45] [46]**.
  The DCC is responsible for collecting crystal data from up to 68 FE boards. Two extra FE links are dedicated to the read-out of laser monitoring data (PN diodes). The DCC also collects trigger data from the TCC modules. The DCC performs also data concentration using

the flags computed by the selective read-out processor (SRP). A data suppression factor near 20 can be attained.

- **the Trigger Concentrator Card (TCC)[43]**.
  The TCC main functionality include the completion of the trigger primitive generation and their transmission, the classification of each trigger tower and its transmission to the SRP at each L1A signal, and the storage of the trigger primitives during the Level-1 latency for subsequent reading by the DCC.
  Moreover, the TCC board performs the calculation of the TP in the Endcaps region.

The selective readout algorithm is based on the classification of the detector in high and low interest regions performed by the SRP. The system is composed by a single 6U-VME crate with twelve identical algorithm boards (AB). The AB computes the selective readout flags in different calorimeter partitions. The flags are composed by 3 bits, indicating the suppression level that must be applied to the associated readout units.

3.3 Detector Control Units (DCU)

In parallel to the crystal data stream of the ECAL readout channels, other relevant parameters such as crystal and electronic temperatures, APD leakage currents and supply voltages, are read-out by several chips located on the on-detector electronics. Those chips are radiation hard ASIC produced in CMOS technology (0.25 μm IBM CMOS) called "Detector Control Units (DCU)". In this section the description of their main characteristics and performaces are presented.

3.3.1 DCU Description

A DCU chip can be divided schematically in 6 main blocks (see Fig. 3.8):

- a serial slave interface based on the standard I2C protocol

- an analogue multiplexer

- a 20 μA constant current source

- a 12-bit ADC

- one on-chip temperature sensor

- a band-gap reference
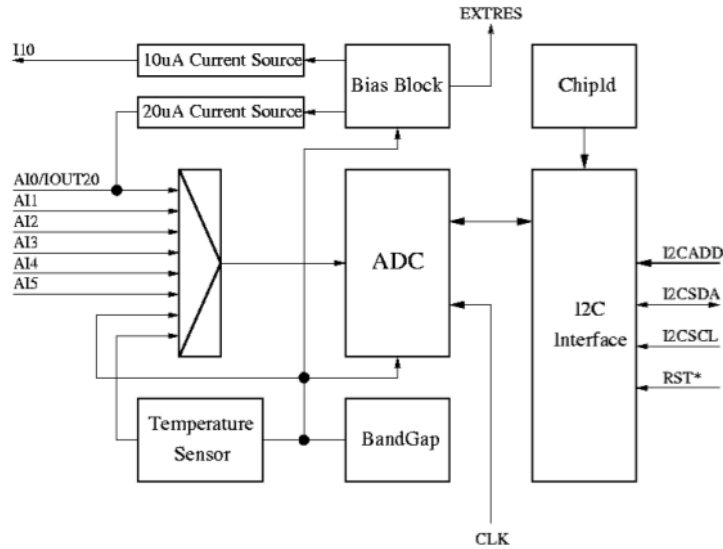
Figure 3.8: *Detector Control Unit Schema.*

The DCU chip only accepts voltages as input. It provides a temperature estimation driving the 20 μA current source through an external thermistor and comparing its voltage drop with the band-gap voltage reference (reaching a sensitivity of 0.012 °C). Good voltage measurements are achievable connecting directly the voltage source to the DCU chip input (sensitivity $\sim$mV), while currents are evaluated by measuring the voltage drop over a fixed well known resistor (sensitivity 340 nA).

Every VFE board houses a DCU chip which reads the temperature of the crystals, the leakage currents of the APDs and its own internal temperature. Three DCU chips are also located on the LVRB, measuring temperatures and supply voltages of the FE and VFE cards.

The DCU chips are read-out via the control token rings driven by CCS cards.

3.3.2   DCU Software architecture

The online software uses a common framework written in C++ (*XDAQ* [52]) and runs on Scientific Linux [53]. The online processes are embedded in the hierarchical control structure of Run Control and Monitor System (*RCMS* [54]) which is the collection of software components responsible for controlling and monitoring the CMS experiment during data taking. The online

software which controls the DCU system is made by two independent parts, one taking care of handling the DCU raw data (CCS Supervisor/Front end daemons) and one which converts them into physics quantities (*DCUConverter*).

The action flow is as follow (Fig. 3.9):

1. the DCU data are read-out by either the front end status daemons or by the CCS Supervisor, application which takes care of configuring the front end boards for data taking. Both can access the DCU internal registers and read the data through the control token rings[1].

2. the DCUConverter checks periodically and independently the presence of new raw data and takes care of converting them into physics quantities. It accesses the Conditions Database (CondDB) to retrieve the calibration constants for the crystal temperature values and the APD leakage currents.

3. the converted data are sent to the Detector Control System (DCS), to the CondDB and stored locally as text files.

An xml file allows the configuration of the DCUConverter main parameters. The scheduler working frequency is settable by the user. A flag called "test mode" allows the user to operate without the presence of the real data. The interaction with the DCS and the database can be bypassed by setting an appropriate boolean flag.

The dispacting of the data to the official CMS database and to the DCS system is then described in the next two subsections.

3.3.3 DCU To DCS Interface

The ECAL Detector Control System [55] provides several functionality: monitoring of the detector environmental parameters and of the operational conditions of the detector electronics, as well as the monitoring and control of the configuration and running parameters of all ECAL subsystems (HV, LV, Cooling and Laser monitoring systems). The ECAL DCS also provides early detection of abnormal conditions, executes predefined control actions and triggers hard-wired interlocks to protect the detector and its electronics from severe damage.

The DCU system is interfaced with the DCS system and sends periodically

---

[1]At this moment, the DCU data are read every ten minutes if the calorimeter is not included in global run, otherwise every start and stop of the run. In the future it is foreseen the data read-out every 10 minutes regardless the status of the calorimeter
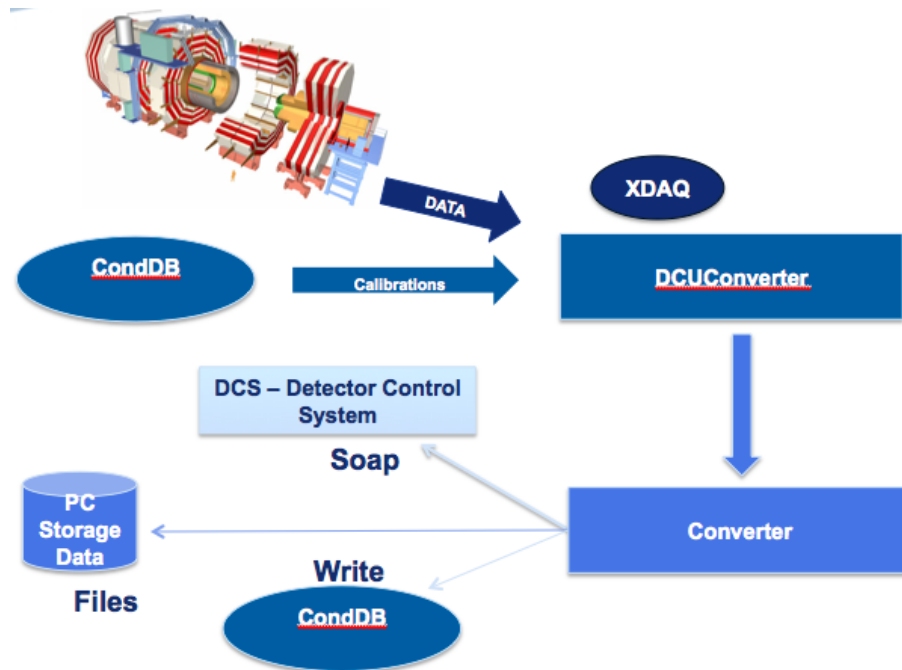
Figure 3.9: *The "DCUConverter" class and its functioning.*

all the safety-related measurements, converted in form of PVSS[2] *datapoint*
to be displayed and monitored: crystals and electronics temperatures, low
voltages electronics supply. The total amount of data is quite huge: $\sim$75000
measurements have to be handled and transferred at every read-out process.
In the final working schema, it is foreseen to send updates (only data chang-
ing more than 2% of their nominal value) every 10 minutes and the whole
ECAL every 30 minutes. Fig. 3.10 shows the summary view of the Endcap
status in the graphical interface of the DCU-DCS project.

3.3.4   DCU To CondDB Interface

The online CMS conditions database is the repository where the detector
status during runtime is going to be stored. Given the complexity of the
CMS detector, each subdetector have developed its own database schema
and services for their control and monitoring. The online database is located
close to the CMS experimental area. The fraction of data relevant for the
physics event is automatically copied into the offline database (located on

---

[2]It is a commercial SCADA (Supervisory Control And Data Acquisition)
application[56], running on Windows machines
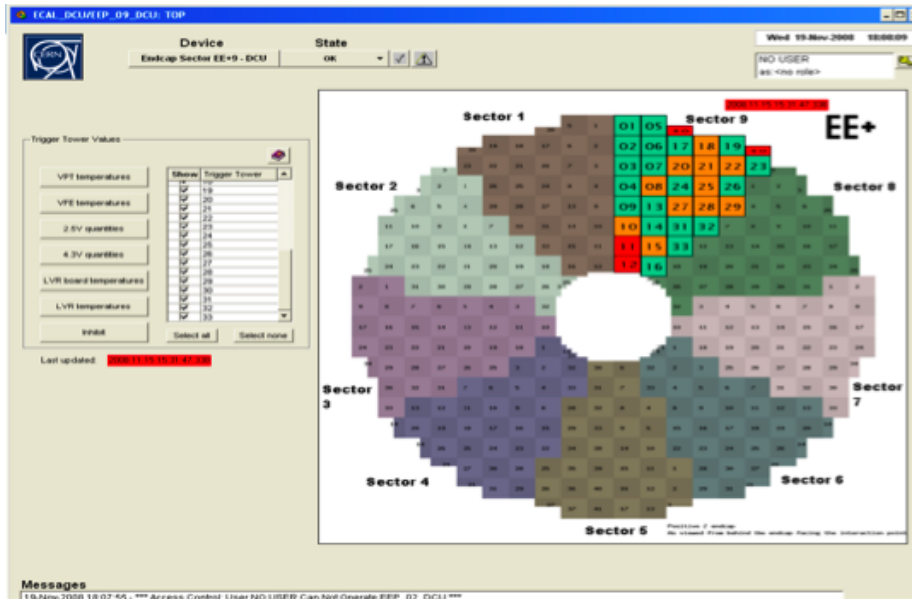
Figure 3.10: *Summary view of the Endcap in the DCU project interface.*

the CERN IT division) using a dedicated link.

The Ecal CondDB stores all the "non event data", which can be grouped into four different categories:

- Quality Control Data: data collected during construction phase which provides the information about the element position (associations between crystals,photodetectors,...) and photodetector optimal biases.

- Detector Conditions: the status of the detector. Temperature, humidity, status of the high voltage and low voltage distribution are included in this type of data.

- Global Run Conditions: DAQ and trigger configuration used for each CMS run.

- Local Runs Results: information on ECAL control and monitoring.

The quality of the physics data is ensured only if the detector working conditions are optimal.

Starting from the 2010, DCU data are sent to the database every four hours. In the final implementation, it is foreseen to send updates containing only the measurements which have changed by $\geq 2\%$ of their nominal value, plus the full record every N hours (where N can be tuned and optimized for every

category). In particular the crystal temperatures have to be properly tracked to allow good monitoring of the detector thermal stability since they are necessary to correct offline, if needed, the crystal light yield and the APD gain. DCU measurements stored in the database can be visualized using the Web Based Monitor (WBM) of CMS[3]. An example of 2D map taken from WBM is shown in Fig. 3.11.
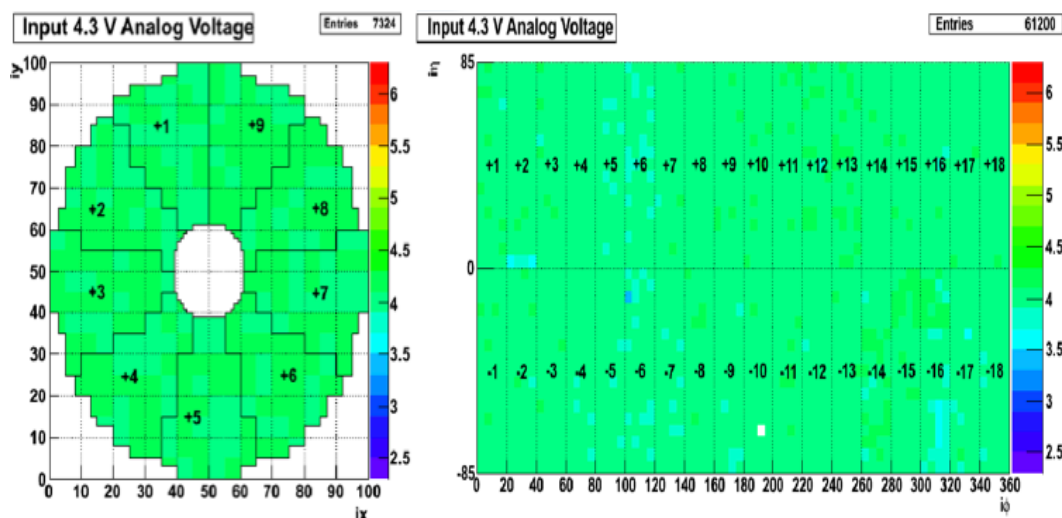
Figure 3.11: *2D map of the distribution of the low voltage values (4.3V analogic) both in the Barrel and in the Endcap, as seen from the Web Based Monitor.*

---

[3]WBM has been designed and implemented un order to easily browse the online data content. It makes use of the Apache Tomcat application server[37] that executes Java servlets and renders the HTML pages.

Chapter 4

ECAL Thermal Stability

In this section we will present how the temperature stability of the ECAL detector has been evaluated and monitored. The DCU system, already introduced in the previous chapter, has been extensively used for this purpose, together with another independent monitoring system (PTM) which is described in section 4.2.

The first study has been performed during the 2008 CMS commissioning phase, and then regularly repeated to measure the detector temperature stability during all the data taking periods.

Section 4.3 presents the analysis procedure and the temperature stability measured in 2008. Section 4.4 reports the results obtained for the 2009 and 2010 stable data taking periods.

4.1 General Overview

The potential to discover a neutral Higgs boson in the low mass region by measuring its decay into two photons has been used as a benchmark for the calorimeter design. A photon energy resolution of 0.5% above 100 GeV has been set as a requirement for the ECAL performance. As already introduced in the previous chapter, this places stringent requirements on the stability of the temperature, since the light yield of the lead tungstate crystals changes approximately by -2%/°C, and the Barrel APD gain by -2.3%/°C. The VPT response in the Endcaps can be assumed to be insensitive to temperature variations. For those reasons a thermal stability of 0.05 °C is required in the Barrel region, and of 0.1 °C in the Endcaps.

A water flow cooling system [59] is used to stabilize the temperature of the crystals at the nominal operating value of 18 °C and to remove the heat generated by the front end cards (73 W per 5x5 crystal matrix). The detector

temperature is monitored by two independent systems: the Precision Temperature Monitoring (PTM) and the Detector Control Unit (DCU) systems, described in details in the next section.

4.2 PTM And DCU Temperature Monitoring Systems

The ECAL Precision Temperature Monitoring system is made by a set of accurate temperature sensors (NTC 470 Ω ECPOS thermistors). In the Barrel there are 10 PTM sensors per supermodule: one on the incoming and one on the outgoing cooling line, plus four pairs positioned one per module. The paired sensors are placed one on the aluminium grid which is in front of the electronic compartment, and one on the thermal screen which decouples the crystals from the silicon tracker. In the Endcaps, every Dee is equipped with four pairs of sensors, located as for the Barrel on the aluminium backplate hosting the crystals and on the thermal screen, plus 16 sensors positioned in each of the incoming and outgoing pipes of the 8 coolant lines.

The PTM sensors are read out every minute. For these studies, only a subset of the available data, corresponding to one reading out of ten, has been used: a ten minutes sampling is well suited to follow the temperature fluctuation of the detector, given its large thermal capacity. All the sensors located inside the detector have been pre-calibrated by the manufacturer and tested in the laboratory: the measurement's accuracy of temperature changes is guaranteed to be better than 0.01 °C, while the measurement tolerance is ≤ 0.1 °C. The uncalibrated sensors, placed on the cooling pipes, provide measurements with a tolerance of about 0.2 °C.

An independent temperature measurement is provided by the DCU system reading a set of thermistors located near the back of the crystals.

In the Barrel there is one thermistor for each 5x2 crystal matrix, for a total of 170 thermistors per supermodule. The thermistor is located inside the capsule hosting the two APDs which read the light from the same crystal. In the Endcaps, there is one thermistor every supercrystal (a matrix of 5×5 crystals), soldered on the backplate and connected by a 50 cm long coaxial cable to the DCU chip line.

The thermistors are read by the DCU ASIC. This chip drives an internal (known) current across the thermistor and the temperature is inferred from the digitalized voltage drop by using the Steinhart-Hart (SH) [58] model for the resistance temperature dependence.

Every thermistor have been characterized prior the installation, in order to

find and record its best SH parameters. Only two parameters are enough for
the SH fit.

Despite this precise calibration of the thermistors, the read-out circuits differ
from the one used in calibration setup and vary from chip to chip, therefore
the measurements are inaccurate. The temperatures reported by two adja-
cent thermistors can be offset by as much as a few degrees centigrade. The
procedure used to compute the offsets of the reading circuits is described in
subsection 4.2.2.

4.2.1 Precision Of DCU Measurements

The ECAL cooling system should provide a temperature stability within 0.05
°C in the Barrel and 0.1 °C in the Endcaps. We verified whether the DCU
system has sensitivity to monitor the temperature evolution at the requested
level. For this purpose, 13 runs on three selected supermodules have been
taken in a very short time (few minutes) to guarantee with a very good
approximation, a stable temperature (given the long thermal time constant
of the system, which is of the order of ten hours). We can therefore assume the
actual temperature variations during these runs to be zero. Figure 4.1 shows
the RMS distribution of the 13 measurements taken by the 510 thermistors
involved.
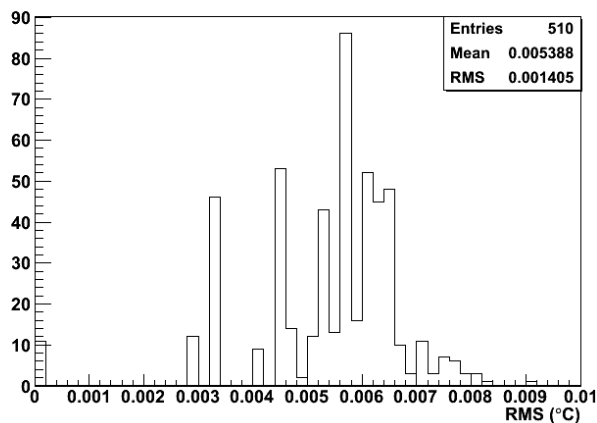
Figure 4.1: *Distribution of the temperature RMS of the thermistors located
in three selected supermodules of the Barrel: every thermistor has been read-
out 13 times in few minutes.*

The average fluctuation is the DCU reading precision and is about (0.005 $\pm$

0.001) °C, one order of magnitude smaller than the allowed range of variation. The RMS values equal to zero come from very stable thermistors varying below the LSB threshold. This fluctuation is the convolution between the sensitivity of the ADC converter, which is equal to $LSB/\sqrt{12} = 0.012/\sqrt{12}$ = 0.0035 °C, and the intrinsic precision of the thermistors. Given the limited number of measurements, the statistical precision of the average fluctuation is not negligible. We can estimate the intrinsic precision to be approximately of the order of ~ 0.004 °C.

It is safe to conclude that the DCU system is well suited to measure the thermal evolution of the detector.

4.2.2   DCU Temperature Measurement Calibration

The procedure to calibrate the DCU readings makes use of the PTM temperature measurements as reference. To overcome the non-simultaneity of the two independent systems, only PTM data points with a time difference between the thermistor and PTM sensors of less than 30 minutes are considered.

The calibration is performed for each thermistor separately. First, the DCU longest thermally stable period, within a given dataset, is found. A stable period is defined as a period where the RMS of all temperatures measured by the thermistor is less than 0.05 °C. For each point in time during the stable period, the difference between the temperatures reported by the thermistor and the nearest PTM measure is computed. The average value of this distribution is taken as the thermistor calibration constant to be added to the temperature reported by the thermistor, while the distribution RMS is taken as the calibration intrinsic precision.

The temperature measurements taken in a thermally stable and controlled area (cosmics stand 2005) have been used to calibrate the DCU readings of the Barrel region [63]. The Very Front End cards in the Barrel, which house the DCU chips, have been dismounted and remounted during 2007, nominally in the original position, with the exception of few VFEs which were broken and therefore replaced. While studying the thermal stability of the Barrel during its commissioning phase (2008), it was discovered that a number of DCU channels were not properly calibrated. In order to recover those channels, the entire detector has been re-calibrated in the experimental cavern (with the same technique used in [63]) using a set of 50 runs taken within one hour.

The new set of calibration constants obtained is less precise than the ones calculated at the cosmic stand, being the experimental cavern thermally more difficult to control. The new constants have been used only for the following

cases:

- Documented replaced VFEs: broken VFEs which have been replaced during the assembly campaign (2007) at building 867 ($\sim$ 2% of the total number of channels).

- Isolated bad points: we define an isolated bad point as a channel in which the temperature is different by ≥ 0.3 °C (corresponding to ~ 16 σ) from its 8 surrounding thermistors. The distance between thermistors is of the order of few centimeters, therefore any eventual source of heat should be detected in more than one channel ($\sim 0.3\%$).

- Displaced VFEs: pairs of VFEs which have been mounted by mistake in the wrong position ($\sim 0.5\%$).

- Supermodule EB-16: for unclear reasons, the calibration constants for EB-16 are no longer applicable.

After the Endcap installation and commissioning (beginning 2009), also the Endcap thermistors have been calibrated in the experimental cavern using the same procedure. Unfortunately no data coming from a thermally controlled test area are available. A special series of 50 runs taken in a very short time (if compared to the detector thermal constant value) have been used to calibrate the Endcaps.

4.3 Temperature Stability: Analysis And Results Of The 2008 Period

Starting from late 2008, the ECAL cooling system has been kept under stable conditions during the data taking periods. The thermal stability and spacial uniformity have been continuously measured for both the supermodules (Barrel) and the Dees (Endcaps).
In the following sections the analysis performed during the *Cosmic Rays at Four Tesla* (CRAFT08) period, September 2008 is presented. About 50 DCU runs and a skimmed PTM dataset (one readout every 10 minutes) have been used [64].

4.3.1   Barrel

The Barrel temperature spacial uniformity at a given time can be shown by representing the Barrel in azimuthal and polar coordinates, as in Fig. 4.2.

Each box of the grid corresponds to one of the 36 supermodules, 18 in the plus side (positive ieta) and 18 in the minus side (negative ieta). The numbering of the supermodules goes from left (EB±1) to right (EB±18). Every thermistor measurement has been represented as a colored square: only channels within 17.8-18.5 degrees are shown. White spots indicate measurements out of this range (percentage ~1‰ in Fig. 4.2) while black spots represent missing measurements (0.6%, mostly recoverable). EB-7 was excluded from the read-out because of low voltage problems. Fig. 4.2 shows the very good temperature homogeneity among the supermodules and that the crystals located at the edges of the calorimeter are warmer.
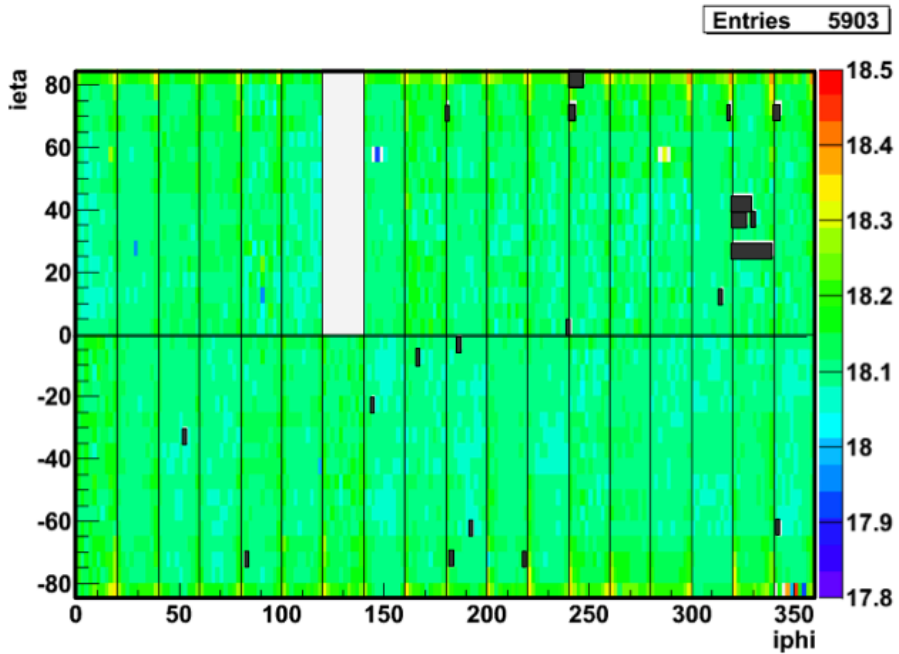
Figure 4.2: *Unrolled view of the Barrel instantaneous temperatures, measured on Oct 14th 2008, where EB-7 was excluded from the read-out because of low voltage problems.*

The temperature distribution measured with DCU sensors during CRAFT is presented in Fig. 4.3. The average temperature is (18.12 ± 0.04) °C, which demonstrate a very good spacial uniformity and stability in time. The distribution also presents a high temperature tail due to the thermistors located on the outer borders of the calorimeter (filled distribution in Fig. 4.3): their average temperature is 0.09 °C higher than the rest of the Barrel. The design

of the ECAL cooling system implies a lack of thermal screen on the outer crystals. This effect, together with the vicinity to the HV cables, might explain the higher average temperature.

The mean temperature does not correspond to the nominal operational temperature of the cooling system (18.00 °C), which has been used during the 2006 calibration test beam campaign. This implies that the calorimeter energy scale, computed during the test beam, must be corrected to take into account the $\sim 0.5\%$ decrease of the detector response.
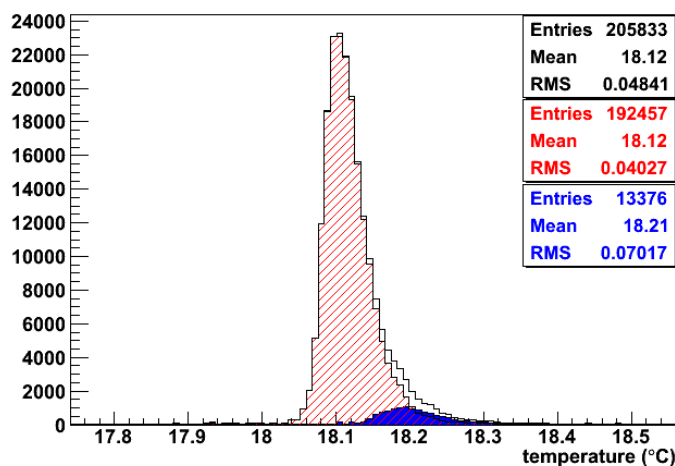
Figure 4.3: *Barrel temperatures distribution during CRAFT, measured at the APD capsules level (DCU): the total distribution of the thermistors (empty white plot), the thermistors located in the outer borders (filled area) and the inner (cross-hatched area) are presented.*

The Barrel temperature distribution during CRAFT as measured by the PTM system is shown in Fig. 4.4, where the mean of the four internal PTM sensors is computed for every supermodule. The average temperature is (18.10 ± 0.02) °C, in very good agreement with the DCU measurement. As the majority of the DCU readings has been calibrated in a different environment (at the cosmics stand), this result also demonstrates the correctness of the calibration procedure.

The time evolution of the Barrel cooling system and, consequently, of the supermodules temperature can be very well followed with the PTM sensors continuous sampling. Figure 4.5 shows the mean temperature over time, as seen by four representative PTM sensors. Each data point is the average of
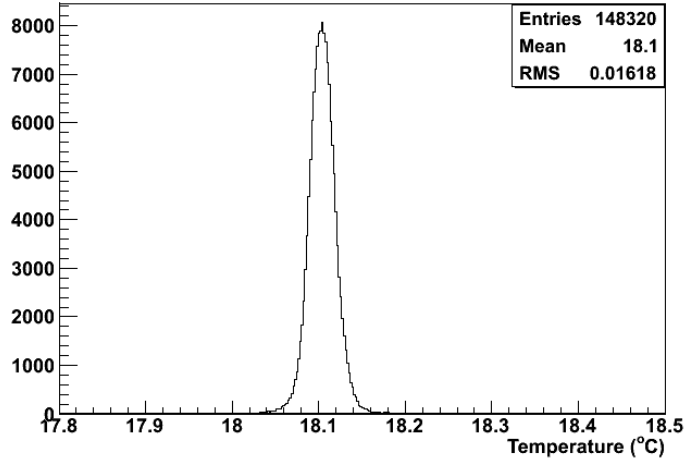
Figure 4.4: *Barrel temperatures distribution during CRAFT, as measured by the PTM system.*

about 45 readings, and the error bar represents the uncertainty on this mean value. Two PTMs are located in the module 1 ($0 \leq |\eta| \leq 0.44$) and one in module 4 ($1.13 \leq |\eta| \leq 1.48$), while the fourth is located on the cooling water line.

To better quantify the temperature stability (removing calibration and inhomogeneity effects), the RMS of every thermistor measurements has been calculated and plotted in Fig. 4.6 (DCU thermistors on the left end plot and PTM sensors on the right).

The stability measured by the DCU thermistors is (0.009 ± 0.003) °C, while the PTM sensors measure an higher value of (0.021 ± 0.010) °C, due to their slightly worse precision (0.01 °C). These measurements demonstrate the temperature stability to be within the specifications.

4.3.2   Endcap

A typical map (in linear coordinates transverse to the beam axis) showing the instantaneous temperature of every Endcap DCU thermistors is shown in Fig. 4.7. Black spots are thermistors with no read-out data, 22 channels in total. Six of them are broken thermistors, while the remaining part is recoverable. This distribution is not representative since both the thermistors and DCU chips calibrations were not yet available and applied.

The Endcap temperature time evolution is presented in Fig. 4.8, where three
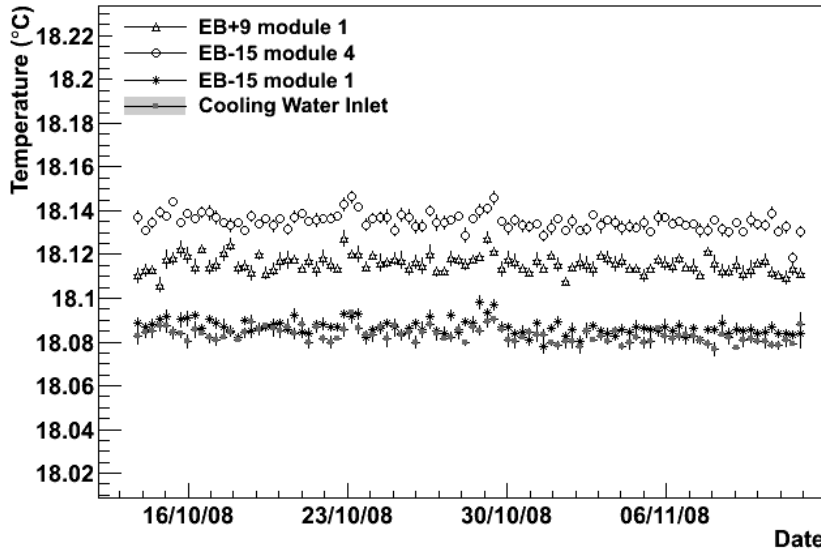
Figure 4.5: *Stability of the Barrel temperature during CRAFT as seen by four sensors located in different Barrel supermodules and by one located on a cooling pipe (water-in).*
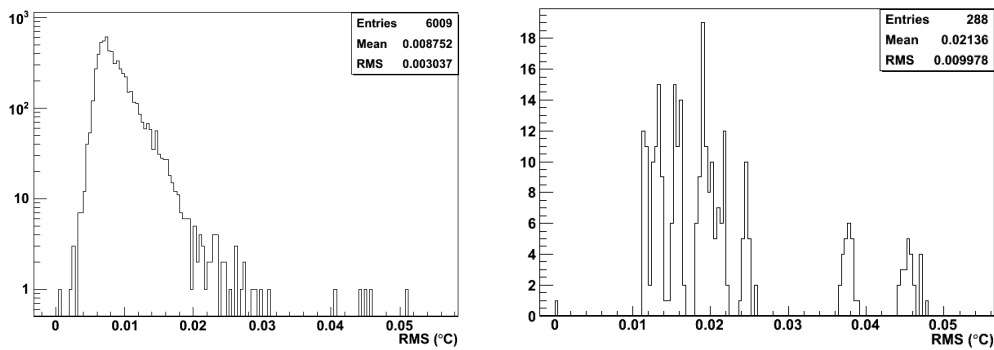
Figure 4.6: *Distribution of temperature RMS for each of the ECAL Barrel DCU thermistors (on the left) and PTM sensors (on the right), during CRAFT.*
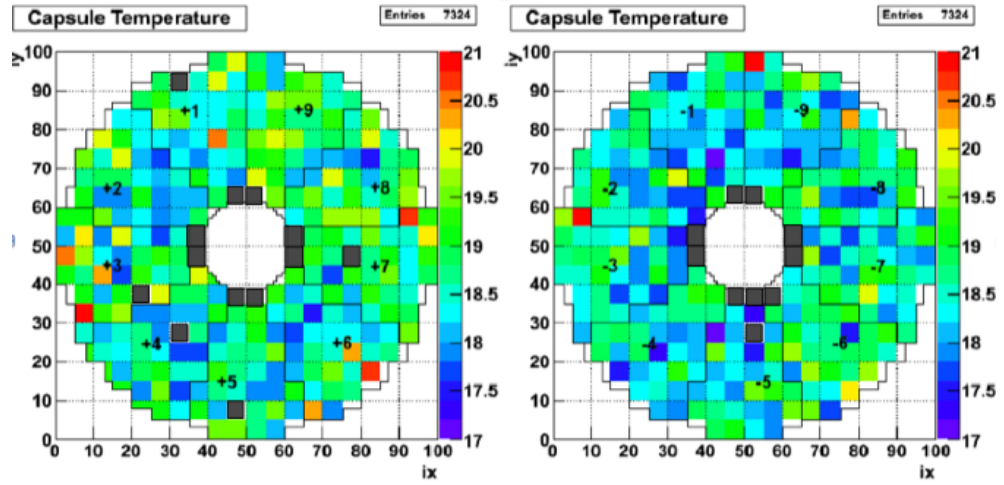
Figure 4.7: *Map of the Endcaps instantaneous temperatures, taken on 14th of October 2008. The DCU readings on the Endcaps are not calibrated.*

PTM sensors (on Dee1, Dee2 and Dee3) are shown together with an additional sensor on the cooling pipe. It clearly show a turn-on period at the start of CRAFT, followed by a long period of relatively flat readings and then a turn-off at the very end (during the turn-off, the source of heat coming from FE cards is removed, and therefore the temperature decreases).
The temperature distribution has been evaluated from the arithmetical mean of the PTM sensors located on the backplate and on the thermal screen (Fig. 4.9). The larger RMS observed in the second Endcap is due to the higher noise level affecting the Dee3 PTM sensors reading, as clearly visible in Fig. 4.8. The mean temperature is (18.58±0.04) °C for Dee1 and Dee2 (EE-) and (18.55±0.06) °C for Dee3 and Dee4 (EE+). The two peak structure is due to the overlap of Dee3 and Dee4 distribution in EE- and Dee1 and Dee2 in the EE+.

The RMS distribution for all the Endcap temperature sensors is presented in Fig. 4.10 (DCU thermistors on the left end plot and PTM sensors on the right end plot). The DCU mean fluctuation is (0.046±0.042) °C, while the PTM is (0.068±0.048) °C. Those values are worse than the ones in the Barrel.
In order to evaluate the performance under stable conditions, the RMS distribution has been computed using only data acquired whenever the detector was in thermal equilibrium (16 October-10 November). For the DCU system, the average stability becomes (0.017 ± 0.011) °C: this value is only two times
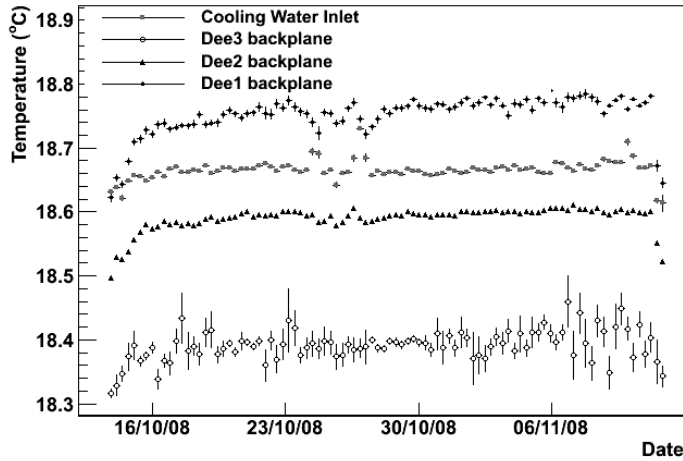
Figure 4.8: *Endcaps temperature time evolution during CRAFT, as seen by three representative PTM sensors located on Dee1, Dee2 and Dee3, and one located on a cooling pipe.*
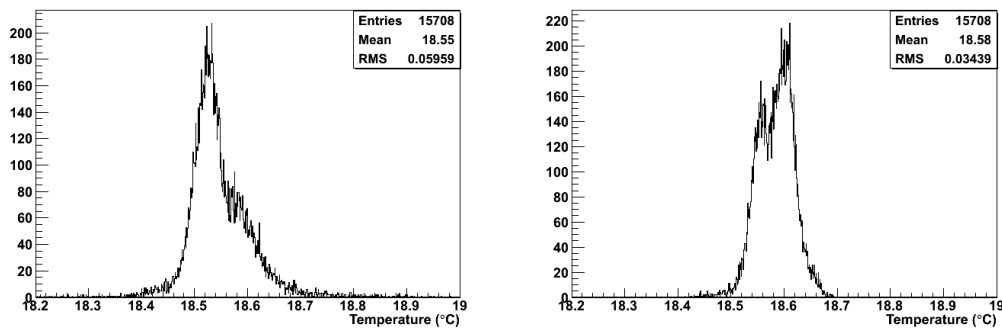
Figure 4.9: *Endcaps temperatures distribution during CRAFT, measured at the PTM sensors level for EE- (left end plot) and EE+ (right end plot).*

worse than the Barrel. For the PTM system, it becomes (0.061 ± 0.048) °C, roughly tree time worse.

Another study has been carried out to investigate the level of intrinsic
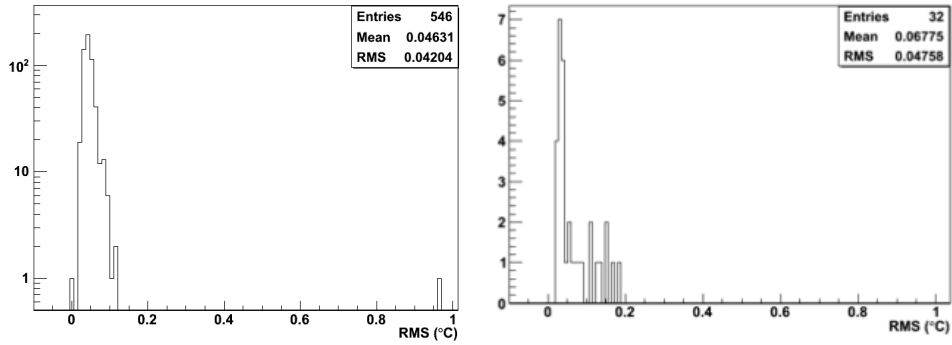
Figure 4.10: *Distribution of temperatures RMS for each of the ECAL End-cap DCU thermistors (left) and PTM sensors (right) during CRAFT.*

readout noise in the temperature measurements. The relative variation of neighboring thermistors (RMS distribution of thermistor pairs temperature difference) has been evaluated for the Barrel and the Endcaps, and it has been found with a larger spread in the latter.

To conclude, even if all of the fluctuations in the Endcap thermistors are attributed to real temperature variations, the temperature stability still lies within the specifications.

4.4 ECAL Thermal Stability During 2009 And 2010

The analysis of the detector thermal stability during 2009 and 2010 data taking is presented in this section. In particular, the following periods have been analyzed:

1. The Cosmic Rays At Four Tesla (CRAFT09) (August - September 2009)

2. 2009 beam period (Beam09) (November - December 2009)

3. 2010 beam period I (Beam10 PI) (30 March- 6 June 2010)

4. 2010 beam period II (Beam10 PII) (1 July - 14 December 2010)

The analysis has been done using the following information:

1. PTM data. The samples have been skimmed considering only measurements every 10 minutes. The PTMs have been particularly useful to detect and eliminate the turn-on and turn-off periods, in which the detector was not thermally stable.

2. DCU data. We have recorded DCU data every 10 minutes whenever the calorimeter was not included in a global run, otherwise at every start and stop of the run. The typical amount of measurements collected in a period is about 1000.

Starting from the second half of 2010 the analysis have been performed using only data acquired when the "Physics Declared" bit was *on*. This bit is set only when both the LHC beams are stable and all the CMS sub-detectors are operative and ready for the data taking.

4.4.1 2009 Period

During this year, the calibration of the Endcap thermistors have been performed. They have been calibrated using the same technique explained in the section 4.2.2. The final result can be appreciated looking at the instantaneous temperature map in Fig. 4.11.
The detector thermal constants have been calculated, using both the DCU and the PTM sensors. During the turn-on periods, the rise time τ has been evaluated according to this formula:

$$T(t) = (T_{stable} - T_{env})(1 - e^{-\frac{t-t_0}{\tau}}) \qquad (4.1)$$
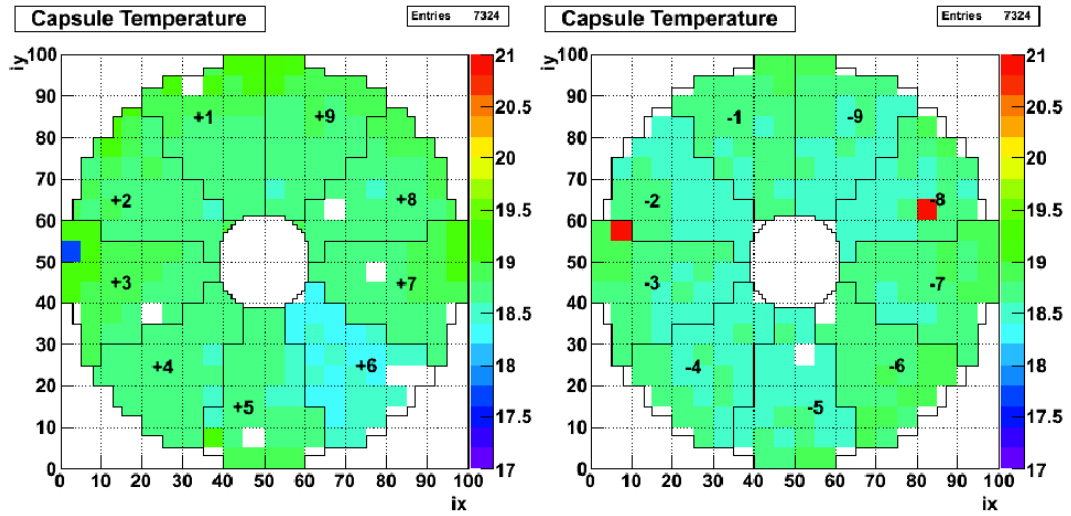
Figure 4.11: *Map of the Endcaps instantaneous temperatures, taken on 2009. The DCU readings on the Endcaps are now calibrated.*

with T_{env} being the environmental temperature and T_{stable} the operational temperature. The τ value has been calculated to be approximately 2 hours for the Barrel and 6 hours for the Endcaps (Fig. 4.12).
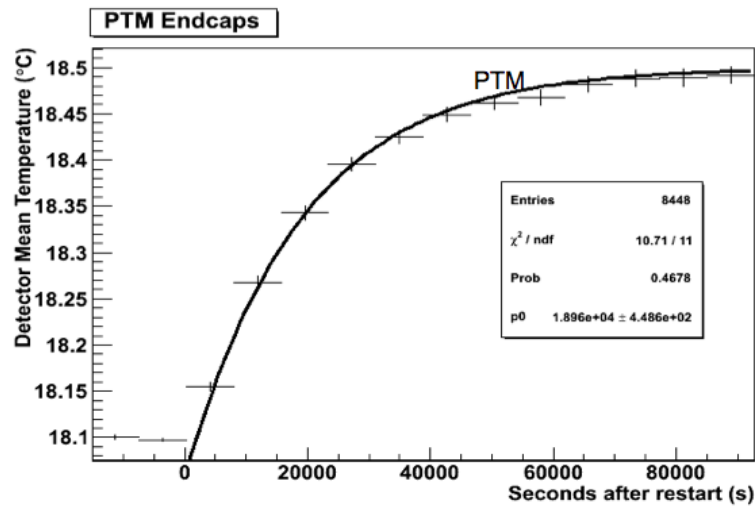
Figure 4.12: *Measurement of the Endcap thermal constant using 2009 PTM data.*

The PTM data have been used to select the time ranges in which the detector was thermally stable. The PTM mean temperature history during the Beam09 is presented in Fig. 4.13 (Barrel) and Fig. 4.14 (Endcaps). The
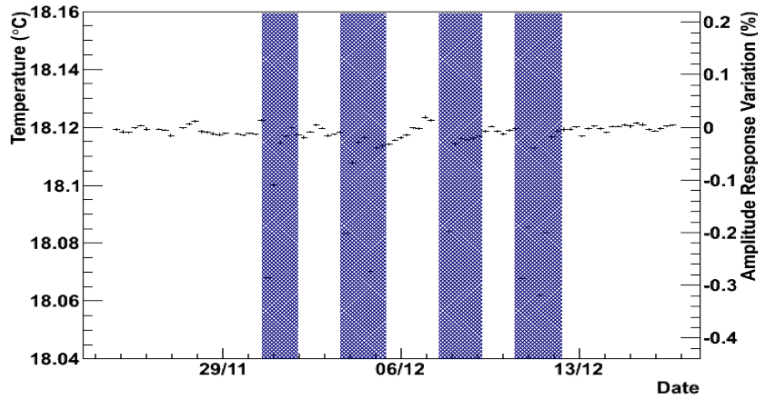
Figure 4.13: *The Barrel PTM mean temperature history during Beam09 period.*
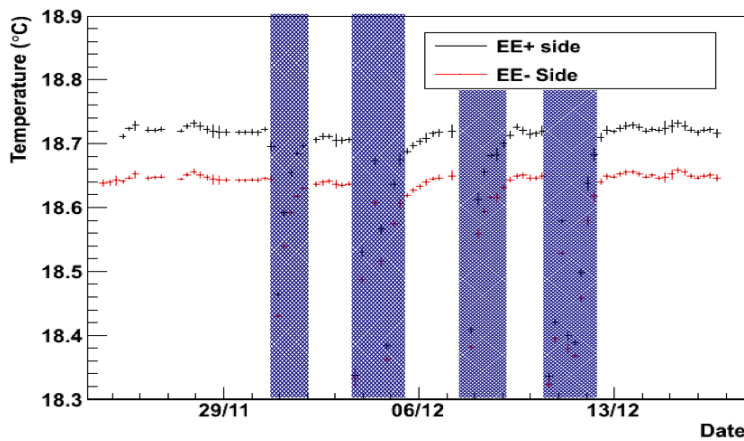
Figure 4.14: *The Endcaps PTM mean temperature history during Beam09 period.*

shadowed areas in two plots represent the periods in which the detector, after being switched on, was not yet thermalized, due to the high values of the Barrel and Endcaps thermal constants. A total of four periods have been excluded from the analysis. The same measurement has been repeated for

CRAFT09: three termically unstable periods have been identified and discarded.

The Barrel and Endcap temperature stability is then estimated with the DCU thermistor temperature RMS: RMS distributions during the Beam09 are shown in Fig. 4.15 (Endcaps and Barrel together), while the CRAFT09 distributions are presented in Fig. 4.16 (Barrel) and Fig. 4.17 (Endcap). The results are also summarized in Table 4.1 recalling the CRAFT08 period for comparison.
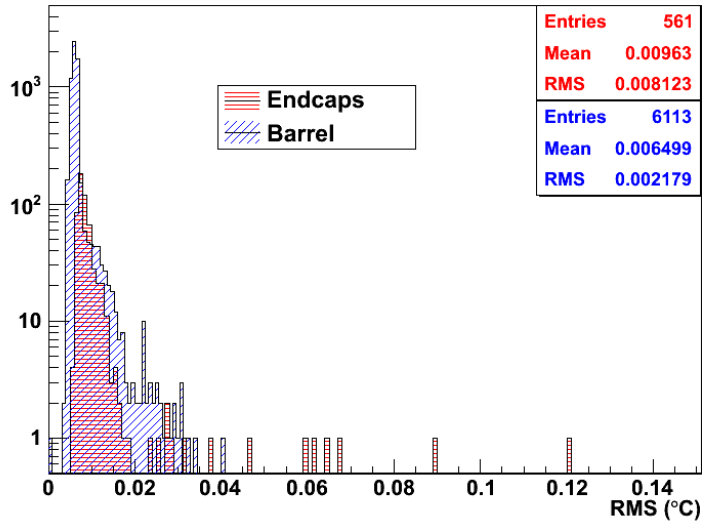
Figure 4.15: *Distribution of the temperature RMS for each of the Endcap and Barrel DCU thermistors. Data have been collected during the Beam09 period.*

Periods	Barrel RMS	Barrel Error	Endcap RMS	Endcap Error
Beam09	0.006	0.002	0.010	0.008
Craft09	0.006	0.003	0.011	0.007
Craft08	0.008	0.002	0.017	0.011

Table 4.1: *Comparison of the mean temperature RMS distributions for Beam09, CRAFT09 and CRAFT08 (Barrel and Endcaps).*
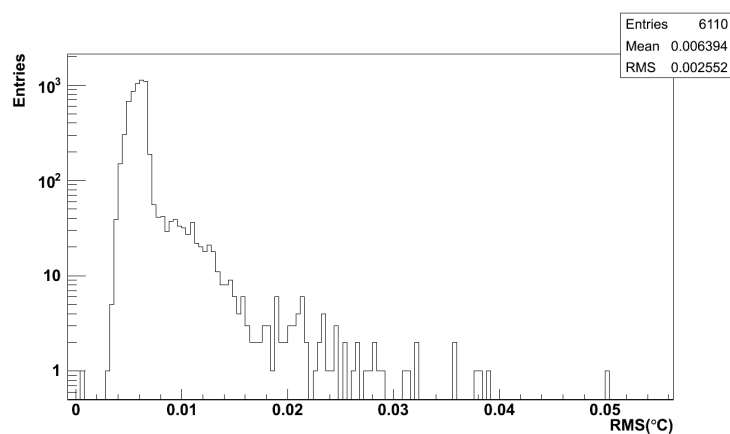
Figure 4.16: *Distribution of the temperature RMS for each of the Barrel DCU thermistors. Data have been collected during the CRAFT09 period.*
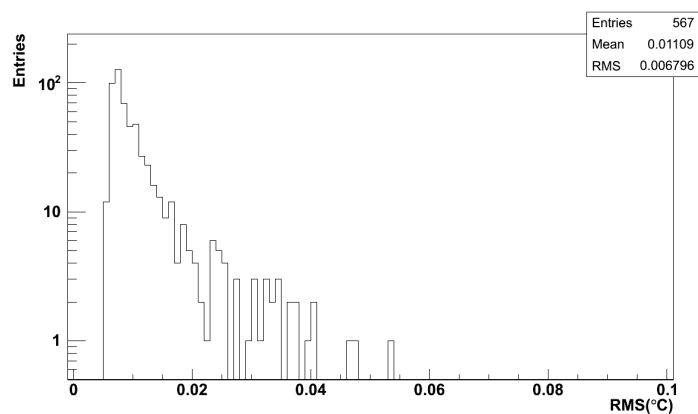
Figure 4.17: *Distribution of the temperature RMS for each of the Endcap DCU thermistors. Data have been collected during the CRAFT09 period.*

The thermal stability has been proven to be within the specifications. The RMS values for both the Endcaps and the Barrel are better than the one measured during the 2008 period.

4.4.2   2010 Period

During the first part of 2010, PTM data were used to select periods of thermal stability, while the Physics Declared Bit has been used during the second half of 2010. We have studied the spacial distribution of the DCU thermistors temperature RMS values in the Barrel, as presented in Fig. 4.18.
The outer crystals (ieta≥80), which were known to be warmer than the oth-
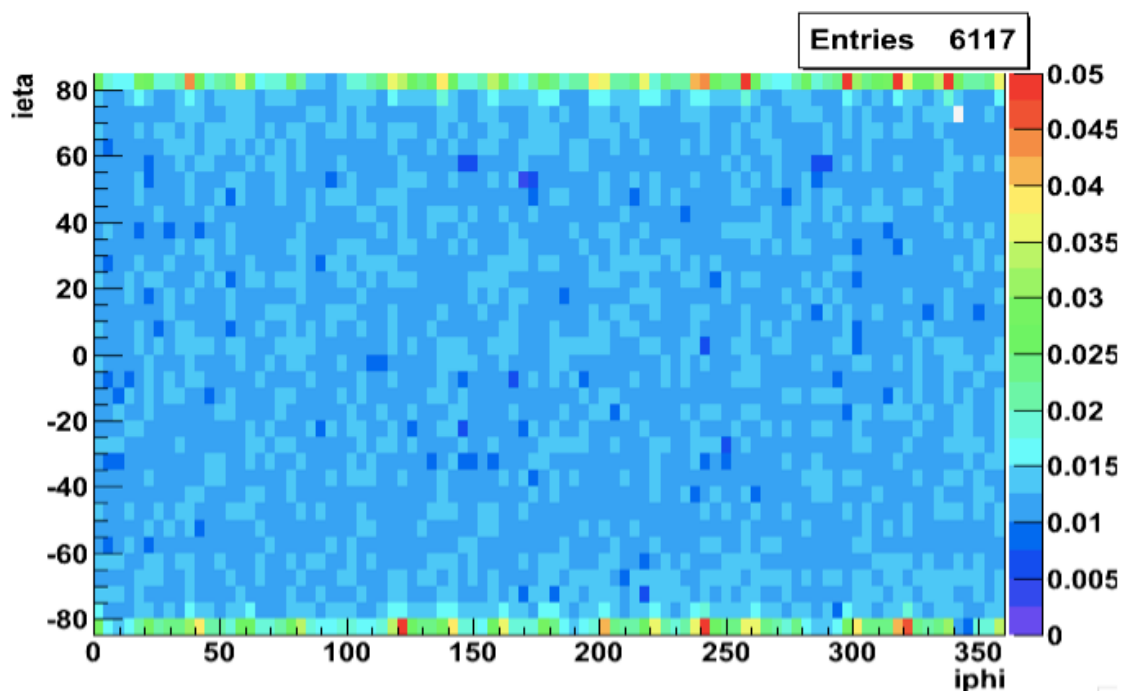
Figure 4.18: *Spatial distribution of the DCU thermistors temperature RMS values in the Barrel.*

ers, have also higher RMS value, as it is clearly shown in the picture. This effect could be explained with the lack of thermal screen in the Barrel edges, which prevents this region to be perfectly insulated.

In the following section the Beam10 PI and PII results are presented. The PTM and DCU mean temperature history during the Beam10 PI are presented in Fig. 4.19 (Barrel) and Fig. 4.20 (Endcaps). The shadowed areas of the two plots represent the periods excluded in the analysis.
The DCU Barrel and Endcaps thermistor RMS distributions have been plotted in Fig. 4.21 and Fig. 4.22 respectively for Beam10 PI and PII. The results are summarized in table 4.2.
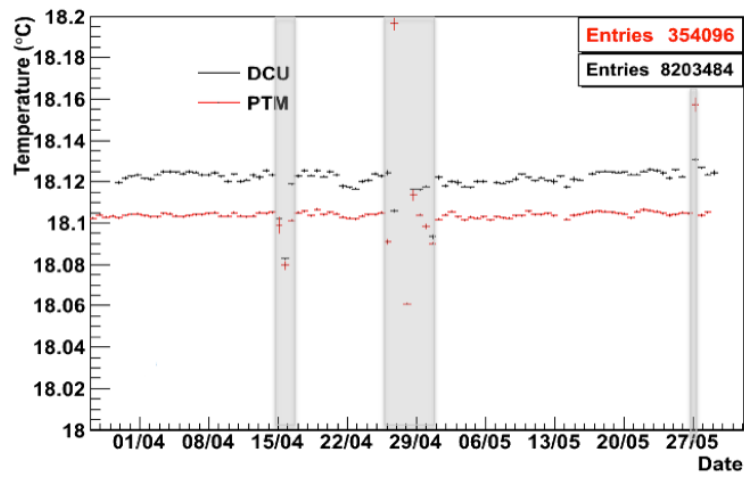
Figure 4.19: *The Barrel PTM and DCU mean temperature history during Beam10 PI period.*
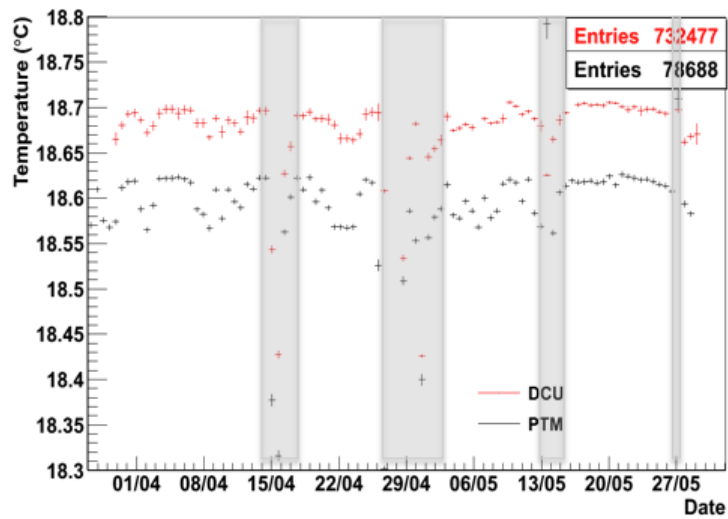
Figure 4.20: *The Endcaps PTM and DCU mean temperature history during Beam10 PI period.*

Periods	Barrel RMS	Barrel Error	Endcap RMS	Endcap Error
Beam10 PI	0.008	0.003	0.015	0.009
Beam10 PII	0.007	0.001	0.009	0.005

Table 4.2: *Comparison of the mean temperature RMS distributions for Beam10 PI and PII (Barrel and Endcaps).*
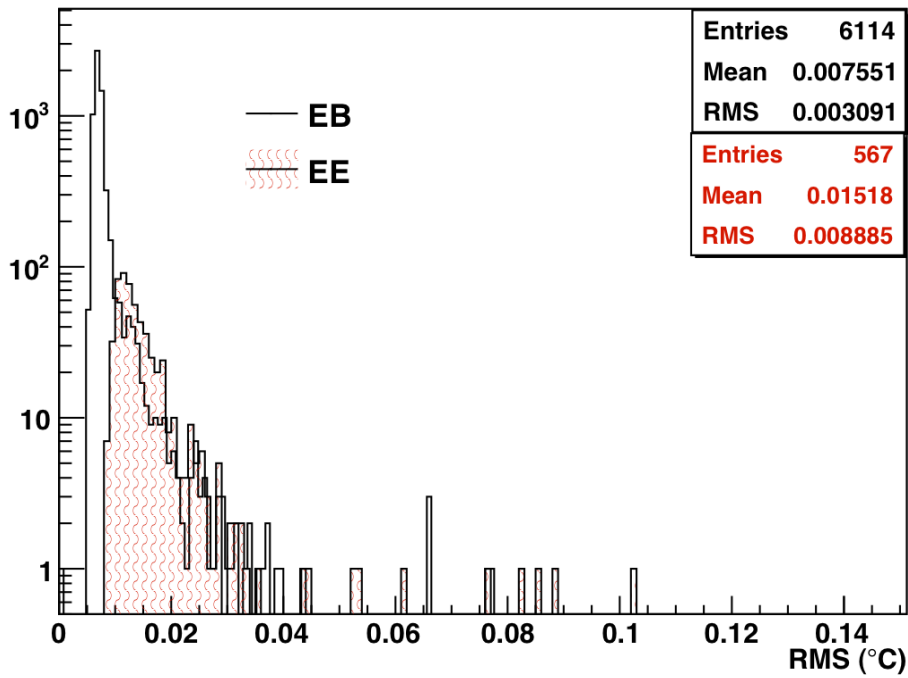
Figure 4.21: *Distribution of the temperature RMS for each of the Barrel DCU thermistors (empty area) and the Endcaps DCU thermistors (filled area). Data have been collected during the 2010 Beam Period I.*
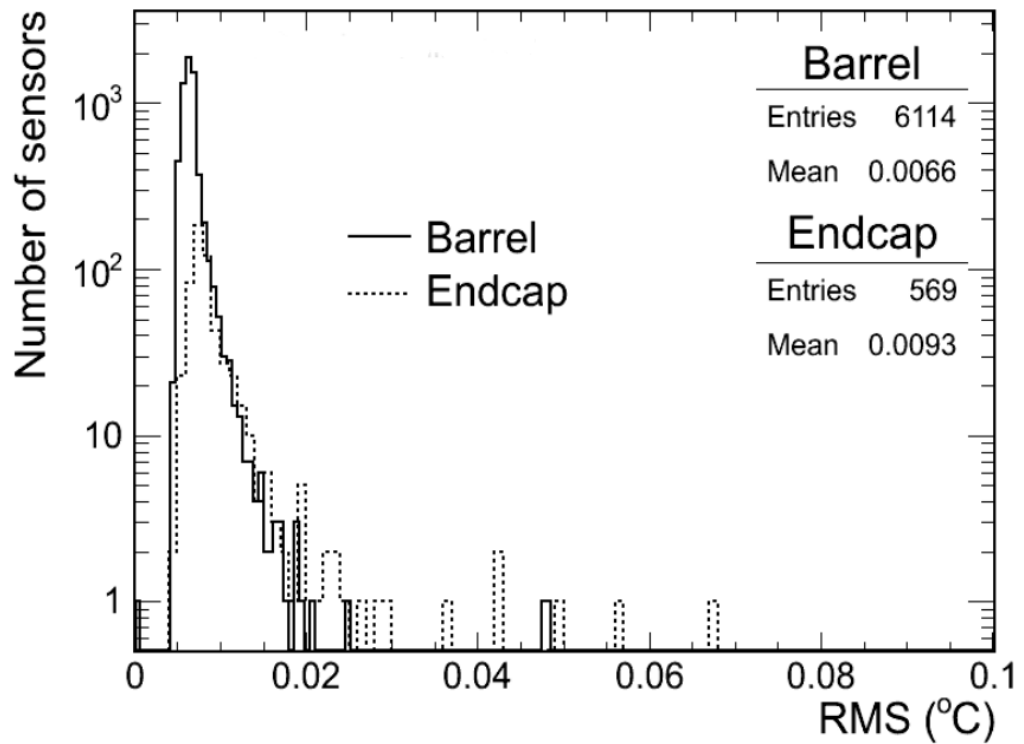
Figure 4.22: *Distribution of the temperature RMS for each of the Barrel DCU thermistors (continuous line) and the Endcaps DCU thermistors (dashed line). Data have been collected during the 2010 Beam Period II (selecting events having "Physics Declared" bit on).*

The analysis demonstrates that also in 2010 the thermal stability is well within the specifications.

4.5 Conclusions

The DCU and PTM measurements taken during the period 2008-2010 show that the CMS-ECAL detector meets the temperature stability target. The mean value of the RMS distribution for every temperature sensors has been considered as the estimator of the detector thermal stability.
In the Barrel, all readings are within the specification of 0.05 °C. In the Endcaps, the system shows worse performance: these higher values can be partly ascribed to a loss in precision due to electronic noise affecting the readings. Nevertheless the Endcap thermal stability lies within the specification of 0.1 °C.

Chapter 5

Diffractive Z Cross Section Studies

During the 2010 run, proton-proton (pp) collisions at 7 TeV were recorded by the CMS experiment. A fraction of the pp scattering is due to diffractive events. This chapter presents a study for the measurement of the diffractive Z$\to e^+e^-$ and Z$\to \mu^+\mu^-$ cross sections.
A comparison between data and Monte Carlo simulation with different generators is also shown.

5.1   Data and Monte Carlo Samples

The data samples processed for the analysis amount to $\sim 36\ pb^{-1}$ and are divided in two periods, called "RunA" and "RunB". The RunA was taken between April-August 2010, at a lower instantaneous luminosity per bunch crossing (BX) ($0.1 - 0.2\ \cdot 10^{30}cm^{-2}s^{-1}$). The RunB was recorded at higher instantaneous luminosity (up to $0.7\ \cdot 10^{30}cm^{-2}s^{-1}$) during the period September-October 2010. Table 5.1 summarizes the data samples main characteristics.
  The following generators have been used in this analysis:

- Pythia 6 [2]. This Monte Carlo has been used to simulate the Drell-Yan (DY) events decaying into ee($\mu\mu$) (see chapter 1, section 1.3).
  We consider two different "tunes"[1] of Pythia 6: D6T and Z2. They are optimized to describe the available experimental data on charged particle multiplicities and underlying events activity from previous experiments. D6T tune has been produced using CTEQ6L parton distri-

---

[1]Different setting of the Pythia internal parameters

	RunA	RunB
Period (2010)	04-08	09-10
L_{BX} ($\cdot 10^{30} cm^{-2} s^{-1}$)	0.1-0.2	0.2-0.7
Dataset Name (ee)	EG/Dec22	Electron/Dec22
Dataset Name ($\mu\mu$)	Mu/Dec22	Mu/Dec22
Events (ee)	53380790	33074402
Events ($\mu\mu$)	51860222	33288128
Selection (electron)	$p_T \geq$15 GeV	$p_T \geq$15 GeV
Selection (muon)	$p_T \geq$9 GeV	$p_T \geq$9 GeV

Table 5.1: *Datasets most relevant characteristics.*

bution functions. It has been done according to the Tevatron available data. Z2 tuning has been produced using the CMS and ATLAS preliminary data at 900 GeV and 7 TeV.

- Diffractive PomPyt. This Monte Carlo simulates the diffractive Z boson production.
  This program makes use of Pythia 5.7 to access a wealth of hard scattering processes and JETSET 7.4 for hadronization according to the Lund string model [68],[69].
  The diffractive processes have been simulated using the interaction of the Pomeron (see Chapter 1), a color-neutral object. The schematic diagram of the single-diffractive Z production with Pomeron exchange is shown in Fig. 5.1.
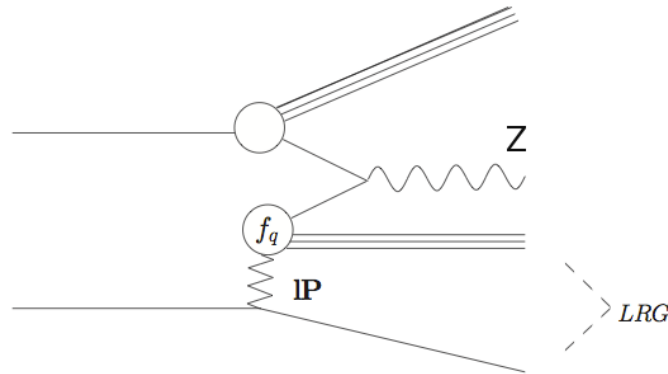
Figure 5.1: *Schematic diagram of a single-diffractive Z production with Pomeron exchange.*

- Dissociative PomPyt. PomPyt simulates the diffractive events in which the proton, after the Pomeron exchange, splits into a leading baryon and into a system of particles (Y). The diagram is presented in Fig. 5.2.
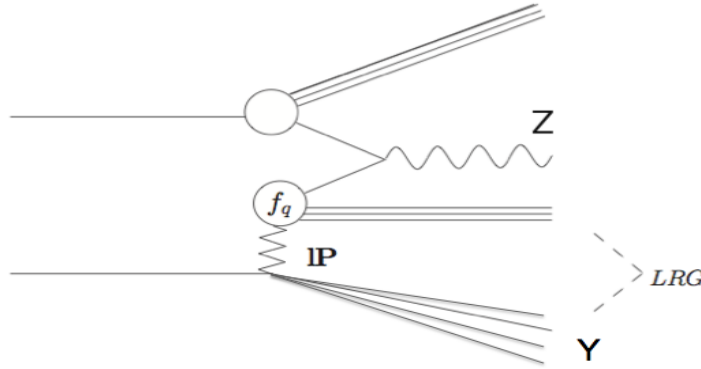
Figure 5.2: *Feyman Diagram of a dissociative event.*

Both Pythia and PomPyt include a description of soft diffractive events (both single-diffractive and double-diffractive), while the hard diffractive part (to describe the production of W and Z bosons) is only simulated using the PomPyt generator.

The Monte Carlo cross sections, the number of generated events and the corresponding integrated luminosities are summarized in the table 5.2. The cross sections are derived from existing data.

The samples used in this analysis were processed through the CMS detector (GEANT4 [65]) simulation, trigger emulation and recostruction packages. Simulated events were reconstructed in the same way as collision data.

5.2 Z Candidates Selection

The Z events selection has been worked out by the CMS Electroweak Group [70], optimizing simultaneously identification and isolation criteria to give approximately 95% selection efficiency. The selection cuts are described in this section as well as their efficiencies for both the Z→ee and Z→ $\mu\mu$ decays. The efficiencies for lepton reconstruction, identification, isolation and trigger are obtained from data. Efficiency correction factors are obtained as ratios of

e^+e^-			
MC Dataset	Cross Section (pb)	Gen. events	Integr. Luminosity (pb^{-1})
Pythia D6T	1300	2471816	1901.40
Pythia Z2	1300	2127607	1636.62
PomPyt	210.5	10000	47.51
Pompyt Diss.	210.5	14000	68.88
$\mu^+\mu^-$			
MC Dataset	Cross Section (pb)	Gen. events	Integr. Luminosity (pb^{-1})
Pythia D6T	1300	2552015	1963.09
Pythia Z2	1300	2289913	1761.47
PomPyt	210.5	10000	47.51
PomPyt Diss.	210.5	14000	68.88

Table 5.2: *Cross section, number of generated events and integrated luminosity for Monte Carlo data samples (ee and μμ).*

"tag-and-probe" [66] efficiencies for the data and for the simulation, and then applied to correct the above efficiencies. The tag-and-probe sample for the measurement of a given efficiency contains events selected with two lepton candidates with an invariant mass in the range [60-120] GeV. One lepton, called "tag", satisfies tight requirements. The other lepton, called "probe", is selected with criteria that depends on the efficiency being measured.

The efficiency of the lepton isolation requirements can also be measured using the "random-cone" technique [67]. In the inclusive Z sample, energy contributing to the isolation variables comes mainly from the underlying event, which can be sampled in directions uncorrelated with the lepton directions in a particular event. Leptons in simulated signal events are used to define directions in data events where the isolation energies can be measured and compared to the requirements of the analysis; this ensures a sampling of phase space that mimics the leptons in real data events.

5.2.1 Z→ee selection criteria

A Z candidate is identified in the CMS detector selecting two high p_t electrons as cluster of ECAL energy deposits matched to tracks in the silicon tracker. Each electron have to:

- pass a Level 1 trigger filter, which requires a coarse-granularity region of the ECAL to have $E_T \geq 5$ GeV.

- pass the High Level Trigger software filter, requiring an ECAL cluster of $E_T \geq 15$ GeV.

- be reconstructed in the fiducial region of ECAL, $0 \leq | \eta | \leq 1.44$ and $1.57 \leq | \eta | \leq 2.5$, where the transition region between the Endcap and the Barrel has been excluded.

ECAL clusters are required to match the tracks using an algorithm [70] which accounts for possible energy loss due to bremsstrahlung effects. The suppression of misidentified electrons is obtained by:

- Requiring the track trajectory, extrapolated to the ECAL, to match the ECAL cluster in the coordinates η and ϕ

- Limiting the amount of the HCAL hadronic energy measured in a cone of $\Delta R = \sqrt{(\Delta \eta)^2 + (\Delta \phi)^2} \leq 0.15$ around the ECAL cluster direction and requiring a narrow ECAL cluster width in η to reject the π contribution.

- Demanding no missing tracker hits before the first hit in the reconstructed track assigned to the electron, in order to avoid the electrons from photon conversions. If a partner track is found with an x-y distance to the electron track when both are parallel less then 0.02 cm, and forming a small opening angle with the electron track, the candidate is also rejected.

- Limiting the sums (excluding the electron candidate) of HCAL E_T, ECAL E_T and tracks p_T in a cone of $\Delta R \leq 0.3$ around the electron candidate direction, in order to isolate the electrons. These criteria ensure that misidentified particles, as well as electrons arising from jets are suppressed.

- Rejecting the Barrel spikes. Anomalous signals in the ECAL Barrel have been observed in collision events: they are due to hadronic interactions produced during *pp* collisions. These type of events have been demonstrated to be consistent with a direct ionisation in the APDs, causing a fake high energy deposits in the crystal. This anomalous signal is removed at HLT level applying the "Swiss Cross" rejection criterion: $(1 - \frac{E_1}{E_4}) \leq 0.95$ which rejects energy deposits in a single crystal. The comparison between the energy in a single crystal (E_1) to the summed energy in the four adjacent crystals in η and ϕ (E_4) is calculated for each channel. The spikes are removed offline using the topology and the timing of the event.

Moreover, the Z invariant mass is required to be within the range [60-120] GeV.

5.2.1.1   Z→ee selection efficiencies

The overall electron efficiency is the product of three terms: the reconstruction efficiency (ϵ_{REC}), the offline selection efficiency (ϵ_{SEL}) and the trigger efficiency (estimated from minimum bias collisions) of L1 and HLT (ϵ_{TRG}). In Tables 5.3,5.4, a summary of the efficiencies estimated with the tag-and-probe method are shown respectively for Barrel and Endcaps.

Barrel			
Efficiency	Data [%]	Simulation [%]	Ratio
ϵ_{REC}	98.6±0.5	98.5	1.001±0.005
ϵ_{SEL}	93.9±1.5	96.4	0.974±0.016
ϵ_{TRG}	98.5±0.2	99.4	0.992±0.002
ϵ_{TOTAL}	91.3±1.5	94.4	0.967±0.016

Table 5.3: *Tag-and-probe efficiencies (data, MC) and correction factors in the Barrel.*

Endcaps			
Efficiency	Data [%]	Simulation [%]	Ratio
ϵ_{REC}	96.2±0.8	96.3	0.999±0.009
ϵ_{SEL}	90.3±1.9	93.9	0.962±0.020
ϵ_{TRG}	99.16±0.02	97.7	1.015±0.003
ϵ_{TOTAL}	86.1±1.9	88.3	0.975±0.022

Table 5.4: *Tag-and-probe efficiencies (data, MC) and correction factors in the Endcaps.*

The product of all the efficiency is $91.3 \pm 1.5\%$ in the Barrel and $86.1 \pm 1.9\%$ in the Endcaps.

5.2.2   Z→ $\mu\mu$ selection criteria

The HLT trigger requires information from both the muon chambers and the inner tracking: an event having a muon with $p_T \geq 9$ GeV/c in the $\mid \eta \mid \leq 2.1$

region is then accepted.

A muon candidate must be reconstructed both as a "tracker muons", that starts from the inner tracker information, and as a "global muons", that starts from segments in the muon chambers.

To suppress signals from fake muons, the following is required:

- $\frac{\chi^2}{ndof} \leq 10$, on a global fit containing all tracks and muon hits

- At least two muon stations fired

- Only tracks with more than 10 hits in the tracker and at least one hit in the pixel detector.

- Transverse impact parameter[2] less than 2mm, in order to reject the muons from cosmic rays.

- Isolation criteria as for the electrons

Moreover, the Z invariant mass is required to be within the range [60-120] GeV.

5.2.2.1   Z→ $\mu\mu$ selection efficiencies

The total muon efficiency is the convolution of three different components:

- the efficiency to find a track in the inner tracker (ϵ_{TK}). The inner-tracker efficiency is studied using well reconstructed tracks in the muon chambers as probes.

- the efficiency to find a track in the muon chambers (ϵ_{SA}). The efficiency for tracking in the muon chambers is tested with tracker muons satisfying very loose matching to muon track segments.

- the efficiency in the remaining set of identification cuts (ϵ_{SEL} and ϵ_{ISO}) and trigger (ϵ_{TGR}).

The efficiencies are summarized in Table 5.5.

The overall muon selection efficiency is (82.8±1.0)%.

The Z→ $\mu\mu$,ee invariant mass spectra are presented in Fig. 5.3. The different shape of the two distributions is due to a known problem in the ECAL calibration, that will be corrected in the next reprocessing of the data. This difference does not affect the analysis results because no further conditions on the Z mass are requested.

---

[2]distance to the beam spot position

Muons			
Efficiency	Data [%]	Simulation [%]	Ratio
ϵ_{SA}	96.4±0.5	97.2	0.992±0.005
ϵ_{SEL}	99.7±0.3	99.7	1.000±0.003
ϵ_{TRK}	99.1±0.4	99.3	0.998±0.003
ϵ_{ISO}	98.5±0.4	99.1	0.994±0.004
ϵ_{TRG}	88.3±0.8	93.2	0.947±0.009
ϵ_{TOTAL}	82.8±1.0	88.7	0.933±0.012

Table 5.5: *Tag-and-probe efficiencies (data,MC) and correction factors for muons.*
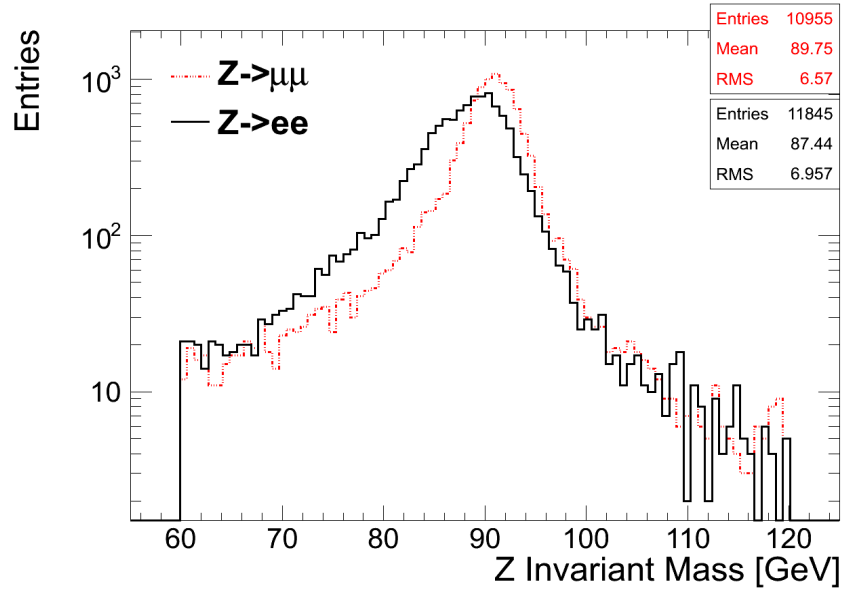
Figure 5.3: *Invariant mass spectrum for both the Z→ μμ,ee dataset.*

5.3 Diffractive Events Selection

The overall number of Z bosons thus selected, with the additional requirement of having all subdetectors fully operational is 21800 (see Table 5.6). The corresponding integrated luminosity is $(31.3\pm1.2)pb^{-1}$.

The analysis has been done using the Particle Flow algorithm to reconstruct

Number of Z→ee	Number of Z→ $\mu\mu$	Total
11845	10955	21800

Table 5.6: *Number of Z Bosons reconstructed from the two datasets.*

the physics objects in the events [72].

5.3.1 Particle Flow Reconstruction

The Particle Flow (PF) method aims at reconstructing and identifying all stable particles in the event, i.e., electrons, muons, photons, charged hadrons and neutral hadrons, with a thorough combination of all CMS sub-detectors (under the form of charged-particle tracks, calorimeter clusters, and muon tracks) for an optimal determination of their direction, energy and type. It makes use of two advanced algorithms:

- the iterative-tracking algorithm. First tracks are seeded and reconstructed with very tight criteria, leading to a moderate tracking efficiency, but a negligibly small fake rate. The next steps proceed by removing hits unambiguously assigned to the tracks found in the previous iteration, and by progressively loosening track seeding criteria. The softer seeding criteria increase the tracking efficiency, while the hit removal allows the fake rate to be kept low due to the reduced combinatorics[3]. With this iterative technique, charged particles with as little as three hits, a p_T as small as 150 MeV/c and a vertex more than 50 cm away from the beam axis, are reconstructed with a fake rate of the order of a per cent.

- the clustering algorithm. It is performed in three steps:

---

[3]In the first three iterations, tracks originating within a thin cylinder around the beam axis are found with an efficiency of 99.5% for isolated muons in the tracker acceptance, and larger than 90% for charged hadrons in jets. The fourth and fifth iterations have relaxed constraints on the origin vertex, which allows the reconstruction of secondary charged particles originating from photon conversions and nuclear interactions in the tracker material, and from the decay of long-lived particles such as K_0 or Λ

- "cluster seeds" are identified as local calorimeter cell energy maxima above a given energy.

- "topological clusters" are grown from the seeds by aggregating cells with at least one side in common with a cell already in the cluster, and with an energy in excess of a given threshold[4]. A topological cluster gives rise to as many "particle-flow clusters" as seeds.

- The calorimeter granularity is exploited by sharing the energy of each cell among all particle-flow clusters according to the cell-cluster distance, with an iterative determination of the cluster energies and positions.

In order to distinguish noise from signal, the following thresholds in the PF algorithms have been used:

Particle type	Position	Particle Flow Threshold (GeV)
Charged Particle	No restrictions	$p_T \geq 0.5$
Neutral	Barrel	Energy ≥ 1.5
Neutral	Endcap	Energy ≥ 2.0
Neutral	HF	Energy ≥ 4.0

Table 5.7: *Particle flow thresholds introduced in our studies.*

5.3.2   Definition Of The Variables In The Diffractive Selection

This analysis uses the following variables:

- $E \pm p_z = \sum_i (E_i \pm p_{z,i})$
  Where i runs over every particles of the event, reconstructed up to the HF acceptance ($3 \leq \eta \leq 5$). This is the sum of the energy and the longitudinal momentum of each particle. The $\pm$ sign is selected according to the Pomeron direction (+z or -z).

- HF Energy
  The energy deposit in HF is computed calculating the energy sum of

---

[4]These thresholds represent two standard deviations of the electronics noise in the ECAL (i.e. 80 MeV in the Barrel and up to 300 MeV in the end-caps) and amount to 800 MeV in the HCAL

all the HF towers, above a threshold of 4 GeV (see table 5.7). It is also divided into two variables, HF Energy minus and plus, according to the detector side.

- $\zeta^{\pm} = \frac{1}{\sqrt{s}} \sum_i E_{T,i} e^{\pm \eta_i}$
  Where E_T is the transverse energy of a given particle, η_i its pseudorapidity (i runs over every particles reconstructed from the particle flow algorithm). This variable corresponds to the fractional momentum loss of the scattered proton in the diffractive events. It is therefore connected to the E$\pm p_z$ variable.

- M_X
  In a diffractive reaction pp→pX, this variable refers to the final system X: M_X is defined as the X system invariant mass.

- etaMax,etaMin
  The highest (lowest) eta value of the reconstructed particles in the events.

- etaGap
  It is the width of the visible largest gap in the event.

- CASTOR energy
  The energy deposit in CASTOR calorimeter above a given threshold. Moreover the timing of each rec hit which compose the CASTOR tower signal have been checked to be consistent. Unfortunately only the minus side of the CMS detector has been equipped with CASTOR.

These variables make use of the particle flow reconstruction algorithms presented previously.

5.3.3   Diffractive Events Selection Using Monte Carlo

The conventional way to recognize a diffractive event is to look for rapidity gap in its particle flow. Since gaps are exponentially suppressed in QCD fragmentation[5], the cut on rapidity gap increases the relative fraction of diffractive events.
 Given the incomplete rapidity coverage of the detector and the high energy of the incoming protons available at LHC, the majority of the diffractive

---

[5]Described in details in Chapter 1
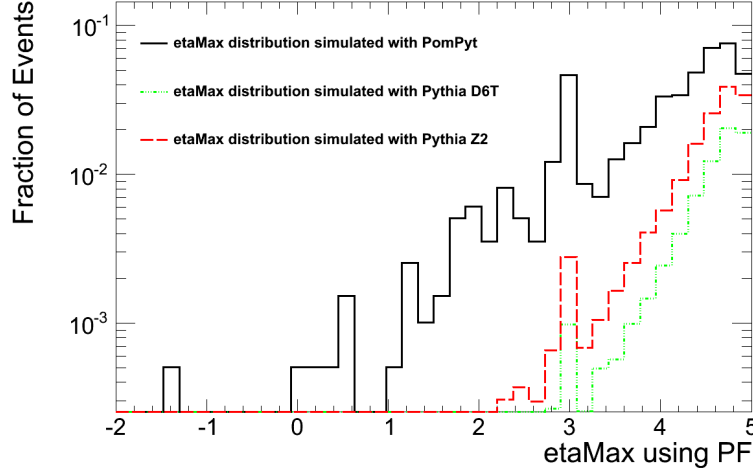
Figure 5.4: *The fraction of events as a function of "etaMax" is presented. The three Monte Carlo have been used: Monte Carlo PomPyt Diffractive (black), Pythia D6T (light grey dotted line) and Z2 (dark grey dashed line).*

events do not have a *visible* large rapidity gap (LRG). In Fig. 5.4, the eta-Max distribution is presented (calculated using the two Pythia Monte Carlos and PomPyt). The y-axis of the figure represent the fraction of events inside each etaMax bin. In the Table 5.8, the fraction of events selected applying different etaMax cuts is presented.

When requiring zero energy in at least one of the HF subdetectors (*sumHF=0*, equivalent to the $|\eta_{max}| \leq 3$ cut), according to Table 5.8, only 9.6% of the diffractive events is selected.

In order to study the signal selection efficiency and the background rejection

	$\eta_{max} \leq 1$	$\eta_{max} \leq 2$	$\eta_{max} \leq 2.5$	$\eta_{max} \leq 3$	$\eta_{max} \leq 3.5$	$\eta_{max} \leq 4$
PomPyt	0.3%	2%	3.6%	9.6%	12.0%	17.9%
D6T	$0.7 \cdot 10^{-2}$%	$0.3 \cdot 10^{-1}$%	$0.6 \cdot 10^{-1}$%	0.2%	0.3%	0.6%
Z2	$0.2 \cdot 10^{-1}$%	$0.9 \cdot 10^{-1}$%	0.2%	0.5%	0.7%	2.0%

Table 5.8: *Fraction of events selected applying different etaMax cuts, using the two tunes of Pythia 6 and Pompyt.*

of this cut, the fraction of events which have zero energy in one of the two HF calorimeters has been measured (table 5.9) for each of the ee simulated sample of Table 5.2.

Let's consider the following double ratios:

Dataset	Total Number of Events	Events when sumHF=0	ratio
Data RunA+B	11845	21	$1.77 \cdot 10^{-3}$
Pompyt	1975	378	0.19
Pythia D6T	2471816	1661	$6.72 \cdot 10^{-4}$
Pythia Z2	2127607	4958	$2.33 \cdot 10^{-3}$

Table 5.9: *Z→ee decay only: signal selection efficiency and the background rejection for the sumHF=0 cut. Data, PomPyt and Pythia datasets have been analyzed.*

$$R_{Pompyt/bkg_{D6T}} = \frac{Ratio_{Pompyt}}{Ratio_{Pythia_{D6T}}} = \frac{0.19}{0.0006} \sim 320 \qquad (5.1)$$

$$R_{Pompyt/bkg_{Z2}} = \frac{Ratio_{Pompyt}}{Ratio_{Pythia_{Z2}}} = \frac{0.19}{0.002} \sim 95 \qquad (5.2)$$

The $R_{PomPyt/bkg_{D6T}}$ and $R_{PomPyt/bkg_{Z2}}$ values are very high, which indicates that only a small fraction of the background survives the sumHF=0 cut. Unfortunately, the energy deposits in the forward region (especially in HF calorimeters) might be pile-up (PU) dependent. At higher luminosity a LRG might be closed by the contribution from the PU events.

5.4 Pile-up Studies

During the 2010, the instantaneous luminosity increased continuously therefore the pile-up conditions during the data taking were different. In figure 5.5 the instantaneous bunch crossing luminosity[6] is presented as a function of the run number. Dark grey points are the events which were taken during the RunB period, while the light grey dots refers to the RunA period. Figure 5.5 shows that also within each period the instantaneous luminosity per bunch crossing changed.

The number of PU events follows a Poisson distribution:

$$P(n) = \frac{(\mathscr{L} \cdot \sigma)^n e^{-\mathscr{L} \cdot \sigma}}{n!} \qquad (5.3)$$

where σ is the total inelastic cross section and $\mathscr{L}$ the bunch crossing instantaneous luminosity.

---

[6]The instantaneous luminosity divided by the number of bunches
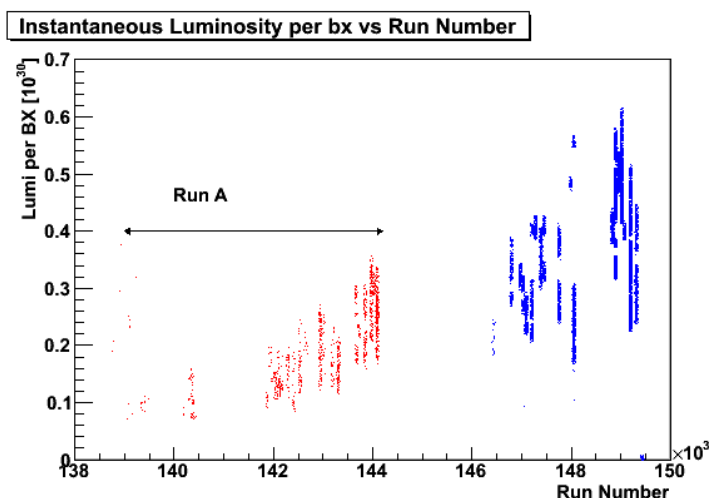
Figure 5.5: *The instantaneous bunch crossing luminosity as a function of the Run Number. Dark grey points are the events which were taken during RunB, while the light grey dots refers to the RunA.*

We estimate the number of pile up events as the number of reconstructed extra vertices, i.e. the total number of vertices minus one. In figure 5.6 the fraction of times we had a given number of pile-up events (PU=0 in the top left plot, PU=1 in the top right plot, PU=2 in the bottom left plot and PU=3-8 in the bottom right plot) as a function of the beam bunch crossing luminosity is presented. The distributions have been fitted using the theoretical prediction (5.3): the agreement between the fit and the data is excellent. A PU interaction can be classified into two categories:

- "hard" interaction, in which detectable particles in the central region ($|\eta| \leq 2.4$) are produced

- "soft" interaction, which does not have a detectable activity in the $|\eta| \leq 2.4$ region.

As already introduced before, the negative effect of the pile-up is to fill the gap. A selection requiring only one vertex in the event removes the hard pile-up interaction component.

5.4.1 Pile-up During 2010

In figure 5.7, the number of Z→ee events collected by CMS in 2010 are presented as a function of the instantaneous luminosity per bunch crossing. The dashed area represents the first period of data taking (RunA), while the other
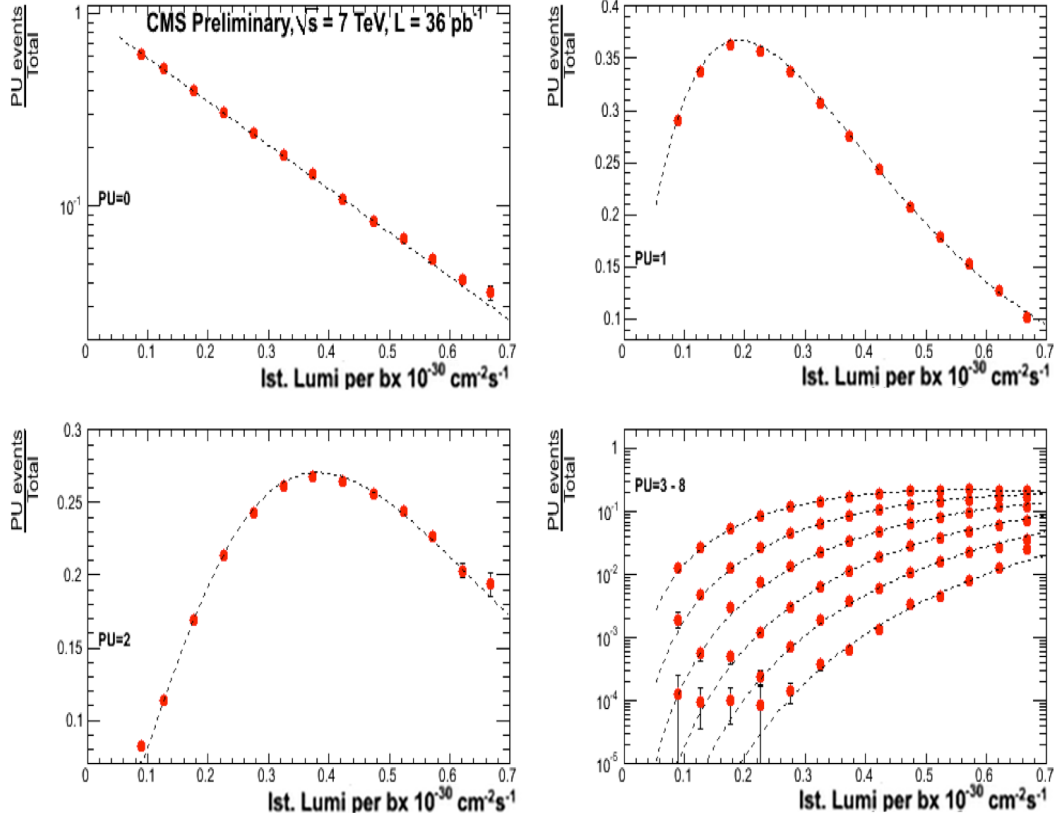
Figure 5.6: *Fraction of events with n pile up events as a function of the bunch luminosity. The dotted line is the poissonian fit. Pile-up (PU) = 0 in the top left plot, PU=1 in the top right plot, PU=2 in the bottom left plot and PU=3-8 in the bottom right plot.*

distribution represents the second (RunB). The RunA mean instantaneous luminosity per bunch crossing was $0.21 \cdot 10^{30} cm^{-2} s^{-1}$: this number, according to the formula (5.3), predicts an average of 1.1 pile up per event. In RunB data, collected at a mean instantaneous luminosity of $0.36 \cdot 10^{30} cm^{-2} s^{-1}$, one expects an average of 1.9 PU per event.

The distribution of the number of recorded vertices per event is presented in figure 5.8: the PU contribution is obtained removing the primary vertex from the counting. During the RunA, there were many events with 0 or 1 pile up event. When the luminosity increased (RunB), the distribution changed widely (figure 5.8), and the events at low PU became the minority.

Using the formula (5.3), it is possible to calculate analytically what is the probability to have an event without pile up as a function of the luminosity. This function is presented in figure 5.9: it is clear that the one vertex
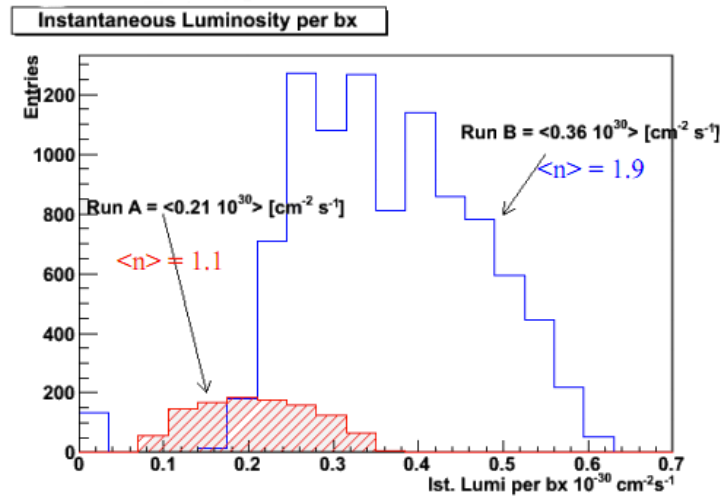
Figure 5.7: *Distribution of the Z→ee events collected by CMS in 2010, divided in bin of instantaneous luminosity. Dashed area and empty area distributions correspond respectively to RunA and RunB.*
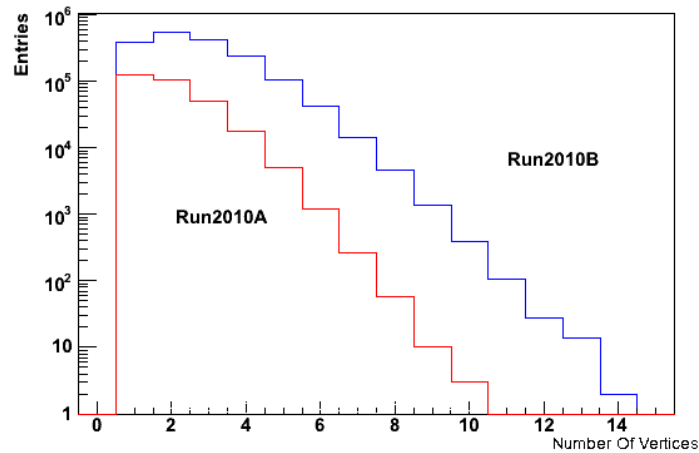
Figure 5.8: *The distribution of the number of recorded vertices (2010 data) during RunA and RunB.*

selection criterion has a lower efficiency at higher luminosities.

5.4.1.1 Effect Of The Pile Up On Observables

Pile up events cause a distortion on the shape of measured distribution. For example, the Min(EnergyHF-, EnergyHF+) (*MinHF*) distribution during
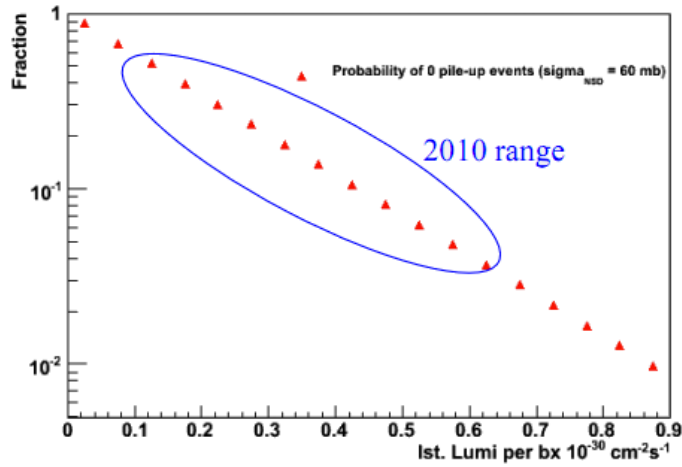
Figure 5.9: *Probability of having an event without pile up, calculated analytically from the formula 5.3.*

two different periods is shown in Fig. 5.10. The dark grey distribution has been obtained using a period with a average luminosity of $0.45 \cdot 10^{30} cm^{-2} s^{-1}$, while the light grey distribution has an average of $0.22 \cdot 10^{30} cm^{-2} s^{-1}$. The
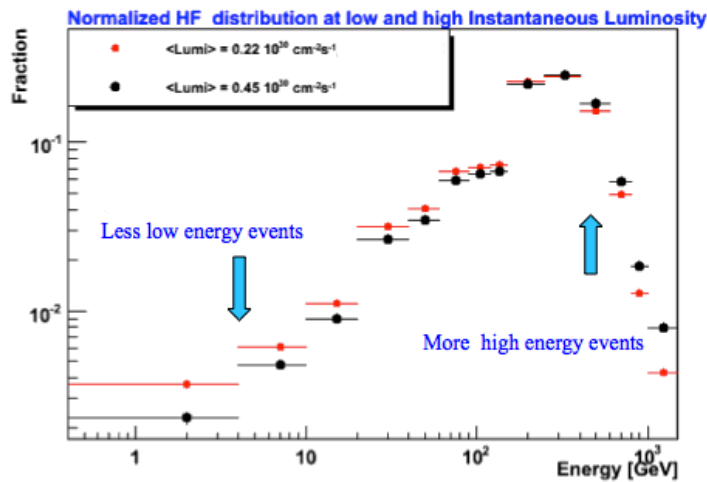
Figure 5.10: *distribution of the Min(EnergyHF-,EnergyHF+) distribution during two different periods.*

effect of the PU is to depopulate the low energy region, and to fill the high luminosity bin. In general, the energy distributions are shifted towards higher mean values.

5.4.2 Diffractive Events selection in data

We select diffractive events requiring *sumHF* equal to zero. The number of Z→ee and Z→ $\mu\mu$ events which pass the diffractive selection is 33 (0.15% of the total number). According to Table 5.9, we define two other variables:

$$R_{data/bkg_{D6T}} = \frac{Ratio_{Data}}{Ratio_{D6T}} = \frac{0.002}{0.0006} \sim 3 \qquad (5.4)$$

$$R_{data/bkg_{Z2}} = \frac{Ratio_{Data}}{Ratio_{Z2}} = \frac{0.002}{0.002} \sim 1 \qquad (5.5)$$

If we compare $R_{data/bkg_{D6T}}$ or $R_{data/bkg_{Z2}}$ with the MC ratios (5.1) and (5.2), there is a clear difference mostly due to the contribution of the pile up events, which are not taken into account in the Montecarlo datasets. To reduce the PU effect, we consider the sub-sample of events characterized by one vertex. In the analysis we have also used a vertex quality cut to select good vertex and to avoid fake vertices. It is based on the "Number Of Degrees of Freedom (NDOF)", defined as:

$$NDOF = 2 * \sum_{tracks} (weights) - 3 \qquad (5.6)$$

 where the sum runs over the tracks associated to a given vertex and weights is a number used to indicate the quality of the tracks (weights=1 means perfect track).

The effective integrated luminosity, considering only events with one vertex and NDOF $\geq$4, decreases then to 7.5 pb^{-1}.

As already presented in chapter 1, diffractive events appear as a peak at a very low value of the ζ variable, which reflects the peak of the cross section at small ζ. Fig. 5.11 shows the distribution of the reconstructed ζ variable in the PomPyt diffractive Monte Carlo. The dotted distribution, obtained using the diffractive selection, is almost totally contained within the range [0-0.03]. Moreover, as presented in Table 5.10, restricting the kinematic region in the same ζ range suppress strongly the background, making an enhancement of the signal/background ratio. The $\zeta \leq 0.03$ cut was therefore added to the diffractive selection criteria. In Table 5.11 the number of diffractive Z→ee and Z→ $\mu\mu$ events is presented, as a function of the ζ variable.

Summarizing, a diffractive event is selected requiring the following cuts:

- Energy in HF- or HF+ calorimeters equal to zero (*sumHF=0*)
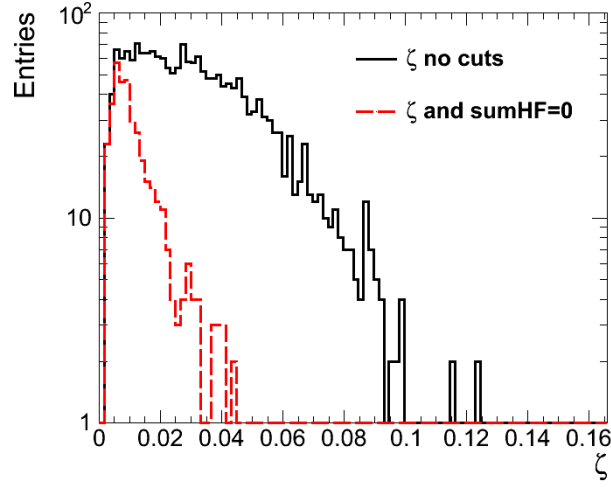
Figure 5.11: *Distribution of the reconstructed ζ variable, in the PomPyt diffractive Monte Carlo. The dotted line is the same distribution requiring sumHF=0.*

Dataset	% sumHF=0	% sumHF=0 and $\zeta \leq 0.03$
Data	$1.77 \cdot 10^{-3}$	$1.61 \cdot 10^{-3}$
Pompyt	0.19	0.18
Pythia D6T	$0.67 \cdot 10^{-3}$	$0.40 \cdot 10^{-3}$
Pythia Z2	$2.33 \cdot 10^{-3}$	$1.53 \cdot 10^{-3}$

Table 5.10: *Selection efficiency and the background rejection for the sumHF=0 and $\zeta \leq 0.03$ cuts.*

- only one vertex

- vertex NDOF ≥ 4

- $0 \leq \zeta \leq 0.03$

The total number of selected diffractive Z candidate is 18 (approximately 0.1% of the total Z candidates): their invariant mass is presented in Fig. 5.12.

Dataset	$0 \leq \zeta \leq 0.015$	$0.015 \leq \zeta \leq 0.03$
Z→ee	6	7
Z→ $\mu\mu$	2	3
Total	**8**	**10**

Table 5.11: *The number of events (Z→ee and Z→ $\mu\mu$) which pass the diffractive criteria, as a function of the ζ variable.*
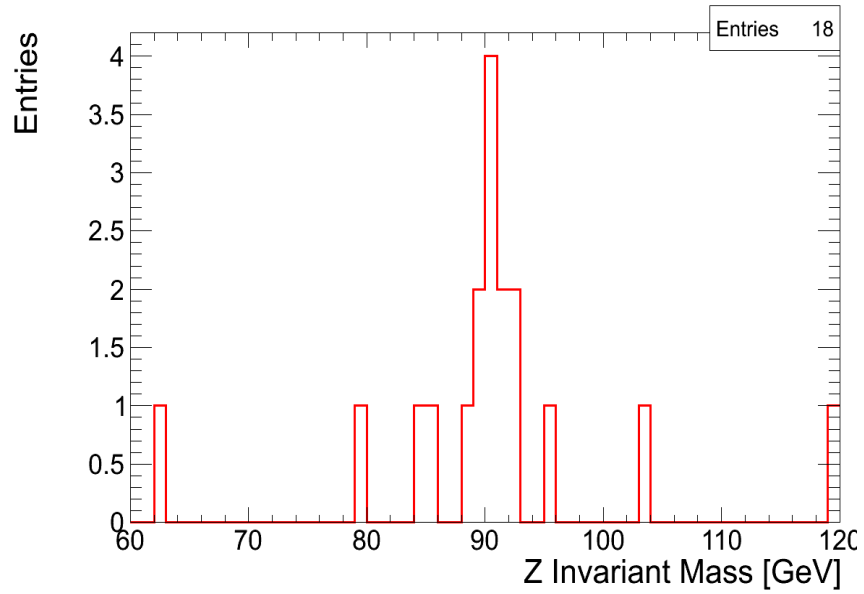
Figure 5.12: *Invariant mass spectrum of the selected diffractive Z. The Z→ $\mu\mu$,ee dataset are summed together.*

5.4.3 Treatment Of The Soft PU Contribution

The efficiency of the diffractive selection, which requires a visible rapidity gap of ~ 2 units (HF acceptance), depends upon the amount of pile-up (mainly the soft contribution) present in any given event. Events collected at higher luminosity have therefore a lower probability of being selected. According to formula (5.3), the probability to have zero PU events decreases as the instantaneous luminosity increases. To correct for this loss of selection efficiency, the following method has been implemented[7]:

- Considering only events with one visible vertex, plot the fraction of events with no energy in one of the two HF calorimeters as a function of the bunch crossing instantaneous luminosity. Fig.5.13 shows how the pile-up events are filling the gap in HF, making it more difficult for an event to still have sumHF=0.
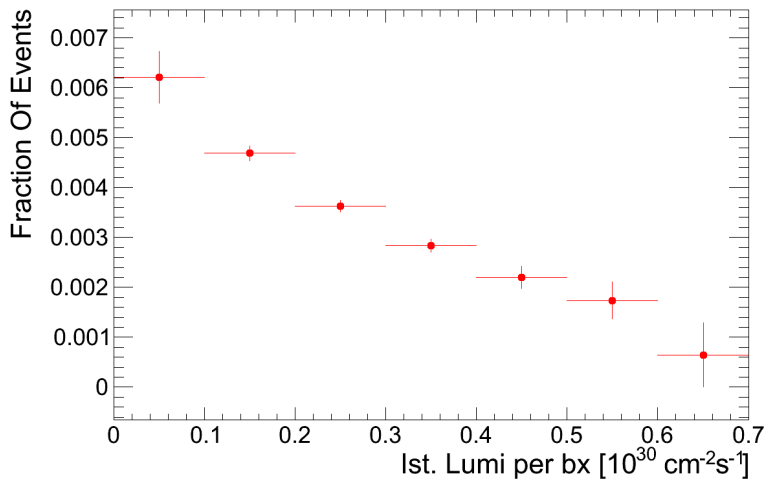
Figure 5.13: *Fraction of events having no energy in one of the two HF calorimeters as a function of the bunch crossing instantaneous luminosity. Only events with one visible vertex have been considered.*

- Fit the plot (Fig. 5.13) with a straight line. The result can be seen in Fig. 5.14.

- The fit in Fig. 5.14, after normalizing the intercept to one, represents the survival probability for sumHF=0 events with only one visible ver-

---

[7]For this study, an high statistics dataset has been used. The pile-up effect is in fact independent from the choice of the dataset
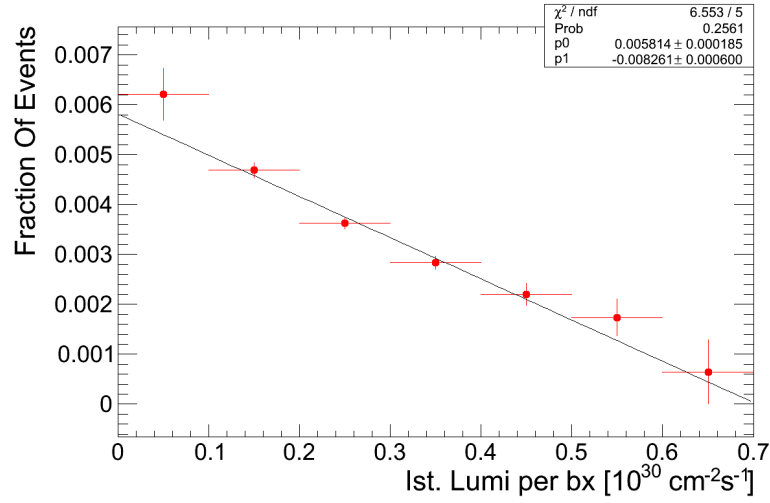
Figure 5.14: *Fraction of events having no energy in one of the two HF calorimeters as a function of the instantaneous luminosity and extrapolation to zero luminosity using a first order polynomial function.*

tex. To evaluate how many events we would have had without pile-up, we assign to each event a weight. This weight, always larger than one, is the inverse of the gap survival probability:

$$y_{FIT} = a + b * Lumi \tag{5.7}$$

$$y'_{CORR} = \frac{a}{y_{FIT}} = \frac{a}{a + b * Lumi} = \frac{1}{1 + \frac{b}{a}Lumi} \tag{5.8}$$

The correction as a function of the instantaneous luminosity per bunch crossing is shown in Fig. 5.15. As an example, the effect of this correction on the ζ distribution is presented in Fig. 5.16.
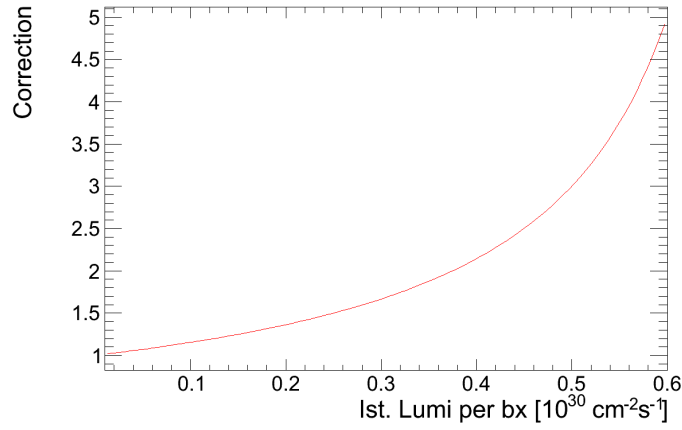
Figure 5.15: *Correction function used to re-weight the events with HF=0 energy in order to account for the pile-up effect.*
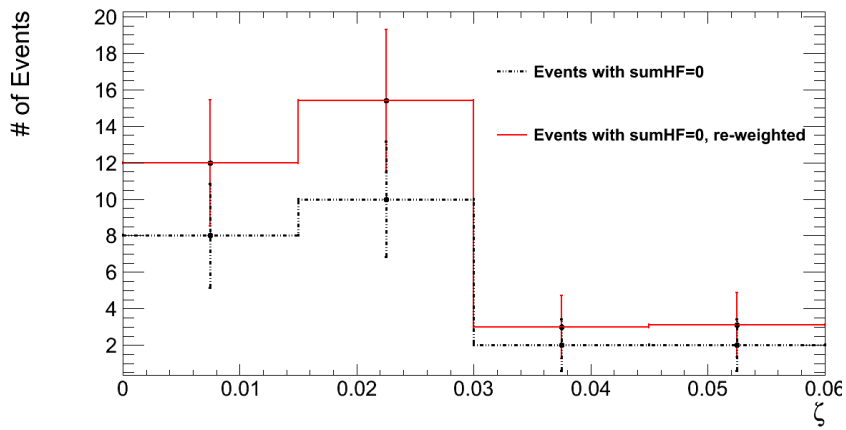
Figure 5.16: *ζ distribution: the dashed line represents the original ζ distribution, while the red solid one is obtained applying the correction function.*
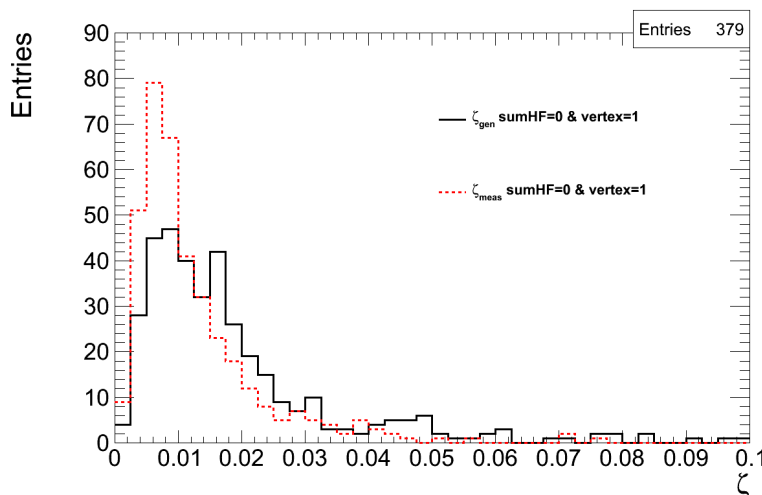
Figure 5.17: *Comparison between the generated ζ (black line) and the reconstructed ζ (light grey dashed line) distribution, simulated using PomPyt.*

5.5 MonteCarlo Signal Studies

In this section, a detailed study on the main properties of the diffractive Z events has been done using the PomPyt Monte Carlo.

In Fig. 5.17 a comparison between the generated (ζ_{gen}) and reconstructed (ζ_{meas}) ζ variables is presented. The reconstructed ζ is almost always underestimated if compared with the true value. This is due to the incomplete detector coverage (important effect at high energy) and to the use of the particle flows thresholds (important at low energy), which affect the reconstruction of the ζ variable[8]. Consequently a migration from high ζ_{gen} values to small ζ_{meas} value is expected.

To evaluate the impact of the migration effect, the following quantities are studied:

ζ **Resolution** Defined as the (relative) difference between the reconstructed and generated ζ.

ζ **Efficiency/Purity** These two quantities measure the quality of the ζ variable reconstruction.

ζ **Migration Map** A map in which the difference between ζ reconstructed

---

[8]The incomplete detector coverage is particularly important at higher energy, increasing the number of particles which escape the detector undetected. The particle flows thresholds effect is instead important at low energy, where the contribution of the particles below threshold become more important

and generated values is visualized.

Ideally to measure the signal in a proper way, the kinematic range $0 \leq \zeta \leq 0.03$ has to be splitted in as many bins as possible, in order to reproduce the cross section shape at best. The quantities introduced above strongly depend on the number of bins chosen to divide the region. The number of bins have been decided in such a way that the purity,efficiency and resolution are within the following limits:

- resolution $\leq$ 30-40 %

- purity $\geq$ 50%

- efficiency within the range [50-150]%

The measurement of the migration, efficiency, purity and resolution are presented below.

5.5.1   Signal Resolution

The ζ absolute and relative resolution are defined as follows:

$$R_{ABS} = \zeta_{meas} - \zeta_{gen} \tag{5.9}$$

$$R_{REL} = \frac{\zeta_{meas} - \zeta_{gen}}{\zeta_{meas}} \tag{5.10}$$

In figure 5.18 R_{ABS} and R_{REL} as a function of the ζ_{meas} are shown for diffractive Z events selected with sumHF=0, while Fig. 5.19 shows the R_{ABS} and R_{REL} one dimensional distributions. ζ measured is, on average 30% lower than the generated value, and its resolution is 28%.

Taking into account also the fact that we have a very small data sample, we decided to divide the kinematic region in two equal bins, having roughly twice the resolution size ($0 \leq \zeta \leq 0.015$ and $0.015 \leq \zeta \leq 0.03$).

5.5.2   Purity

The quantity *purity* is defined as follows:

$$\text{Purity} = \frac{\text{number of events generated and measured in the same bin}}{\text{number of events generated in bin}} \tag{5.11}$$

In Fig. 5.20 the Monte Carlo diffractive events purity is shown using the Z→ee selected events.
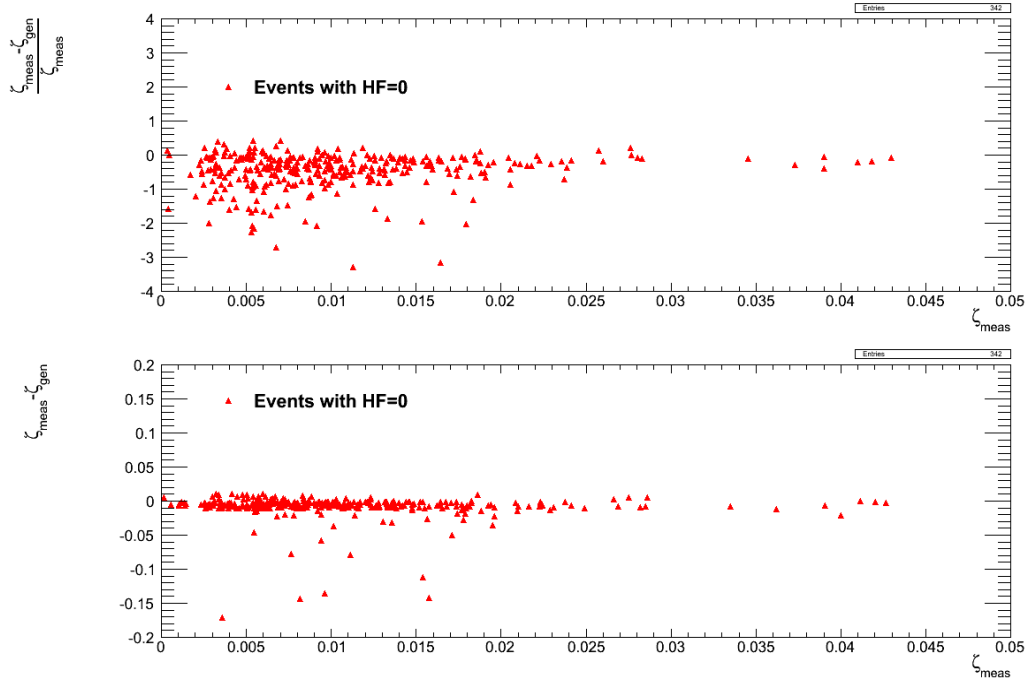
Figure 5.18: *R_{REL} and R_{ABS} as a function of the ζ_{meas} are shown: on the upper plot the relative (R_{REL}) resolution while the absolute resolution (R_{ABS}) is presented in the bottom plot, both of them calculated requiring all selection cuts and sumHF=0.*
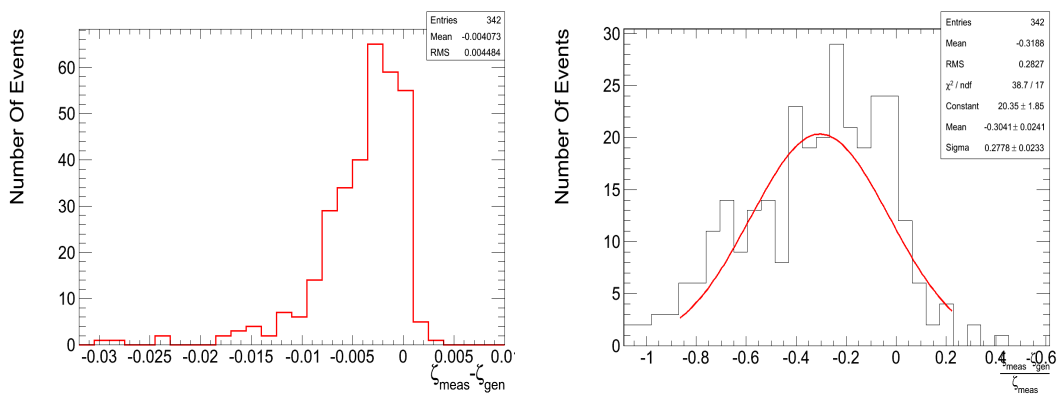
Figure 5.19: *One dimensional distribution of the R_{ABS} and R_{REL}, requiring all selection cuts and sumHF=0.*
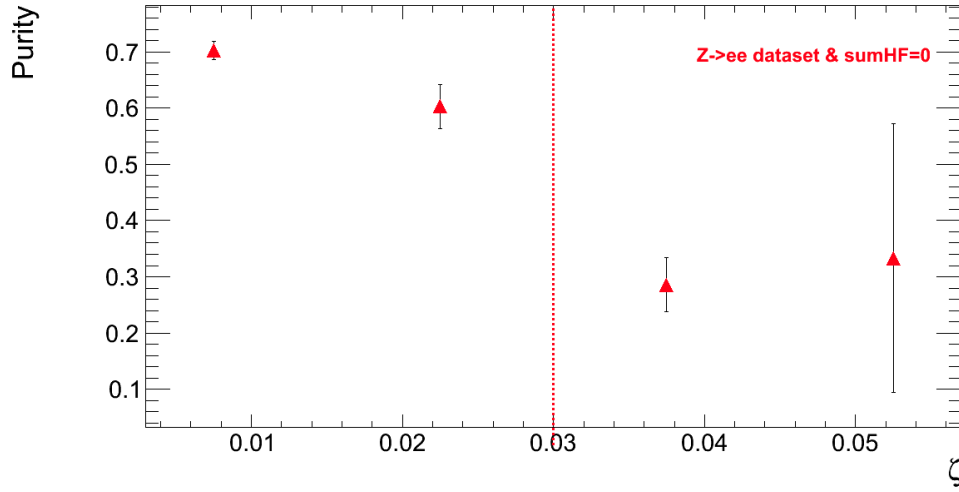
Figure 5.20: *Signal Purity (Z→ee dataset) computed using PomPyt Diffractive Montecarlo, after all selection cuts and sumHF=0. The dashed vertical line indicates our selection region (ζ ≤0.03).*

Figure 5.20 shows that, dividing the kinematic region in two bins and using the diffractive selection, the *purity* is well above 50%. A similar plot obtained from the Z→ $\mu\mu$ dataset confirms the same behaviour.

5.5.3 Efficiency

The signal *efficiency* is defined as follows:

$$\text{Efficiency} = \frac{\text{number of events measured in a bin}}{\text{number of events generated in a bin}} \tag{5.12}$$

In Fig. 5.21 the Monte Carlo diffractive events efficiency is shown using the Z→ee dataset.

Fig. 5.21 shows that, dividing the kinematic region in two bins and using the diffractive selection, the *efficiency* is within the range of [50%-150%]. The efficiency plot obtained from the Z→ $\mu\mu$ dataset confirms the same behaviour.

5.5.4 Migration Maps

Two different migration maps have been studied: the first one, called "origin map", is calculated in this way:

1. The events (requiring sumHF=0) are divided into two sub-samples,
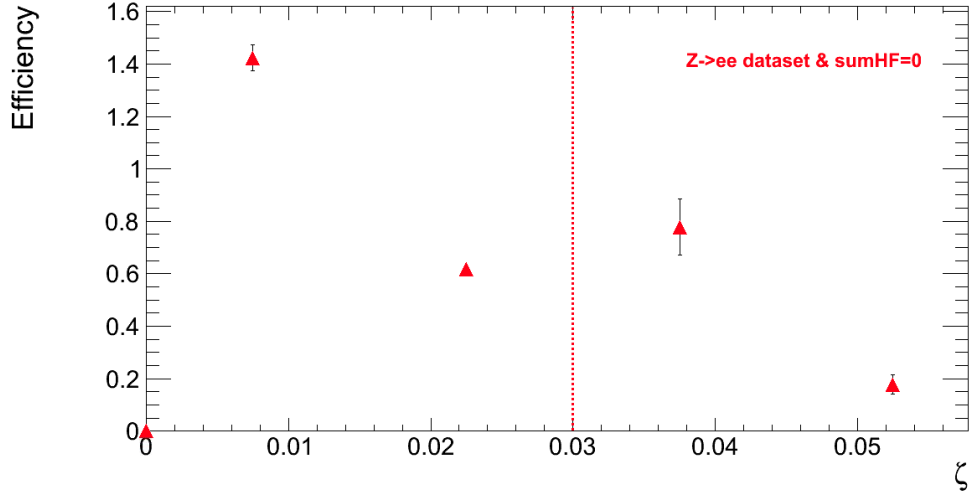
Figure 5.21: *Signal efficiency (Z→ee dataset), computed using PomPyt Diffractive Montecarlo, after all selection cuts and sumHF=0. The dashed vertical line indicates our selection region ($\zeta \leq 0.03$).*

according to their ζ_{meas} value (0-0.015 and 0.015-0.03). Only events which pass the diffractive cuts are accepted.

2. For each sample, the distribution of the ζ_{gen} of the events is presented.

Four plots are shown (Fig. 5.22): on the lefthand side, the ζ_{gen} of the events having $0 \leq \zeta_{meas} \leq 0.015$ (first bin), for the Z→ $\mu\mu$ (bottom) and Z→ee (top) datasets. On the righthand side, ζ_{gen} of the events having $0.015 \leq \zeta_{meas} \leq 0.03$ (second bin) is presented, for the Z→ $\mu\mu$ (bottom) and Z→ee (top) datasets. Fig. 5.22 shows that only very few points (1-2%) have a ζ_{gen}-ζ_{meas} difference greater than the bin width (0.015).

The second map, called "destination map", is obtained in the following two steps:

1. The events are divided into two samples, according to their ζ_{gen} value (0-0.015 and 0.015-0.03). Only events which pass the diffractive cuts are accepted.

2. For each sample, the distribution of the ζ_{meas} of the events is presented.

Fig. 5.23 presents: on the lefthand side, the ζ_{gen} of the events having $0 \leq \zeta_{meas} \leq 0.015$ (first bin), for the Z→ $\mu\mu$ (bottom) and Z→ee (top) datasets. On the righthand side, ζ_{gen} of the events having $0.015 \leq \zeta_{meas} \leq 0.03$ (second bin) is presented, for the Z→ $\mu\mu$ (bottom) and Z→ee (top) datasets.
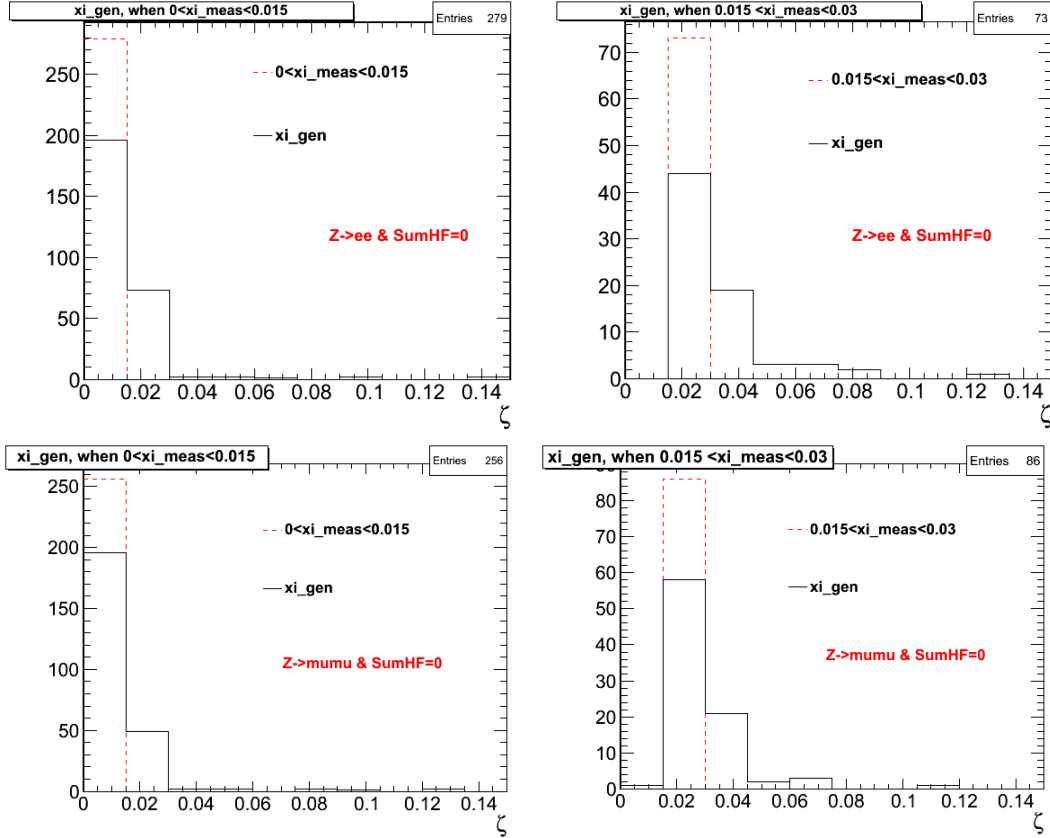
Figure 5.22: *"Origin Migration Map". On the lefthand side, the ζ_{gen} of the events having $0 \leq \zeta_{meas} \leq 0.015$ is presented, for the $Z \to \mu\mu$ (bottom) and $Z \to ee$ (top) datasets. On the righthand side, ζ_{gen} of the events having $0.015 \leq \zeta_{meas} \leq 0.03$ is presented, for the $Z \to \mu\mu$ (bottom) and $Z \to ee$ (top) datasets. (PomPyt Diffractive Montecarlo requiring all selection cuts and sumHF=0).*
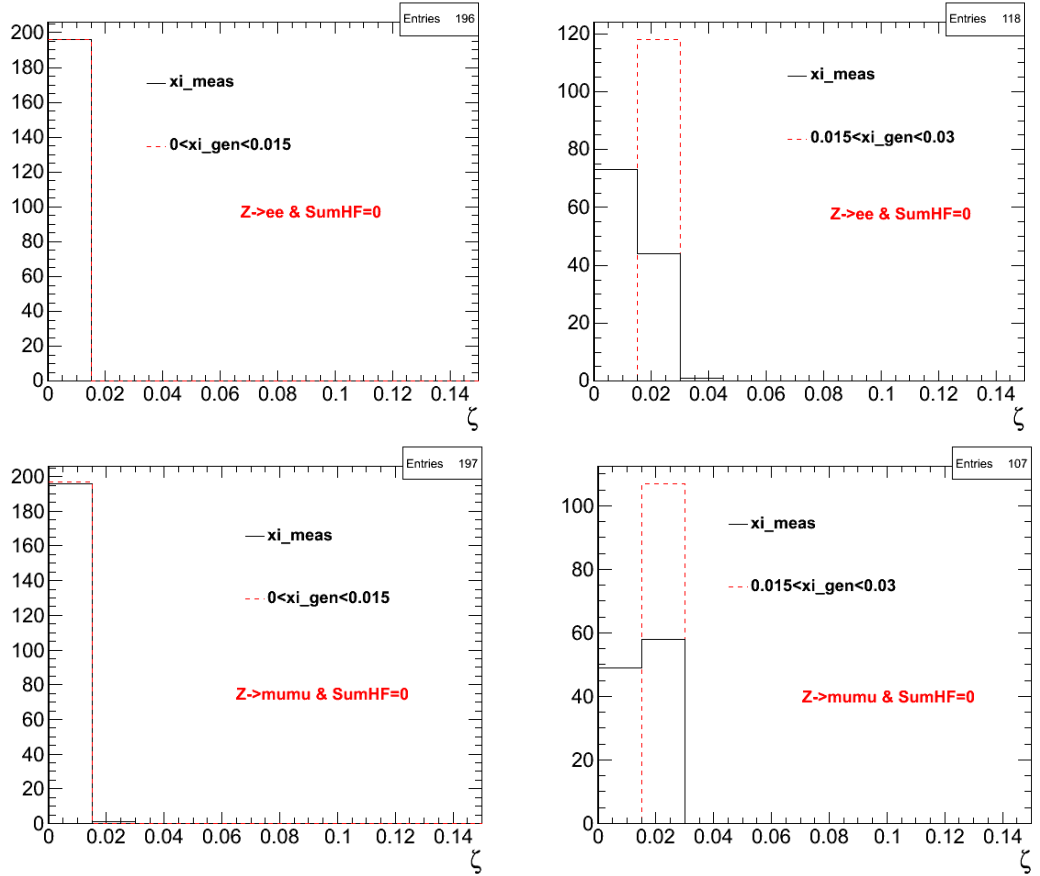
Figure 5.23: *"Destination Migration Map". On the lefthand side, the ζ_{meas} of the events having $0 \leq \zeta_{gen} \leq 0.015$ is presented, for the $Z \to \mu\mu$ (bottom) and $Z \to ee$ (top) datasets. On the righthand side, ζ_{meas} of the events having $0.015 \leq \zeta_{gen} \leq 0.03$ is presented, for the $Z \to \mu\mu$ (bottom) and $Z \to ee$ (top) datasets. (PomPyt Diffractive Montecarlo requiring all selection cuts and sumHF=0).*

Fig. 5.23 shows that all the points have a ζ_{gen}-ζ_{meas} difference lower than the bin width (0.015).

5.5.5 Conclusions

Given the poor statistics, the selected ζ_{meas} kinematic region has been divided into two equal bins. Under these conditions, the ζ resolution, efficiency, purity are within the limits. The cross section measurement will be performed in the region $0 \leq \zeta_{meas} \leq 0.03$.

5.5.6 Studies of diffractive events with proton dissociation

Single diffractive Z production with proton-dissociation can be described as:

$$pp \rightarrow XY \tag{5.13}$$

where X contains a Z boson and Y is a low-mass state into which the proton has diffractively dissociated. The probability for the Y system to escape undetected in the forward region depends on its mass. If this value is small, then each of the fragmentation products has on average low p_T value and the system remains close to the beamline. Viceversa, the probability of hitting the HF calorimeters is not negligible for high mass value.

In order to evaluate under which conditions the dissociative system starts to hit HF, we calculate the fraction of events that hit HF as a function of the Y mass (M_Y) (Fig. 5.24):

$$R(M_Y) = \frac{\text{Number of Dissociative events with sumHF=0}}{\text{Number of Dissociative events}} \tag{5.14}$$

The acceptance for low M_Y state is similar to that of non dissociative diffractive events, (roughly 20% of diffractive Z have sumHF=0), while as M_Y increases the acceptance decreases.

The distribution in Fig. 5.24 does not reach zero at higher Y mass; this is due to the fact that the products of M_Y fragmentation can actually miss HF. It is interesting to compare the number of events which pass the diffractive selection for the diffractive and the dissociative diffractive events. We compute the ratio:

$$\frac{diffractive_{sumHF=0}}{dissociative_{sumHF=0}} \tag{5.15}$$
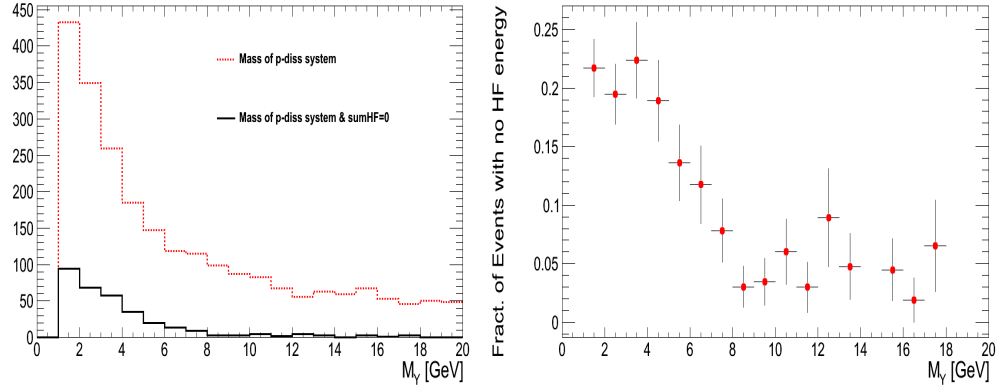
Figure 5.24: *On the left the M_Y distribution is presented for dissociative events (dotted line), and dissociative events with sumHF=0 cut (solid line). On the right the ratio of the two distributions is shown.*

normalized at the same integrated luminosity (since the dissociative cross section is not known, it has been supposed to be equal to the diffractive cross section).

The result is presented in Fig. 5.25. In the upper left plot, the ζ_{meas} distribution for both the Monte Carlo PomPyt diffractive and Monte Carlo PomPyt dissociative events is provided, normalized to the same number of events. The ratio between the two distributions is presented in the plot on the bottom left. On the upper right plot, the ζ_{meas} distribution for both the diffractive and dissociative events is provided, applying the diffractive selection. On the bottom right plot, the ratio between the two distributions is presented. From the bottom right plot fit, the $\frac{diffractive_{sumHF=0}}{dissociative_{sumHF=0}}$ can be estimated to be around 2.59±0.26.

Summarizing, with the assumption that diffractive and dissociative diffractive Z production have the same cross section, then our selection cuts preferentially select diffractive events above diffractive dissociative events.
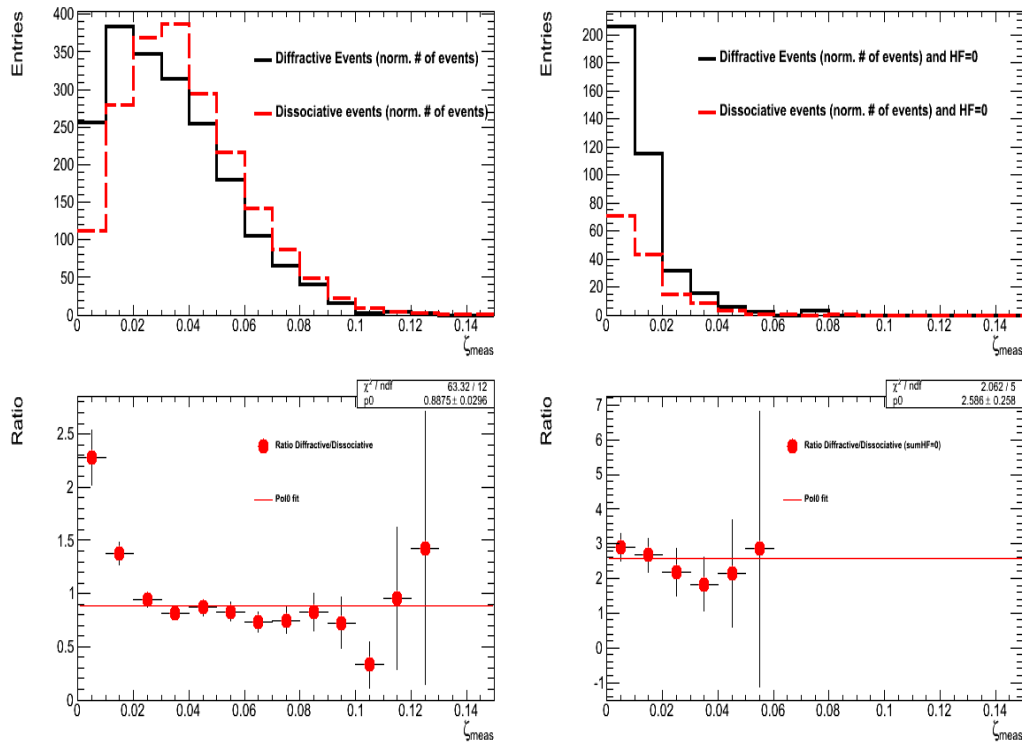
Figure 5.25: *In the upper left plot, the ζ_{meas} distribution for both the PomPyt Monte Carlo diffractive and PomPyt Monte Carlo dissociative events is shown, normalized to the same number of events. The ratio between the two distributions is in the plot on the bottom left. On the upper right plot, the ζ_{meas} distribution for both the diffractive and dissociative events is provided, applying the diffractive selection. On the bottom right plot, the ratio between the two distributions is presented.*

5.6   Non Diffractive Monte Carlo Studies

In this section we present the studies carried out in order to evaluate the Monte Carlo-data agreement.

We have used the Pythia 6 D6T and Z2 Monte Carlo samples, generated without pile-up events, i.e. they simulate only one interaction per event. They have been normalized to the data integrated luminosity.

It is therefore necessary to remove the pile-up contribution from the data events before being able to do a meaningful comparison. The method chosen to remove the effect of the pile-up is a generalization of the technique presented in section 5.4.3.

5.6.1   Pile-up Removal Method

The method presented in section 5.4.3 is used to obtain the number of events with sumHF=0 that we would have collected in absence of pile-up. The same technique can be applied to every energy bin of the HF distribution, evaluated with the MinHF variable, so that we can obtain the complete "pile-up free" MinHF energy distribution. The technique has been developed and validated using a high statistics data sample (2 leptons with p_T greater than 10 GeV, see Table.5.12) to avoid possible problems due to the small number of Z events.

In the following, the steps of the technique are explained:

Dataset Name	Number Of Events
/EG/Run2010A-DiLeptonEle-Dec22Skim	1019114
/Electron/Run2010B-DiLeptonEle-Dec22Skim	3569988

Table 5.12: *The high statistics di-lepton datasets.*

- The distribution is divided into energy bins. The number of bins and their width is chosen in order to distribute the bins statistics. We have chosen to divide the energy range in 12 bins:

$$\text{HF Energy intervals [GeV]} = 0\text{-}4, 4\text{-}10, 10\text{-}20, 20\text{-}40, 40\text{-}60, \\ 60\text{-}90, 90\text{-}120, 120\text{-}150, 150\text{-}250, 250\text{-}400, 400\text{-}700, 700\text{-}3000 \tag{5.16}$$

- For each bin, the fraction of events as a function of the instantaneous luminosity is measured, as already explained in section 5.4.3.

Figure 5.26: *Fraction of events populating different MinHF energy bins as a function of the instantaneous luminosity. The extrapolation to zero luminosity provides the estimation of the "pile-up" free population of the bin.*

- The extrapolation to zero luminosity provides an estimate of the pile-up free number of events in each bin of MinHF.

Two sets of events have been used for this unfolding:

- Events with any number of pile-up events. For this dataset the extrapolation is quite steep since at higher luminosity the number of pile-up events is large. The final result can be seen in Fig. 5.26.

- Events that only have one visible vertex, i.e. only pile-up events which do not make a vertex are still present. For this second dataset, the

extrapolation is shallower as the amount of energy due to the pile-up is much lower. Unfortunately, the lower statistics implies bigger errors on the intercept measurement. In Fig. 5.27 the plots are presented.

Figure 5.27: *Fraction of events populating different MinHF energy bins as a function of the instantaneous luminosity. The condition "one vertex only" has been required. The extrapolation to zero luminosity provides the estimation of the "pile-up" free population of the bin.*

Both methods should give the same extrapolation[9], so it's interesting to fit them together, requiring a common intercept. The combined fit has the strenght of the two previous methods: it is presented in Fig. 5.28. A straight line and a polynomial function have been used to fit the two distributions.

---

[9]The pile-up distribution depends only on the total inelastic cross section and the instantaneous luminosity per bunch crossing, as presented in formula (5.3). The pile-up effect disappears when the luminosity reaches zero, regardless the choice of the data sample.
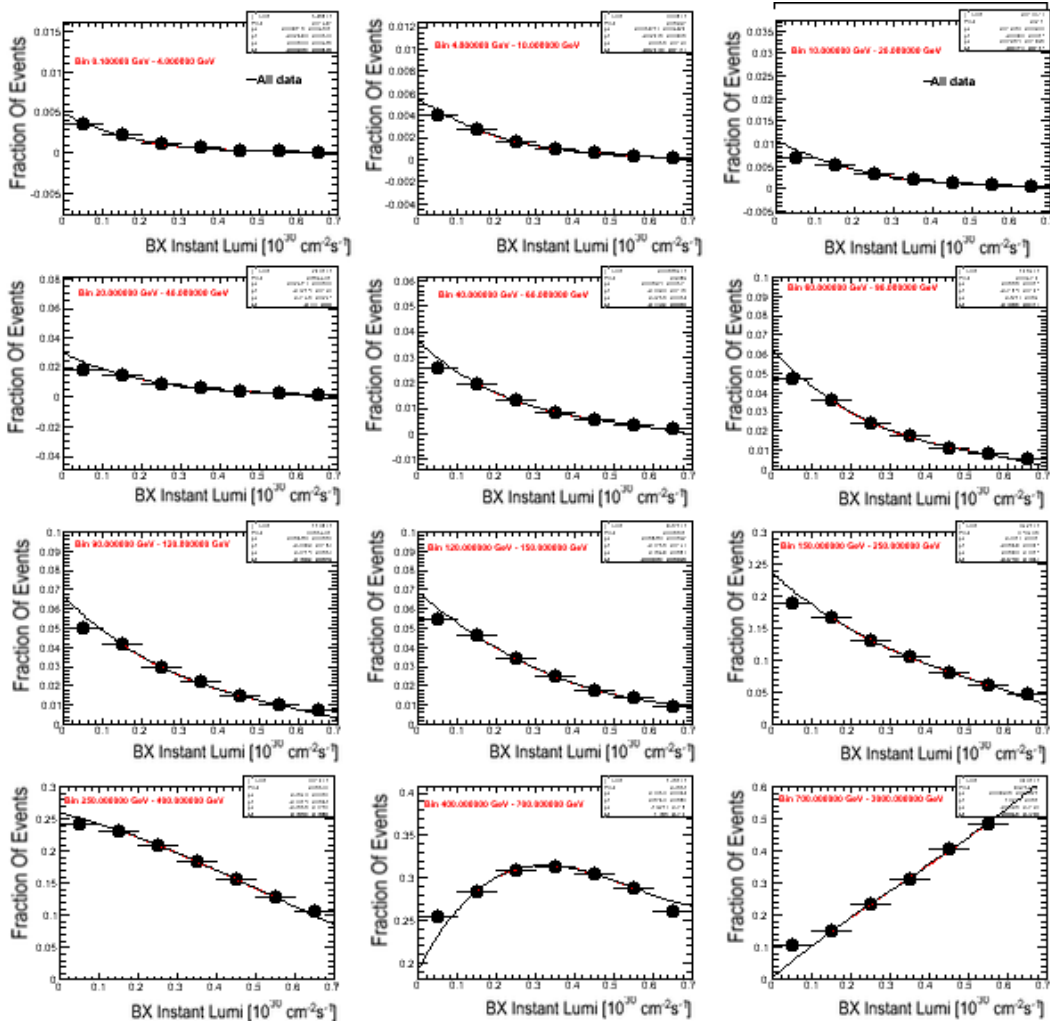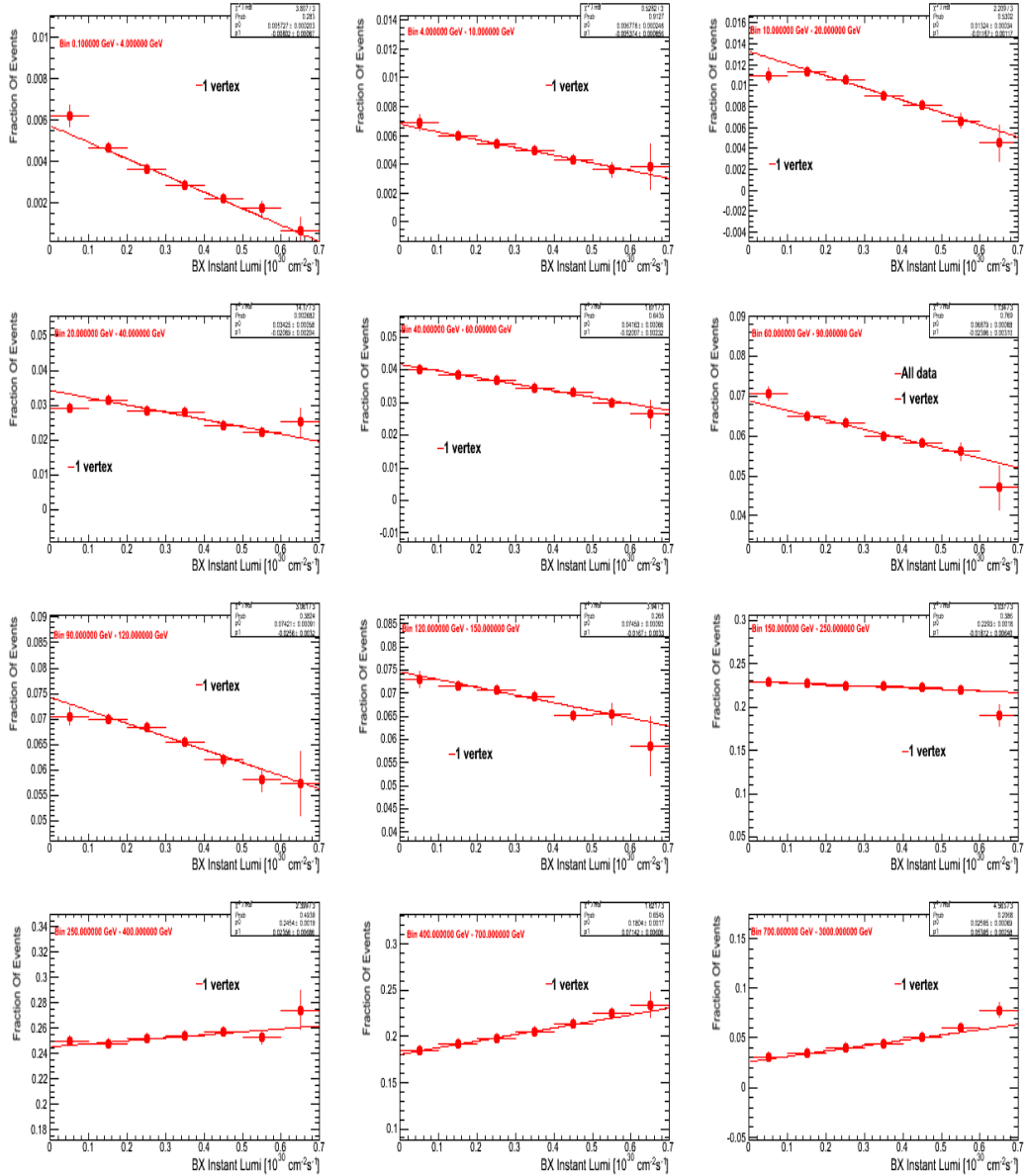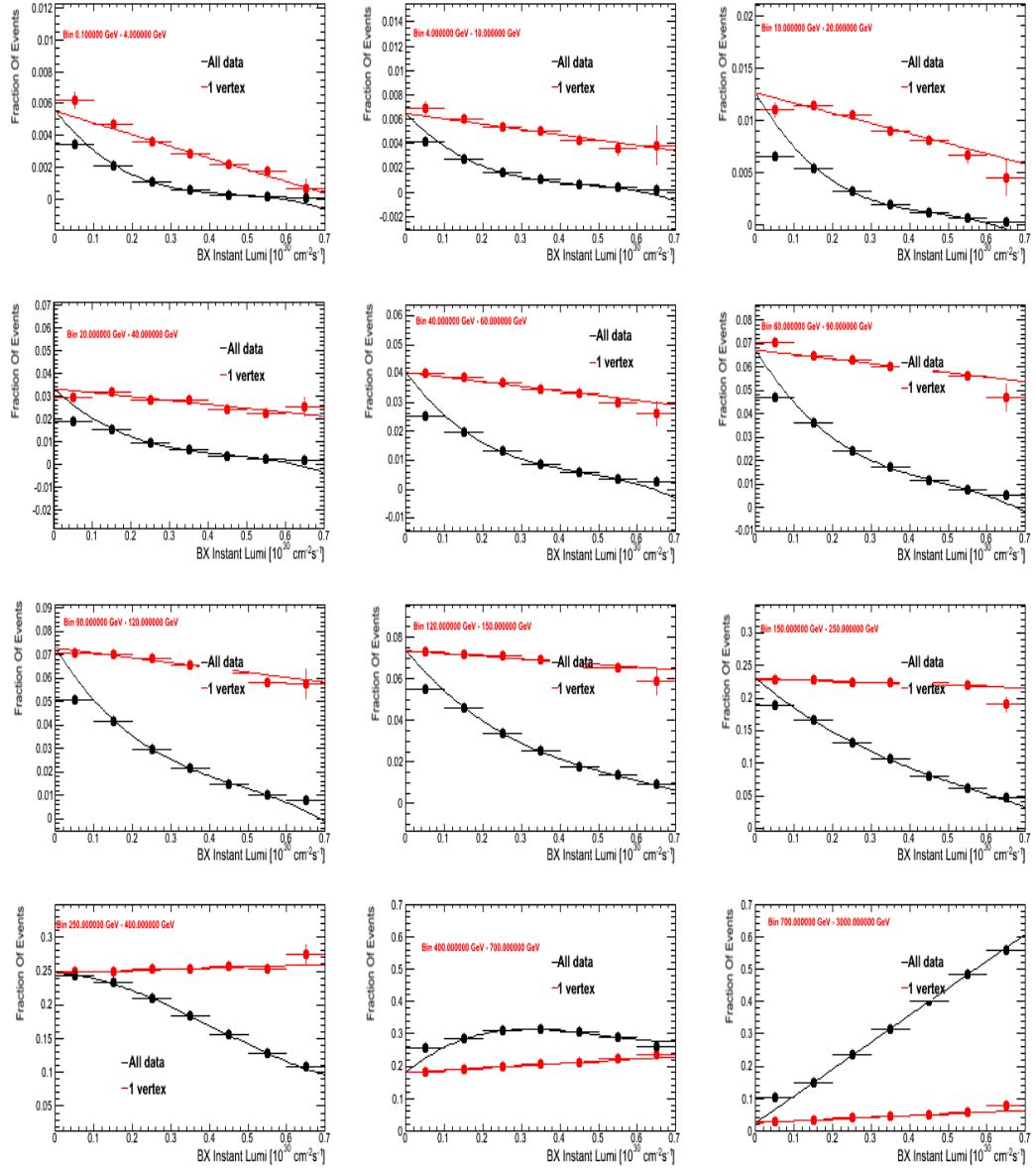
Figure 5.28: *Fraction of events populating different MinHF energy bins as a function of the instantaneous luminosity calculated using the common intercept method. The extrapolation to zero luminosity provides the estimation of the "pile-up" free population of the bin.*

5.6.2 Statistics Uncertainties And Validation of the Unfolding Method

Table 5.13 summarizes the results of the pile-up unfolding of the MinHF variable using the three methods. All intercept values and errors (which are obtained from the fits) are presented.

Energy	unfolding (%)		unfolding one vertex(%)		unfolding combined(%)	
(GeV)	*value*	*error*	*value*	*error*	*value*	*error*
0-4	0.48	0.04	0.57	0.02	0.55	0.02
4-10	0.55	0.04	0.68	0.02	0.65	0.02
10-20	1.06	0.06	1.32	0.03	1.26	0.03
20-40	2.93	0.10	3.43	0.06	3.31	0.05
40-60	3.59	0.12	4.16	0.07	4.04	0.06
60-90	6.18	0.17	6.88	0.08	6.74	0.08
90-120	6.64	0.18	7.42	0.09	7.28	0.08
120-150	6.83	0.19	7.46	0.18	7.35	0.08
150-250	23.50	0.46	22.93	0.55	23.03	0.16
250-400	25.91	0.55	24.54	0.19	24.69	0.18
400-700	19.31	0.64	18.04	0.02	18.10	0.16
700-3000	0.69	0.58	2.56	0.07	2.56	0.07

Table 5.13: *Summary of the intercept values and their errors obtained as described in section 5.6.1 for the three unfolding methods, using the high statistics dataset.*

Every intercept value has the meaning of "fraction of events which would have populated the energy range without the PU contribution". Therefore, the sum of all the intercepts of each of the three methods has to be compatible with "1". The results are:

$$\text{All events} = 0.985 \pm 0.002 \qquad (5.17)$$

$$\text{One vertex events} = 0.996 \pm 0.003 \qquad (5.18)$$

$$\text{Combined} = 1.000 \pm 0.004 \qquad (5.19)$$

Of the three fits, the last one has the best value of the integral and the smaller error. We will therefore use it as our baseline method.

5.6.3   Results

The combined unfolding method presented in section 5.6.1 is then applied
to the Z→ $\mu\mu$ and Z→ee datasets to correct for the pile-up contribution.
The results over the Min HF energy distribution are shown in Fig. 5.29 and
summarized in Table 5.14.

The uncertainties of Table 5.14 are large compared to the intercept values
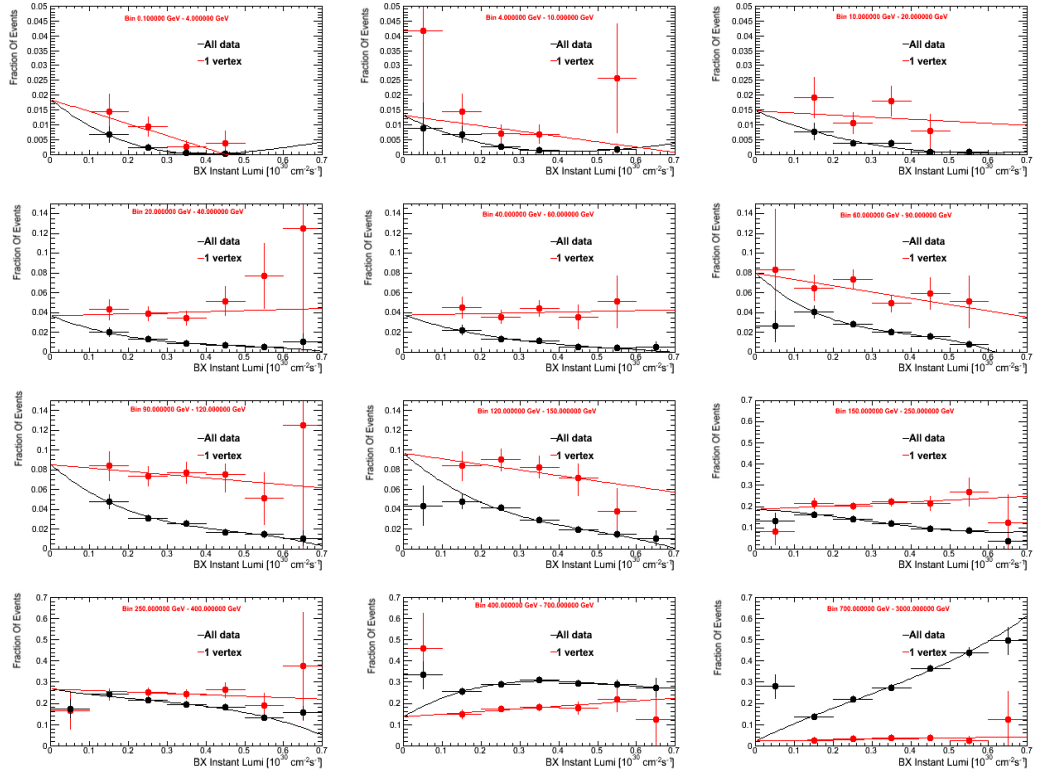
Figure 5.29: *Fraction of events populating different MinEHF energy bins
as a function of the instantaneous luminosity calculated using the Z→ $\mu\mu$,ee
and with the common intercept method. The extrapolation to zero luminosity
provides the estimation of the "pile-up" free population of the bin.*

because of the small size of the Z→ $\mu\mu$,ee dataset. The sum of the intercepts
obtained is:

$$\text{unfolding combined} = 0.997 \pm 0.063 \tag{5.20}$$

The pile-up free distribution of the MinHF variable is presented in Fig. 5.30.

Energy	combined method(%)	
(GeV)	*value*	*error*
0-4	1.85	0.64
4-10	1.32	0.64
10-20	1.47	0.70
20-40	3.68	1.22
40-60	3.75	1.18
60-90	7.99	1.51
90-120	8.52	1.62
120-150	9.66	1.64
150-250	18.69	3.05
250-400	26.79	3.28
400-700	13.70	2.73
700-3000	2.29	1.05

Table 5.14: *Summary of the intercept values and their errors obtained as described in section 5.6.1 for the unfolding combined method, using the Z→ μμ,ee datasets.*

Figure 5.30: *Unfolding of the MinHF energy distribution. The black line represents the uncorrected MinHF energy distribution. The blue points show the distribution without the contribution of the pile-up, as obtained using the unfolding procedure. The events at low HF energy increase as the ones at higher energy decrease.*
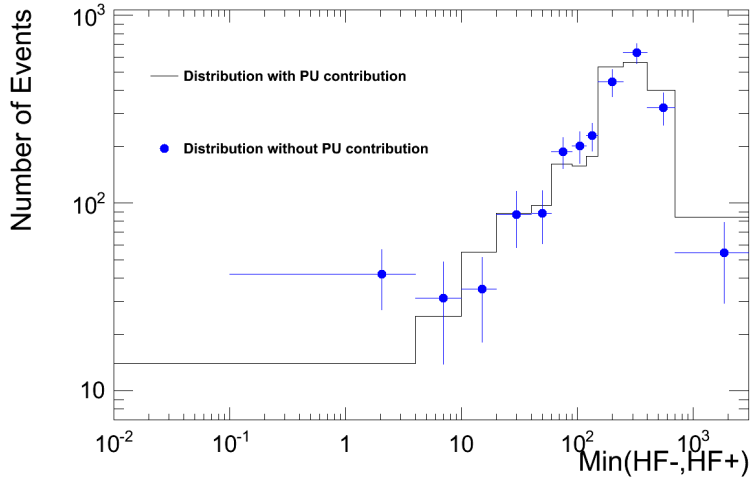
5.6.4   Monte Carlo And Data Comparison

The following variables have been used to check the agreement between Pythia Monte Carlo and data:

1. MinHF.

2. EtaMax.

3. "Etot". Total energy recorded in the detector (Barrel+Endcaps+HF).

4. "TracksMultiplicity". Number of tracks int the event.

5. MaxHF. Maximum energy between the two HF calorimeters

The additional one vertex selection has been applied, both to the data and Monte Carlos. The Monte Carlo data samples have been normalized to the integrated luminosity. The plots are presented for both the Z$\to \mu\mu$ and Z$\to$ee datasets in Figs. 5.31,5.32,5.35,5.33 and 5.34 (the same distributions, without the pile-up removal are presented in the Appendix A).
A further uncertainty has been taken into account (yellow bands): given the low statistics, the uncertainty on the sum of all intercepts is not one. Therefore, an overall normalization error of $\sim 6\%$ is introduced.

5.6.5   Conclusions

Considering the data-Monte Carlo comparisons mentioned above, it is clear that data distributions are not reproduced perfectly by neither Z2 nor D6T MC.
The statistics is still too low: the data points are almost always located between the two Pythia Monte Carlo distributions and their errors are still high. For these reasons, it has not been possible to decide which Monte Carlo tune fits the control distributions at best. We will use both the two Pythia tunes in the measurement of the cross section.

Figure 5.31: *MinHF energy distribution, corrected to remove the pile up contribution. Black points represent the data. Normalized at the same integrated luminosity, the Pythia D6T(continuous line),Z2 (line with big dash) have been superimposed. The plot is done by gathering the Z→ μμ and ee statistics.*
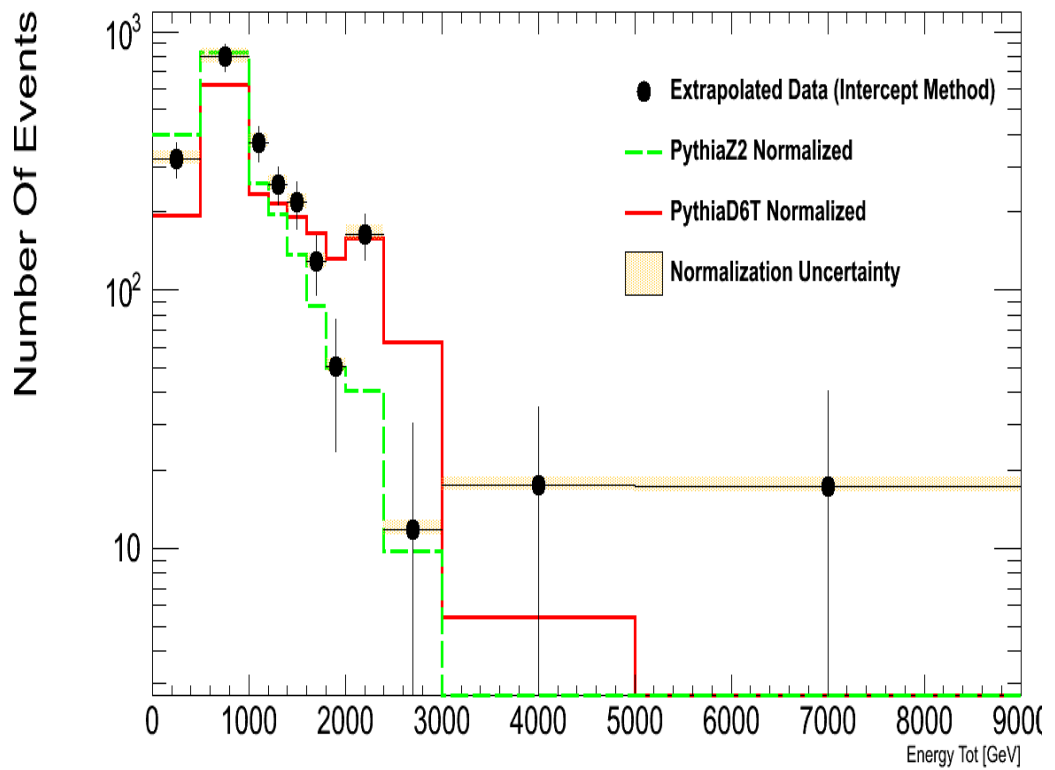
Figure 5.32: *Detector total Energy distribution, corrected to remove the pile up contribution. Black points represent the data. Normalized at the same integrated luminosity, the Pythia D6T(continuous line),Z2 (line with big dash) have been superimposed. The plot is done by gathering the $Z \rightarrow \mu\mu$ and ee statistics.*
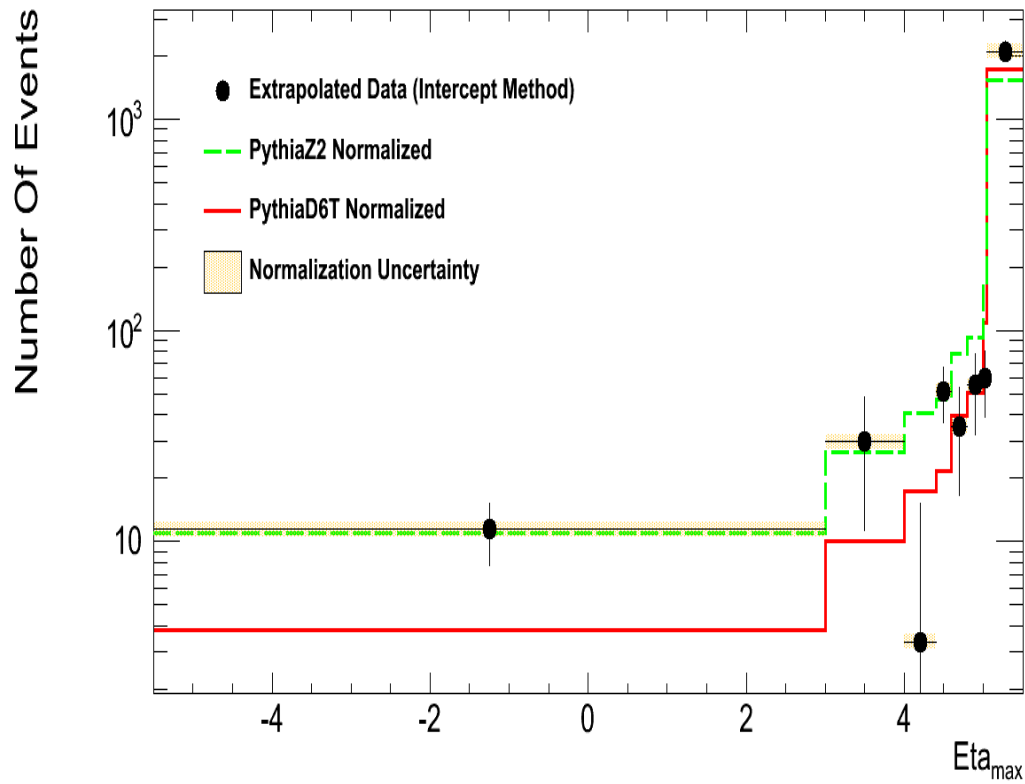
Figure 5.33: *Eta Max distribution, corrected to remove the pile up contribution. Black points represent the data. Normalized at the same integrated luminosity, the Pythia D6T(continuous line),Z2 (line with big dash) have been superimposed. The plot is done by gathering the $Z \to \mu\mu$ and ee statistics.*
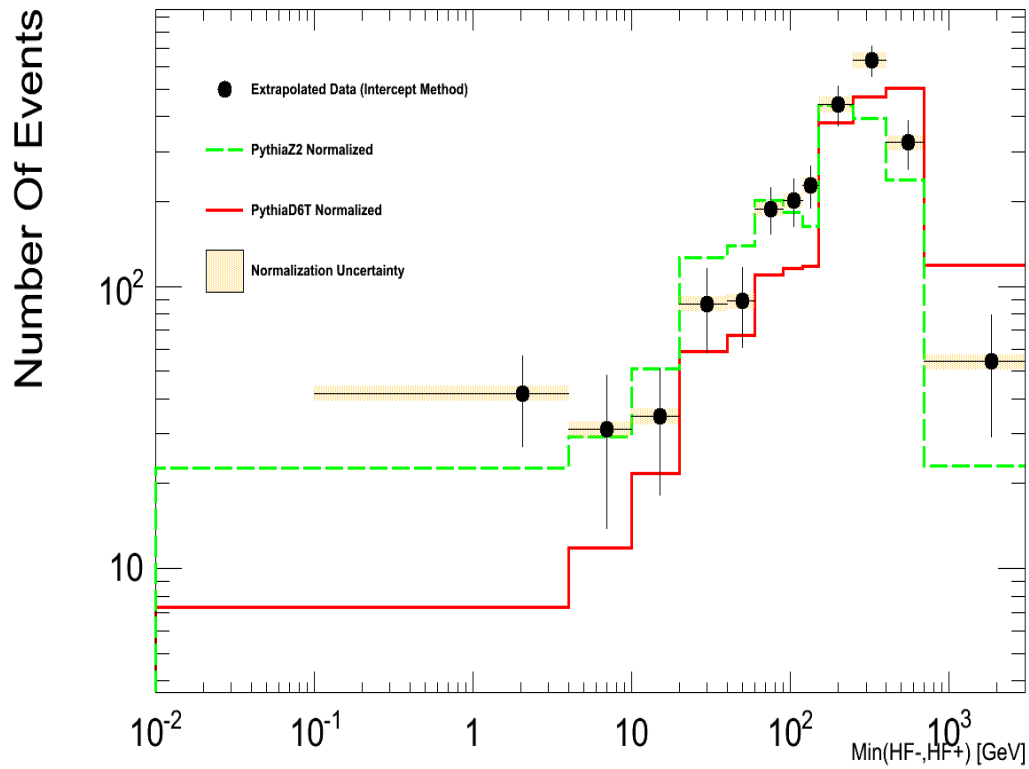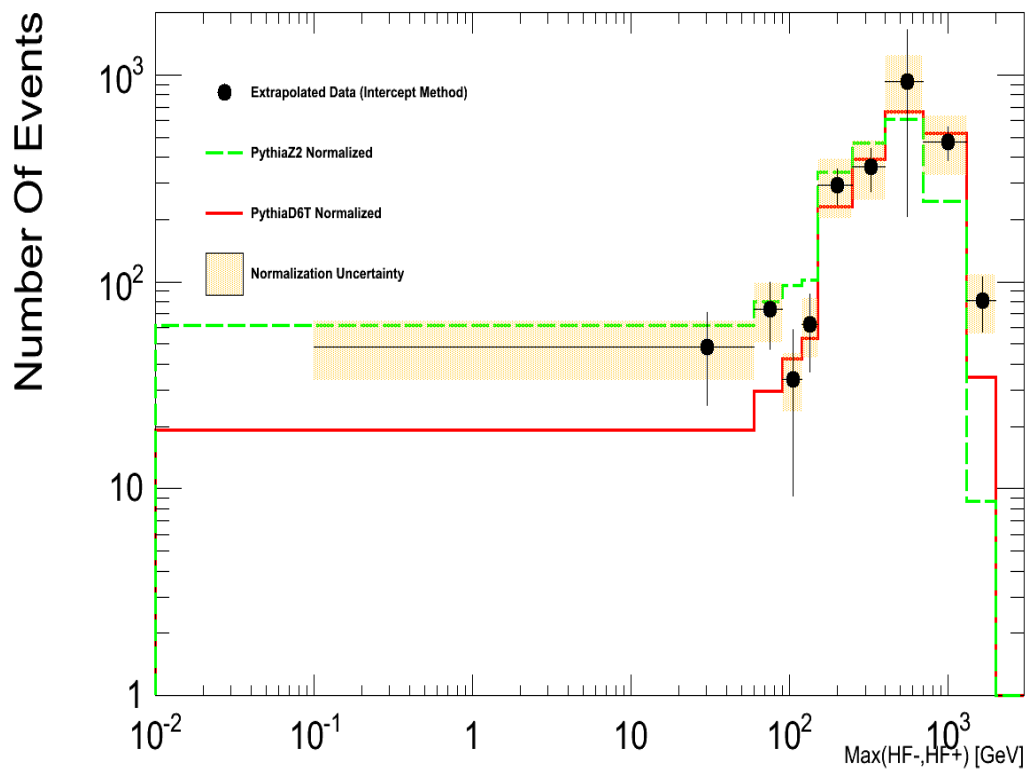
Figure 5.34: *MaxHF energy distribution, corrected to remove the pile up contribution. Black points represent the data. Normalized at the same integrated luminosity, the Pythia D6T(continuous line),Z2 (line with big dash) have been superimposed. The plot is done by gathering the $Z \to \mu\mu$ and ee statistics.*

Figure 5.35: *TracksMultiplicity distribution, corrected to remove the pile up contribution. Black points represent the data value. Normalized at the same integrated luminosity, the Pythia D6T(continuous line),Z2 (line with big dash) have been superimposed. The plot is done by gathering the $Z \to \mu\mu$ and ee statistics.*
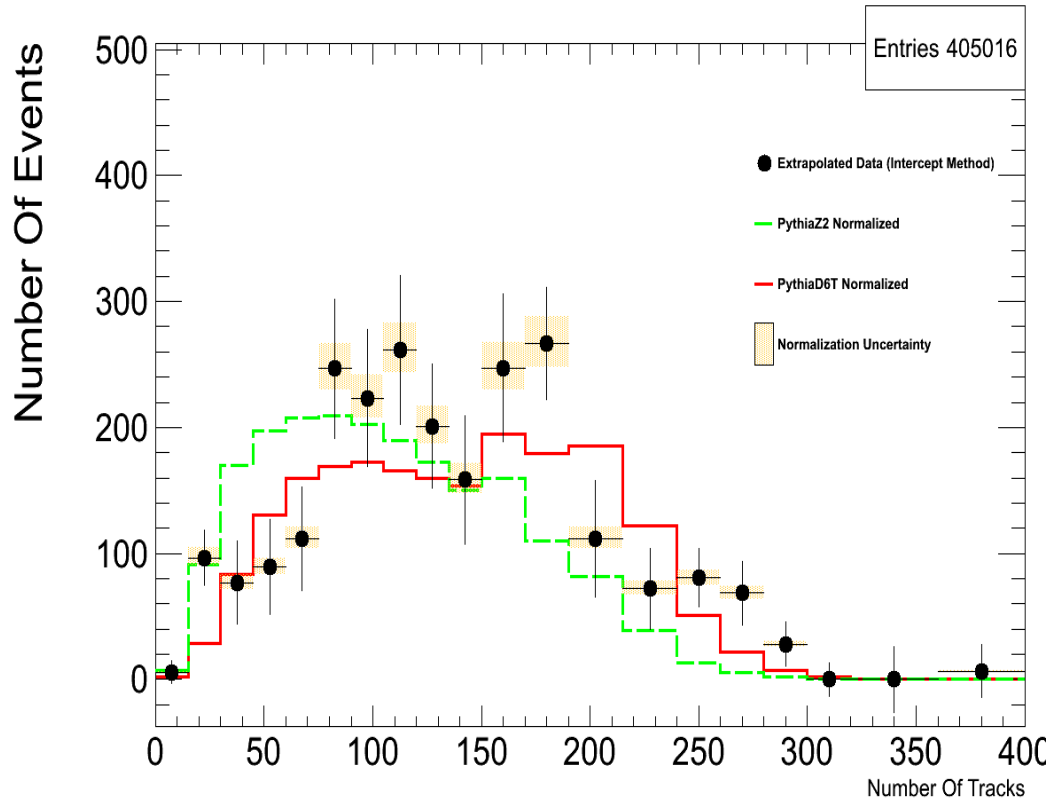
5.7   Cross Section Measurement And Results

In this section a measurement of the Z$\to$ ee and Z$\to$ $\mu\mu$ diffractive cross section is presented.
Events have been selected requiring:

- energy below a minimum threshold (see section 5.3.1) in HF- or HF+ calorimeters (sumHF=0)

- only one vertex with quality NDOF $\geq$ 4, to avoid reconstruction of fake vertices

- value of ζ within $0 \leq \zeta \leq 0.03$

Diffractive Pompyt and Pythia MC have been used to predict the cross section for $0 \leq \zeta \leq 0.03$. The results are presented in Table 5.15.

Bin	PomPyt (pb)	Pythia D6T (pb)	Pythia Z2 (pb)
0-0.015	61.8±1.1	10.2±0.2	24.5±0.3
0.015-0.030	24.9±0.7	31.4±0.4	81.3±0.5
Total	**86.7±1.3**	**41.6±0.4**	**105.8±0.6**

Table 5.15: *Predicted cross section using Pompyt and Pythia Monte Carlos for 0 ≤ ζ ≤ 0.03.*

Figure 5.36 shows the number of Monte Carlo (normalized to the data integrated luminosity) and data events which pass the above selection as a function of ζ, for both the electrons (upper plot) and muons (bottom plot) Z decay modes. The black dots represent the data points, while the Monte Carlo Pythia Z2 (coarse dashed line), Pythia D6T (continuous line) and PomPyt (fine dashed line) are shown together with the dissociative diffractive events (dot-dashed line). The data have been reweighted (see section 5.4.3) to account for the loss of efficiency due to the pile-up.
 Figure 5.36 clearly demonstrates:

- the different behavior of the two Pythia tunes. D6T has less events after the diffractive selection.

- the number of diffractive PomPyt events which pass the diffractive selection cuts is very large compared to data. The total cross section used to generate the PomPyt Monte Carlo (210.5 pb) is then too high.
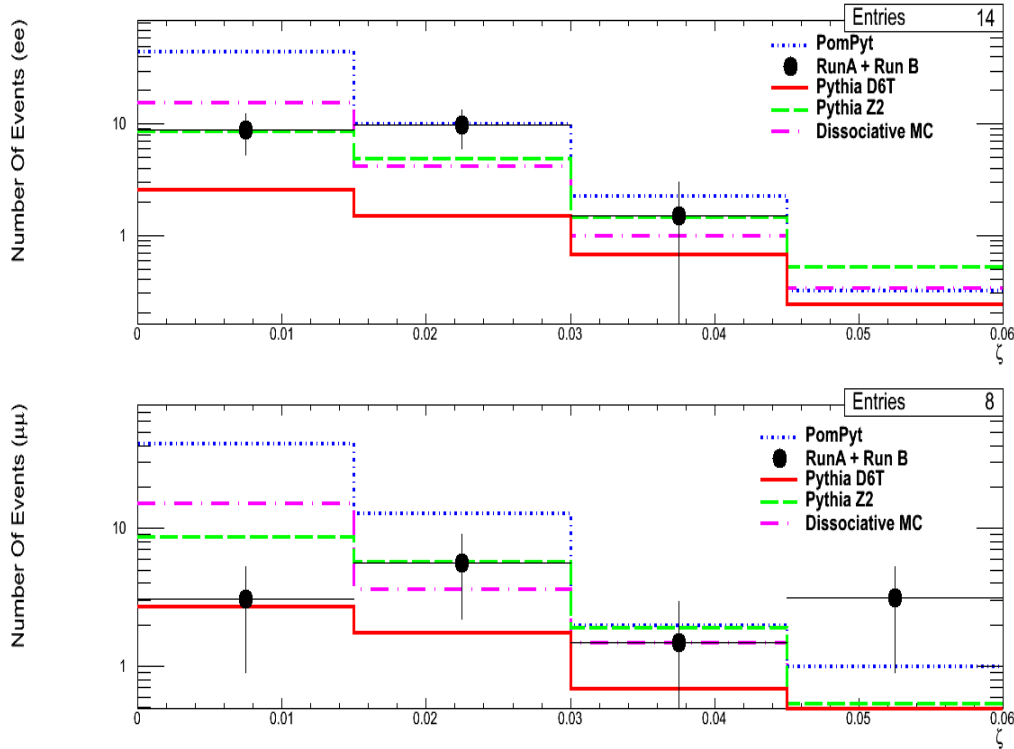
Figure 5.36: *Number of events which pass the diffractive selection as a function of ζ, for both the electrons (upper plot) and muons (bottom plot) Z decay modes: the PomPyt MonteCarlo Diffractive and Dissociative,Pythia D6T and Z2 are presented together with the data collected during 2010.*

- the contribution of the diffractive dissociative part is roughly a third of the diffractive PomPyt

- The number of selected data events is small, especially if compared to the Z2 tune prediction.

Table 5.16 shows the diffractive selection efficiency (number of events per pb of cross section) for the various Z→ee datasets. It is evident that:

1. the selection cuts reject the majority of Pythia Monte Carlo events

2. the number of selected events from Pythia Z2 sample is higher compared to D6T tune. This is due to the combination of two factors: a lower rejection power (due to a larger number of simulated gaps then D6T) and a higher number of events predicted at low ζ.
   Fig. 5.37 shows the generated ζ distribution for the two Pythia Monte

Range	PomPyt		PythiaD6T		Pythia Z2	
	Sel.Events	$\frac{Events}{\sigma_{bin}}$	Sel.Events	$\frac{Events}{\sigma_{bin}}$	Sel.Events	$\frac{Events}{\sigma_{bin}}$
0-0.015	44.6	**0.77**	2.5	**0.25**	8.6	**0.37**
0.015-0.03	10.2	**0.44**	1.5	**0.05**	4.8	**0.06**

Table 5.16: *Diffractive selection efficiencies. The ratio between the number of selected events and the predicted cross section ($\frac{Events}{\sigma_{bin}}$) in each bin is presented. All samples have been normalized to 7.5 pb^{-1}*
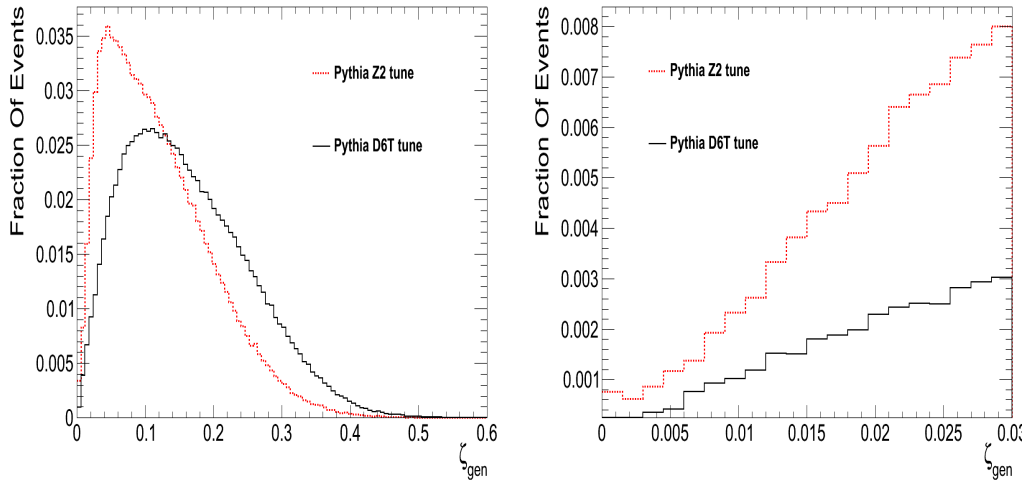

Figure 5.37: *Distribution of the ζ_{gen} variable for the two Pythia Monte Carlos. On the left plot, the dashed line represents the Z2 tune distribution while the black continuous line the D6T tune. On the right the same plot, zoomed on the kinematic region of interest.*

Carlos (no cuts have been applied). A larger fraction of Z2 events has very small ζ values. A zoomed view of the range used in this analysis is shown on the right.

5.7.1   Statistical Significance Of The Null Hypothesis

In this section we have evaluated the statistical *significance S* of the measured events with respect of the null hypothesis, i.e. we evaluate the probability that the measured events are due only to non diffractive events. We define

S as:

$$S = \frac{N_{evts} - N_{bkg}}{\sqrt{\sigma_{evts}{}^2 + \sigma_{bkg}{}^2}} \tag{5.21}$$

where σ_{bkg} is $\sqrt{N_{bkg}}$ while the σ_{evts} are the weighted errors obtained before (see Fig. 5.16). The Z→ee and $\mu\mu$ data samples have been summed together to increase statistics. In Table 5.17, the significance of each bin is presented. If we assume D6T to be the correct background description, then we would

Range	D6T Background(σ_{D6T})	Z2 Background(σ_{Z2})
0-0.015	1.38	-0.89
0.015-0.030	2.26	0.38
Total	**2.62**	**-0.07**

Table 5.17: *The significance of the selected Z→ $\mu\mu$,ee diffractive events. The significance has been obtained using the two MCs separately.*

have a significance of about 2.6 σ. Considering the Z2 tune, this value drops down to ~ 0 σ. With the available data, it is not possible to evaluate the presence of a signal using Z2 tune as background.

Fig. 5.38 shows the signal significance as a function of the (effective) integrated luminosity if the background is modeled by D6T. To assess at 3 σ the presence of a signal, we would need ~ 11 pb^{-1}. The 5 σ signal is instead assessed with ~ 29 pb^{-1}. Unfortunately, the luminosity for events without visible pile-up collected during the 2010 run is only 7.5 pb^{-1}.

5.7.2 Measurement Of The Cross Section For Diffractive Z Production

The cross section is derived in the following way:

$$\sigma_{0 \leq \zeta \leq 0.03} = \frac{N_{events} - N_{bkg}}{A \cdot \mathscr{L} \cdot \epsilon_Z \cdot \epsilon_D} \tag{5.22}$$

where A is the acceptance, $\mathscr{L}$ the (effective) integrated luminosity, ϵ_Z the efficiency of the Z boson selections (as calculated in section 5.2) and ϵ_D the efficiency of the diffractive selection (as shown in Table. 5.17). The results are summarized in Table.5.18.
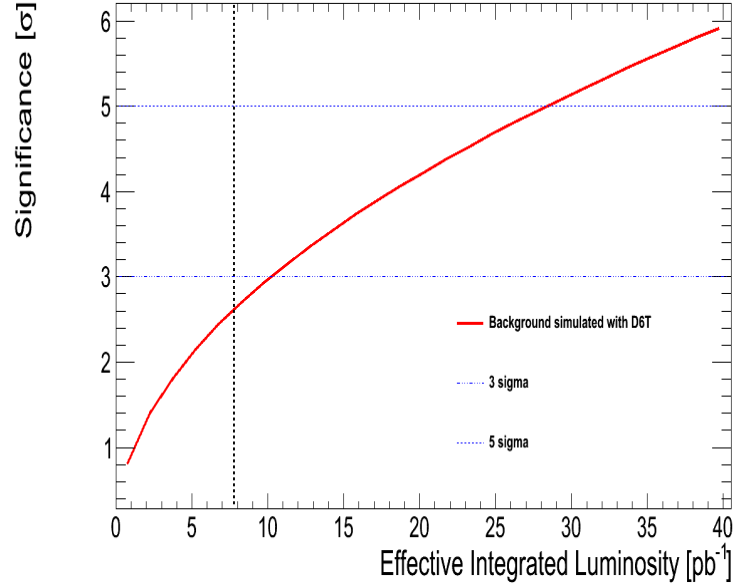
Figure 5.38: *The (one vertex) integrated luminosity needed to have a significance of 3 or 5 σ, for the D6T Monte Carlo tune. The dashed vertical line indicates the integrated luminosity of our data samples.*

Montecarlo	Z$\rightarrow$ee (pb)	Z$\rightarrow \mu\mu$ (pb)	combined (pb)
Pythia D6T	33$\pm$12	9$\pm$8	**42$\pm$15**
Pythia Z2	14$\pm$12	-9$\pm$8	**5$\pm$15**

Table 5.18: *Summary of the measured cross sections considering two different Pythia Monte Carlos as background.*

5.7.3   Results

The estimation of the Z$\rightarrow \mu\mu$,ee cross section in the kinematic range $0\leq \zeta \leq 0.03$ depends on which Pythia tune is considered as background. Using the Z2 tune, no signal is assessed. Using the D6T tune, the cross section is measured to be **(42$\pm$15)** pb, with a statistical significance of 2.6 σ.
To assess at (3) 5 σ the presence of a signal using the D6T tune, we would need $\sim$ (11) 29 pb^{-1} of effective integrated luminosity.

5.8 Studies on Different Diffractive Event Selections

Besides sumHF=0, two other alternative cuts to select diffractive events have been studied:

EtaMax $\leq$ 2.85 : this request implies to have no energy (below a minimum threshold, see 5.3.1) deposited in the HF calorimeter and in the outer rings of the HE.

sumHF=0 and CASTOR=0 : the energy in HF and CASTOR calorimeters is requested to be zero (below a minimum threshold, see 5.3.1)

5.8.1 Selection Using EtaMax $\leq$ 2.85

The event selection relies on the measurement of two subdetector parts at the same time. The larger gap size (2.15 units instead of 2) helps in the rejection of gaps created in non diffractive events but implies a lower signal selection efficiency (if compared to sumHF=0). According to Fig. 5.4, it decreases from 9.6% to 7.5%.
The measurement of the cross section (see Table 5.19) has been obtained from Fig. 5.39, in which the number of events having $\eta_{max} \leq$2.85 is presented.

Montecarlo	Z→ee (pb)	Z→ $\mu\mu$ (pb)	combined (pb)
Pythia D6T	18±9	0±3	**18±10**
Pythia Z2	9±9	-9±3	**0±10**

Table 5.19: *Summary of the measured cross sections obtained using the diffractive selection $\eta_{Max} \leq$2.85.*

The comparison between sumHF=0 and η_{max} <2.85 cross sections has been used to estimate the dependency of the selection on the η_{max} parameter (using D6T as background). The $\sigma_{\zeta \leq 0.03}(Z \to \mu\mu, ee)$ becomes:

$$\sigma_{\zeta \leq 0.03}(Z \to \mu\mu, ee) = 42 \pm 15(\text{Stat}) \pm 24 \text{ (Syst) pb} \qquad (5.23)$$

5.8.2 Diffractive Selection With CASTOR Calorimeter.

The request of no energy in both CASTOR (-6.6$\leq \eta \leq$-5.2) and HF calorimeters corresponds to a gap of $\sim$ 3.5 units, which makes this selection virtually
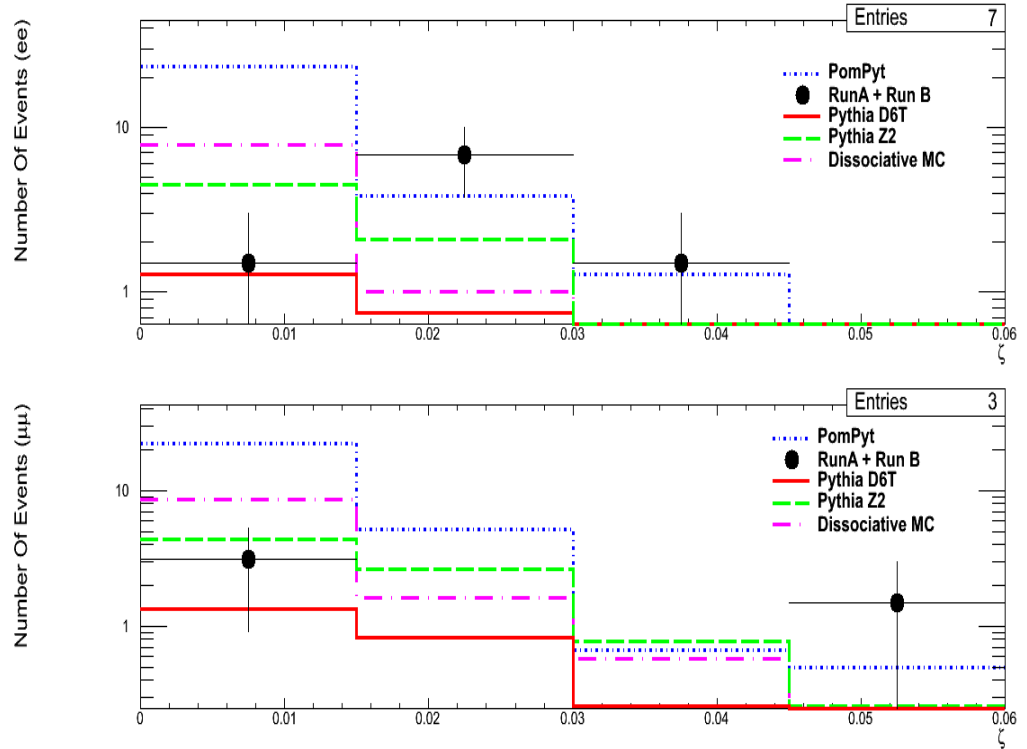
Figure 5.39: *Number of events which pass the diffractive selection $\eta \leq 2.85$ as a function of ζ, for both the electrons (upper plot) and muons (bottom plot) Z decay modes: the PomPyt MonteCarlo Diffractive and Dissociative,Pythia D6T and Z2 are presented together with the data collected during 2010.*

background-free, as it is shown in Table. 5.20.

While the background events are decreased by a factor of 10, the signal efficiency is only 20% less than sumHF=0. These numbers make this cut very suitable for the signal selection.

Unfortunately, the CMS detector has been equipped with only one CASTOR calorimeter: only the diffractive events produced in the -z direction are detected by CASTOR.

In Fig. 5.40, the number of events which pass this selection is presented. As it is clearly visible in figure, the expected background is very small, for both the Pythia D6T and Z2 tunes.

In Table 5.21, the cross section of the selected events is presented.

Considering the recorded data, the signal is not assessed. Unfortunately, CASTOR calorimeter has suffered of intermittent calibration problem during 2010. Even if it were operational, the data recorded during these periods

	PomPyt (%)	Pythia D6T (%)	Pythia Z2 (%)
sumHF=0	9.6	0.2	0.5
sumHF=0 and Castor	8.0	$2.0 \cdot 10^{-2}$	$6.1 \cdot 10^{-2}$

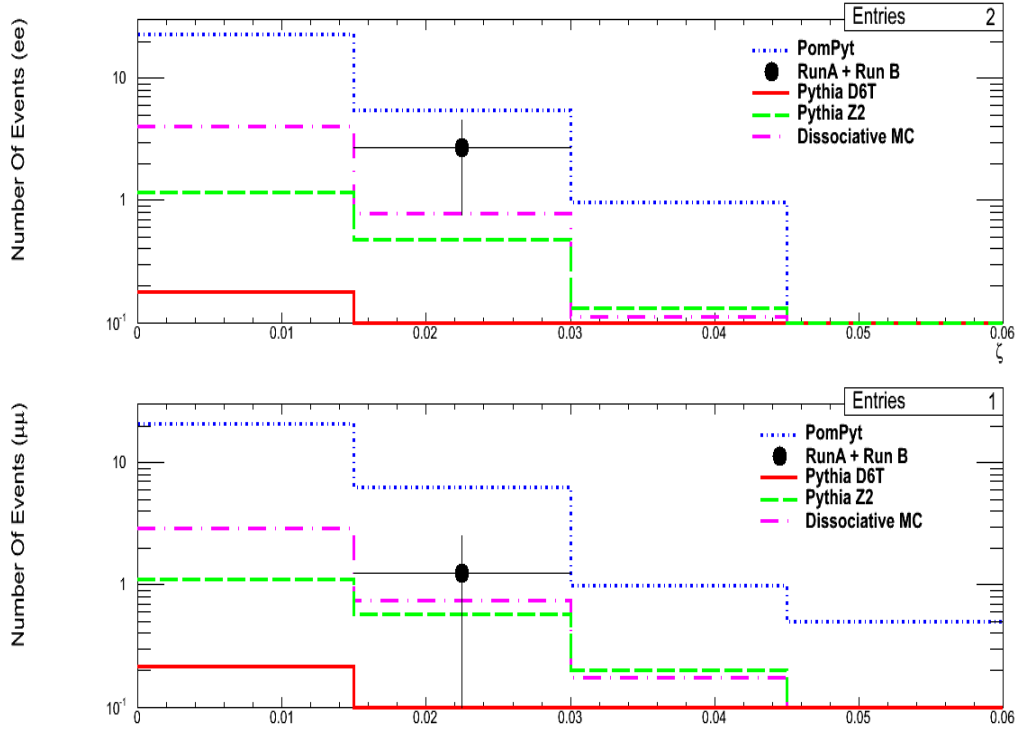**Table 5.20:** *Fraction of background and MC signal events which pass the "HF and CASTOR =0 selection".*

Figure 5.40: *Number of events which pass the diffractive selection HF and Castor energy equal to zero as a function of ζ, for both the electrons (upper plot) and muons (bottom plot) dataset: the PomPyt MonteCarlo Diffractive and Dissociative,Pythia D6T and Z2 are presented together with the data collected during 2010.*

were not fully certified for the analysis and thus eliminated. Nevertheless, precise study shows the possibility to use this cut to obtain a cross section measurement at higher luminosity.

Montecarlo	Z→ee (pb)	Z→ $\mu\mu$ (pb)	combined (pb)
Pythia D6T	7±5	3±4	**10±6**
Pythia Z2	5±5	0±4	**5±6**

Table 5.21: *Summary of the measured cross sections obtained using the diffractive selection sumHF and Castor=0*

Conclusions

The study of hard diffraction at LHC will explore and test the ideas and models developed at DESY and Fermilab at much lower energies. However, the very large number of pile-up events in a typical LHC event poses new challenges to the selection of diffractive events and the past methods based on the presence of a rapidity gap are not applicable. Furthermore, any topological cut such those based on rapidity gaps, needs to be validated by detailed studies of forward energy flow at the new LHC energy regime.

In this thesis we have proposed and employed a novel method to select diffractive events. The first request of our selection, use only events without visible pile-up events, exploits the characteristics of the first months of LHC running, when the instantaneous luminosity per bunch was quite low, 0.1-0.5 $10^{30} \cdot cm^{-2}s^{-1}$, and the number of interactions per bunch crossing was around 2-3. Secondly, we have derived a weight function that weights diffractive events on the probability of having a rapidity gap at a given luminosity: in so doing we were able to use the luminosity of the complete running period. The third requests of the method, a value of ζ less than $3 \cdot 10^{-2}$, further enhance the number of diffractive events in the final sample.

The extraction of the diffractive signal from the events that pass our selection criteria is further complicated by the current discrepancy between data and Monte Carlo in the description of the energy flow in the forward region. This mismatch, which is actually quite important, did not allow us to choose one single Monte Carlo model for the description of the non diffractive part but has forced us to use two Pythia tunes, D6T and Z2, which bracket the range of uncertainties.
Within these constrains, and due to the quite low luminosity, we were not able to establish the presence of diffractive Z production, but only to see a production excess over one of the two Pythia tunes prediction.

We are confident that the tools developed for this analysis can be applied to

the much larger sample of the 2011 data, and we are looking forward to do
the analysis in the next few months.

Acknowledgments

Ringraziamenti

Infine, a chiudere il cerchio, voglio fare una dedica speciale a Luisa. Lei è infatti legata più di tutti a questa tesi di dottorato. A lei devo la scrittura del Capitolo 0 della mia tesi: quel capitolo che non è mai scritto in nessun libro, ma che è fondamentale in ogni traguardo e in ogni successo. Un capitolo in cui le parole sono il supporto, le figure il conforto e le formule l'aiuto e la spinta per inseguire un sogno. Mancherebbero poi tanti altri piccoli particolari, dettagli e sottogliezze che sono impossibili da sintetizzare in una parola, ma prendono forma e sostanza quando tu sei accanto a me, e mi sostieni, proprio come hai fatto durante questo periodo.

Appendix A

Comparison Data-Monte Carlo For Distribution Without Pile-up Correction

The following plots present the comparison between data and Monte Carlo datasets. The D6T (continuous line), Z2 (coarse dashed line) and PomPyt (fine dashed line) Monte Carlo are compared to the data points (black points), without the pile-up removal.

Figure A.1: *Control Distribution: Min(HF-,HF+). Black points represent the data value. Normalized at the same integrated luminosity, the Pythia D6T (continuous line), Z2 (coarse dashed line) and PomPyt (fine dashed line) have been superimposed. The upper plot is done using the Z→ee dataset, while the bottom one with Z→ μμ. The pile-up contribution has not been removed.*

Figure A.2: *Control Distribution: EtaMax. Black points represent the data value. Normalized at the same integrated luminosity, the Pythia D6T(continuous line),Z2 (line with big dash) and PomPyt (line with small dash) have been superimposed. The upper plot is done using the Z→ee dataset, while the bottom one with Z→ μμ. The pile-up contribution has not been removed.*

Figure A.3: *Control Distribution: Etot. Black points represent the data value. Normalized at the same integrated luminosity, the Pythia D6T(continuous line),Z2 (line with big dash) and PomPyt (line with small dash) have been superimposed. The upper plot is done using the Z→ee dataset, while the bottom one with Z→ μμ. The pile-up contribution has not been removed.*

Figure A.4: *Control Distribution: TracksMultiplicity. Black points represent the data value. Normalized at the same integrated luminosity, the Pythia D6T(continuous line),Z2 (line with big dash) and PomPyt (line with small dash) have been superimposed. The upper plot is done using the Z→ee dataset, while the bottom one with Z→ μμ. The pile-up contribution has not been removed.*
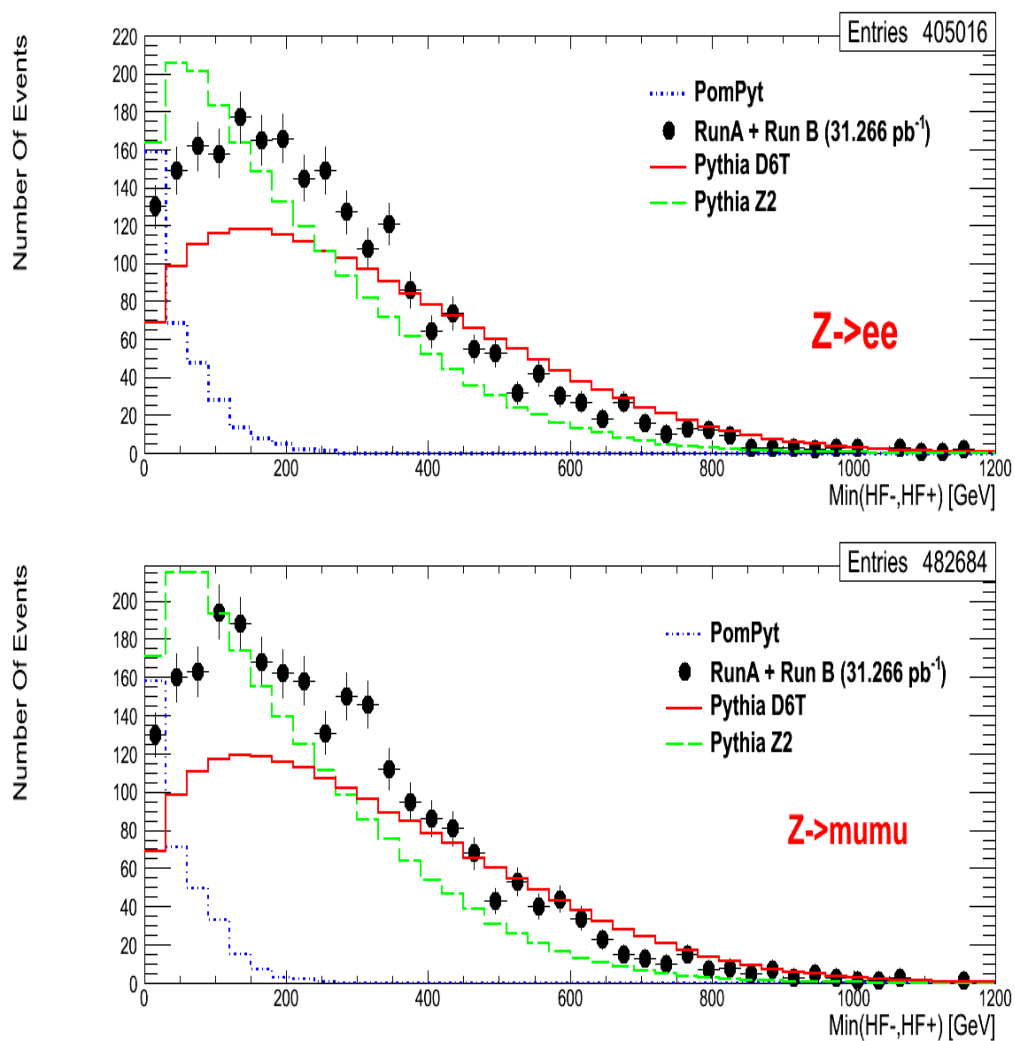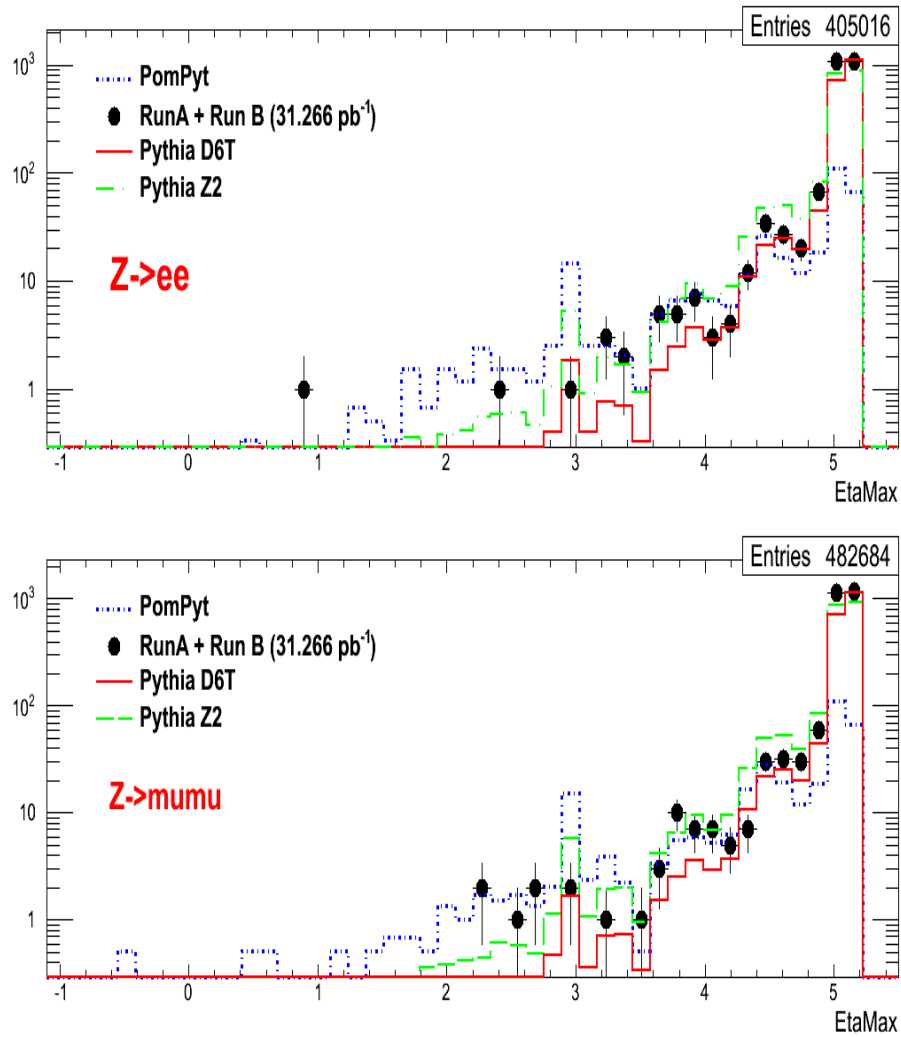
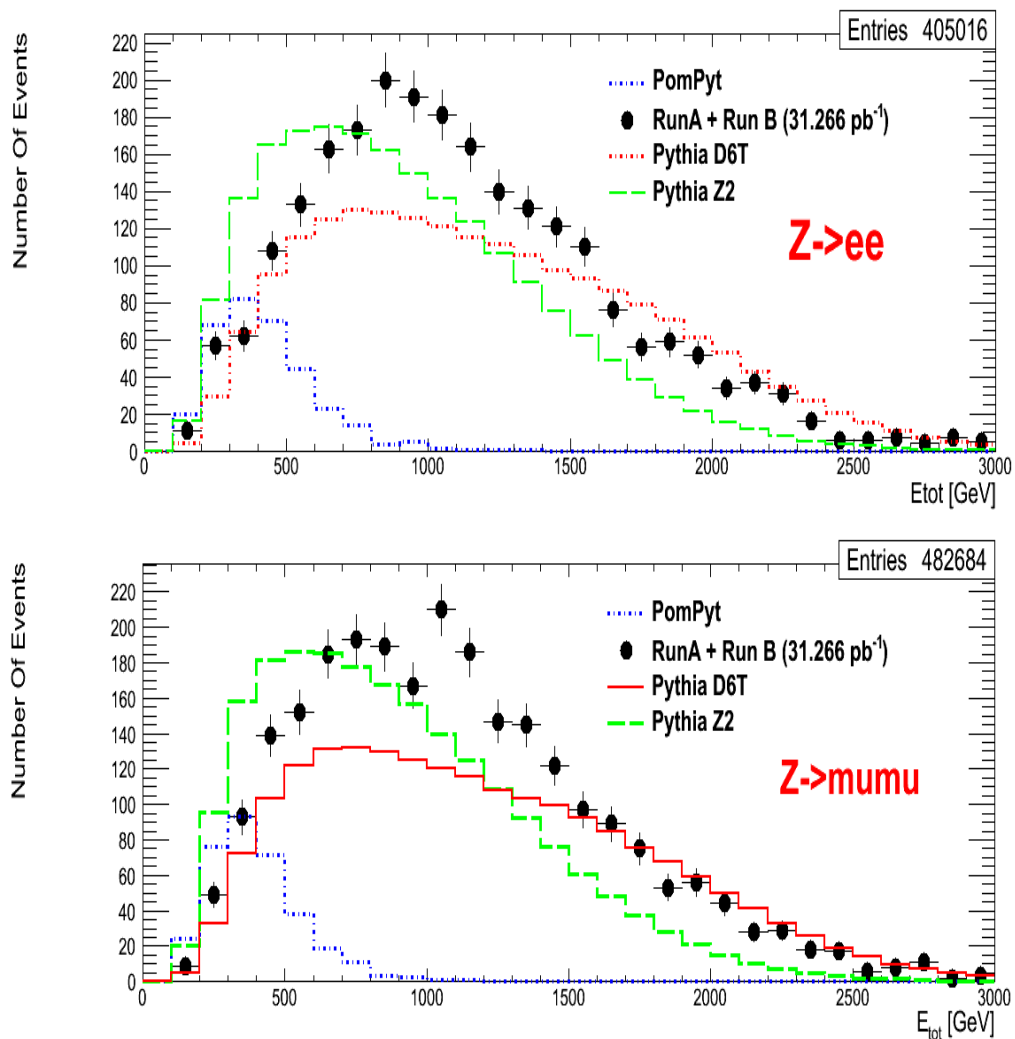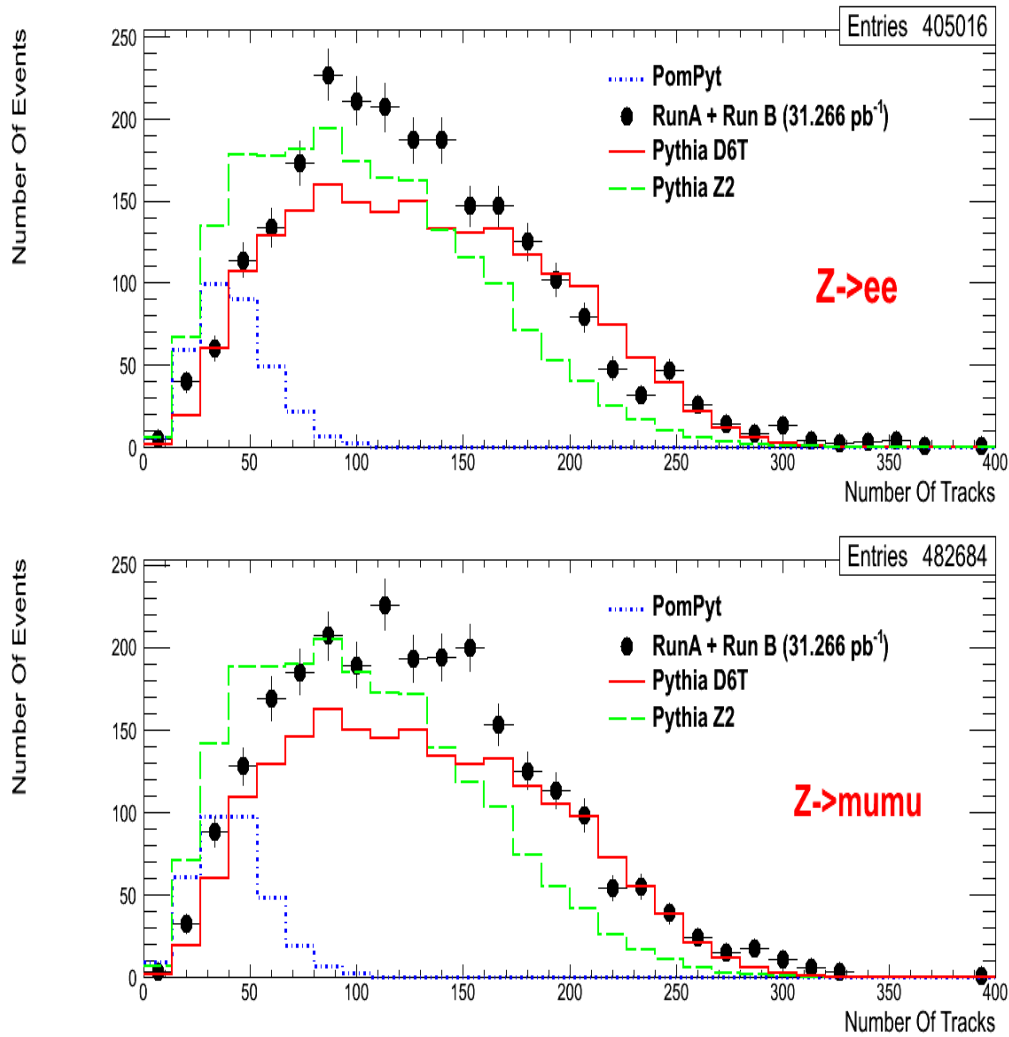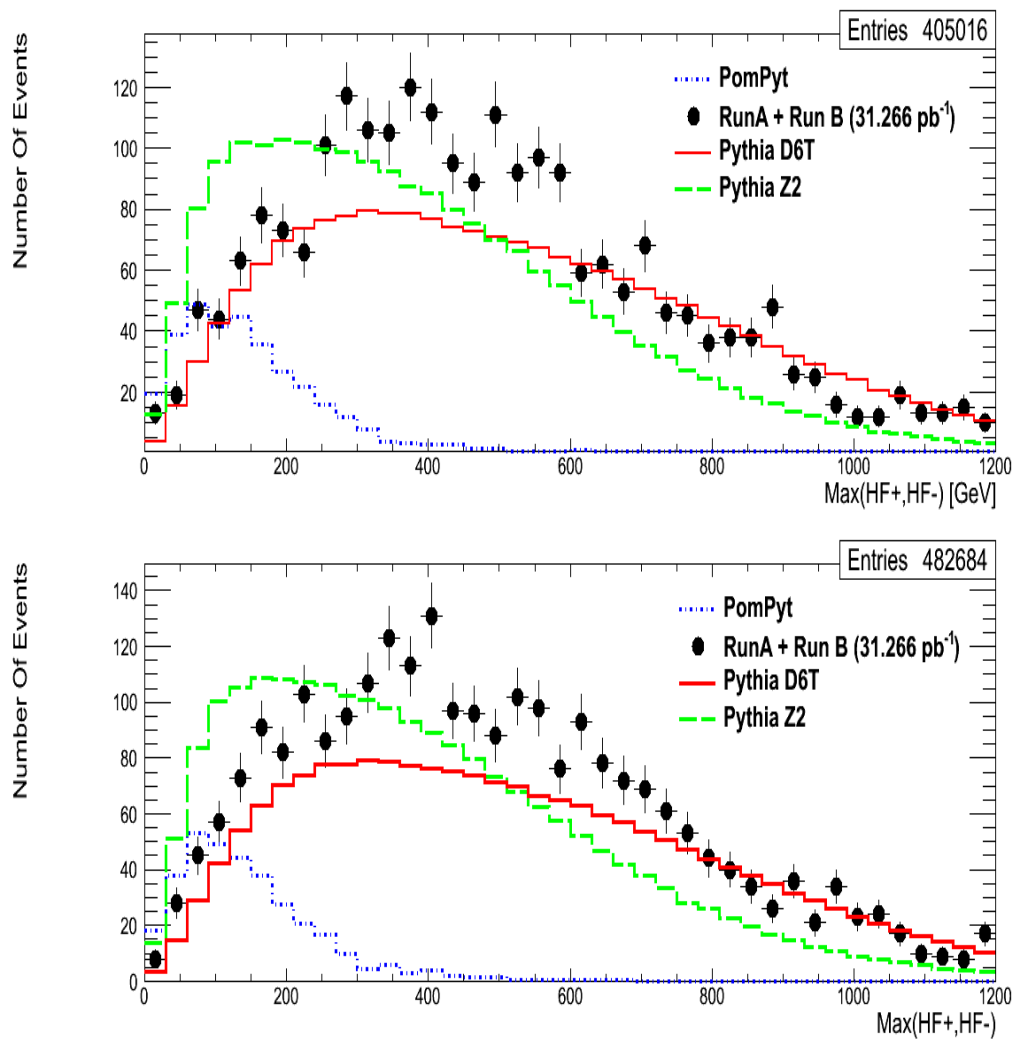**Figure A.5:** *Control Distribution: HFMax. Black points represent the data value. Normalized at the same integrated luminosity, the Pythia D6T(continuous line),Z2 (line with big dash) and PomPyt (line with small dash) have been superimposed. The upper plot is done using the Z→ee dataset, while the bottom one with Z→ μμ. The pile-up contribution has not been removed.*

Bibliography

[1] The LHC Study Group, *The Large Hadron Collider Conceptual Design*, CERN/AC 95-05 (1995).

[2] T. Sjostrand, S. Mrenna and P. Skands, *PYTHIA 6.4 physics and manual*, JHEP 05 (2006) 026. hep-ph/0603175.

[3] S. Beole et al., *ALICE technical design report: Detector for high momentum PID*, CERN-LHCC-98-19.

[4] The LHCb Collaboration, *LHCb technical design report: Reoptimized detector design and performance*, CERN-LHCC-2003-030.

[5] W. W. Armstrong et al., *ATLAS: Technical proposal for a general-purpose p p experiment at the Large Hadron Collider at CERN*, CERN-LHCC-94-43.

[6] The CMS Collaboration, *CMS, the Compact Muon Solenoid: Technical proposal*, CERN-LHCC-94-38.

[7] A. D. Martin et al. *Uncertainties of predictions from parton distributions I: Experimental errors*, Eur. Phys. J. C 28 pg.455 (2003).

[8] H. T. Haber et al. *The search for Supersimmetry: probing physics beyond the Standard Model*, Physics Report 117, pg.75 (1985).

[9] P.D.B. Collins, *An introduction to Regge Theory and High-Energy Physics*, Cambridge (1977).

[10] V.Barone and E.Predazzi, *High-energy particle diffraction*, Springer (2002).

[11] R. Bonino et al., *Evidence for Transverse Jets in High Mass Diffraction*, Phys. Lett. B211, 239 (1988).

[12] A.Donnachie,P.V Landshoff, Phys. Lett. B296, 227, (1992)

[13] B. Kopeliovic et al., hep-ph/9601291

[14] G. Ingelman and P. E. Schlein, *Jet Structure in High Mass Diffractive Scattering*, Phys. Lett. B152, 256 (1985).

[15] M. Gallinaro, *Prospects of Diffractive Physics with the CDF Forward Detectors at the Tevatron*, hep-ph/0407255.

[16] T. Affolder et al. (CDF Collaboration), Phys. Rev. Lett 87, 241802 (2001).

[17] M. Convery, *Diffractive W and Z production at the Fermilab Tevatron*, arXiv:0606024v1[hep-ex].

[18] A.R.White, *Physics of a sextet quark sector*, Phys. Rev. D72, 036007 (2005).

[19] The CMS-ECAL group, P. Adzic et al., *Results of the first performance tests of the CMS electromagnetic calorimeter*, Eur. Phys. J. C44 (2006) S1.1

[20] The CMS Collaboration, CMS, *the Compact Muon Solenoid: Technical proposal*, CERN-LHCC-94-38.

[21] G. Acquistapace et al., CMS, *The Magnet Project: Technical Design Report*, CERN-LHCC-97-10.

[22] C. Eck et al., *LHC computing Grid: Technical Design Report. Version 1.06 (20 Jun 2005)*. Technical Design Report LCG. CERN, Geneva, 2005.

[23] A.A. Annenkov, M.V. Korzhik and P. Lecoq, *Lead tungstate scintillation material*, Nucl. Instrum. Meth. A 490 (2002) 30

[24] K. Deiters et al., *Double screening tests of the CMS ECAL avalanche photodiodes*, Nucl.Instrum. Meth. A 543 (2005) 549.

[25] S. Baccaro et al., *Radiation damage effect on avalanche photo diodes*, Nucl. Instrum. Meth.A 426 (1999) 206.

[26] A. Bartoloni, *The power supply system for CMS-ECAL APDs*, in Proceedings of the 7th Workshop on Electronics for LHC Experiments, Stockholm Sweden (2001), http://cdsweb.cern.ch/record/530694; A. Bartoloni et al., *High voltage system for the CMS electromagnetic calorimeter*, Nucl. Instrum. Meth. A 582 (2007) 462.

[27] K.W. Bell et al., *Vacuum phototriodes for the CMS electromagnetic calorimeter endcap*, IEEE Trans. Nucl. Sci. 51 (2004) 2284.

[28] Yu. I. Gusev et al., *Super radiation hard vacuum phototriodes for the CMS endcap ECAL*,Nucl. Instrum. Meth. A 535 (2004) 511.

[29] B. Betev et al., *Low voltage supply system for the very front end readout electronics of the CMS electromagnetic calorimeter*, in 9th Workshop on Electronics for LHC Experiments, CERN-LHCC-2003-055 page 353.

[30] M. Raymond et al.,*The MGPA electromagnetic calorimeter readout chip for CMS*, in 9th Workshop on Electronics for LHC Experiments, Amsterdam The Netherlands (2003), CERN-LHCC-2003-055 page 83.

[31] G. Minderico et al.,*A CMOS low power, quad channel, 12 bit, 40 MS/s pipelined ADC fo applications in particle physics calorimetry*, in 9th Workshop on Electronics for LHC Experiments, Amsterdam The Netherlands (2003), CERN-LHCC-2003-055 page 88.

[32] The CMS Collaboration,*Technical Design Report, Volume 2: Data Acquisition and High-Level Trigger*, CERN LHCC 2002-36, 2002

[33] The CMS Collaboration, *The CMS experiment at the CERN LHC*, JINST3S08004, 2008.

[34] The CMS Collaboration,*CMS Physics Technical Design Report,Volume I:Detector performance and software*, CERN-LHCC-2006-001, 2006.

[35] The CMS Collaboration, *The Electromagnetic Calorimeter Technical Design Report*,CERN/LHCC97-033, 1997.

[36] R.Arcidiacono, A.Brett, F.Cavallari, A.David, N. S. Eggert, G.Franzoni, M.Marone, P.Musella, G.Organtini, P.Rumerio, A.Thea, E.Vlassov, *ECAL front-end monitoring in the CMS experiment*, Conference Report presented at "CHEP09: International Conference On Computing In High Energy Physics And Nuclear Physics".

[37] http://tomcat.apache.org

[38] http://root.cern.ch

[39] The CMS Collaboration, *The TriDAS Project Technical Design Report, Vol. 1.*, CERN/LHCC 2000-038, 2000.

[40] The CMS Collaboration, *The TriDAS Project Technical Design Report, Vol. 2.*, CERN/LHCC 2002-026, 2002.

[41] R. Alemany et al., *CMS ECAL off-detector electronics*, in Proceedings of the 11th International Conference on Calorimetry in High Energy Physics (CALOR2004), Perugia Italy (2004), CMS-CR-2004-022, http://cdsweb.cern.ch/record/787474.

[42] R. Alemany et al., *Overview of the ECAL off-detector electronics of the CMS experiment*, IEEE Nucl. Sci. Symp. Conf. Rec. 2 (2004) 1053.

[43] P. Paganini et al., *Tests of the boards generating the CMS ECAL trigger primitives: from the on-detector electronics to the off-detector electronics system*, in Proceedings of the 10th Workshop on Electronics for LHC Experiments, Boston U.S.A. (2004), CMS-CR-2004-066, http://cdsweb.cern.ch/record/814461.

[44] N. Almeida et al., *Calorimeter trigger synchronization in CMS, implementation and test system*, in Proceedings of the 10th Workshop on Electronics for LHC Experiments, Boston U.S.A. (2004), CMS-CR-2004-068, http://cdsweb.cern.ch/record/823745.

[45] N. Almeida et al., *Data concentrator card and test system for the CMS ECAL readout*, in Proceedings of the 9th Workshop on Electronics for the LHC Experiments, Amsterdam The Netherlands (2003), CMS-CR-2003-056, http://cdsweb.cern.ch/record/692739.

[46] R. Alemany et al., *Test results of the data concentrator card of the CMS electromagnetic calorimeter readout system*, in Proceedings of the 10th Workshop on Electronics for LHC Experiments, Boston U.S.A. (2004), http://cdsweb.cern.ch/record/814237.

[47] N. Almeida et al., *The selective read-out processor for the CMS electromagnetic calorimeter*, IEEE Nucl. Sci. Symp. Conf. Rec. 3 (2004) 1721.

[48] J. Gutleber and L. Orsini, *Software architecture for processing clusters based on I2O*, Cluster Comput. 5 (2002) 55.

[49] O. Nierstrasz, S. Gibbs and D. Tsichritzis, *Component-oriented software development*, Comm. ACM 35 (1992) 160.

[50] J. Boyer, *Canonical XML version 1:0*, W3C Recommendation, 16 August 2006, http://www.w3c.org/XML.

[51] D. Box et al., *Simple Object Access Protocol (SOAP) 1:1*, W3C Note 08,http://www.w3.org/TR/SOAP.

[52] http://xdaq.web.cern.ch

[53] http://linux.web.cern.ch/linux/

[54] G. Bauer et al., *The Run Control and Monitoring System of the CMS Experiment*, (2007) CERN CMS CR-2007/062.

[55] P. Adzic et al., *Implementation and performance of the Detector Control System for the electromagnetic calorimeter of the CMS experiment*, (2007), presented at Topical workshop on electronics for particle physics, 3-7 September 2007, Prague, Czech Republic

[56] http://itcobe.web.cern.ch/itcobe/Services/Pvss/

[57] CMS Collaboration, *Ecal technical design report*, CERN-LHCC-97-33

[58] Steinhart, J. S. and S. R. Hart, *Calibration curves for thermistors*, Deep Sea Res., 15, 497-503 (1968).

[59] S. Chatrchyan *et al.* [CMS Collaboration],*Performance and Operation of the CMS Electromagnetic Calorimeter*,JINST **5** (2010) T03010

[60] CMS Collaboration, *The Electromagnetic Calorimeter Project: Technical Design Report*,CERN/LHCC **97-033** (1997). CMS TDR 4

[61] CMS Collaboration, *The CMS experiment at the CERN LHC*, JINST **3** (2008) S08004

[62] G. Magazzu, A. Marchioro and P. Moreira , *DCUF User Guide*, CERN - EP/MIC, Geneva Switzerland, November 14, 2003

[63] N. Eggert, G. Franzoni, R. Rusack, F. Cavallari, P. Rumerio, *Calibration of the ECAL Thermal Sensors Using Cosmics Stand Data*, CERN CMS IN-2008/043

[64] R.Arcidiacono, M.Marone, *Ecal thermal stability during Cosmic Rays Run 2008*, CERN Detector Note number DN2010/003 , 2010.

[65] S. Agostinelli at al., Nucl. Instr. and Methods A, 506 (2003) 250-303

[66] CMS Collaboration, *Measuring Electron Efficiencies at CMS with Early Data*, CMS 504 Note EGM-07-001 (2007).

[67] S.Abdullin et al., *Sensitivity of the Muon Isolation Cut Efficiency to the Underlying Event Uncertainties*, CMS-NOTE 2006-033, (2006).

[68] P.Bruni,A.Edin,G.Ingelman, *POMPYT 1 version 2.6 A Monte Carlo to Simulate Diffractive Hard Scattering Processes*, ISSN 0418-9833, May 1995

[69] http://www3.tsl.uu.se/thep/pompyt/

[70] The CMS collaboration, *Measurements of Inclusive W and Z Cross Sections in pp Collisions at $\sqrt{s}=7$ TeV*, CMS PAS EWK-10-002, 2010.

[71] The CMS collaboration, *Measurements of Inclusive W and Z Cross Sections in pp Collisions at $\sqrt{s}=7$ TeV*, JHEP01 080, 2011.

[72] The CMS Collaboration, *particle-Flow Event Reconstruction in CMS and Performances for Jets, E_t^{miss}, and Taus*, CMS PAS PFT-09-001, 2009.